

Abstract

Vancouver has a large seismic risk due to the proximity of the city to the Cascadia subduction zone offshore, the Cascadia Subduction Zone, the soft soils the metropolitan region overlies, and the mountainous topography nearby. The soft soils and mountainous topography could cause an increase in shaking due to the sedimentary basin and topographic effects respectively. Numerical three-dimensional (3D) wave propagation simulations (WPS) were run using a finite difference scheme developed by Peterson and Sjogreen (2012), Seismic Waves, 4th order, to perform simulations of large shallow crustal rupture scenario earthquakes using the 1994 M6.7 Northridge, California earthquake slip distribution. The 3D WPS quantify the effects that topography and higher frequency waves can have on ground motions by running simulations with and without topography, with maximum resolvable frequencies increased from 0.5 Hz to 2 Hz in the simulation with topography. The Peak Ground Velocity (PGV), relative difference between simulations with and without topography and velocity amplitude maps were computed. Results showed significant variance in amplification due to rupture characteristics and location, and PGV increased with topography when higher frequencies up to 2 Hz were included in simulations for most sources, particularly at mountainous sites. The effect of harder ground conditions at these sites was not counterbalanced by topographic effects for lower frequency (< 0.5 Hz) simulations. The mountainous sites showed de-amplification at lower frequencies and more amplification at higher frequencies, while low elevation sites showed more amplification at low frequencies and less at higher frequencies.

Keywords

Seismology, Finite Difference, Numerical Simulations, PGV, velocity ground motions, topography, Georgia Basin, British Columbia, Vancouver, wave propagation simulation

Summary for Lay Audience

Vancouver is surrounded by mountainous terrain and is underlain by soft soils, both of which could increase shaking during large earthquakes and cause additional damage to what is currently modelled and expected. The effect of these soft soils has been studied, but the effect of topography in this region has not been. The Topographic effect is caused by topographic variation and the basin effect is caused by the structure of sedimentary basins and their soft soils. This study conducts numerical simulations that can model the ground motions from these large earthquakes and includes topography in the model for the Greater Vancouver Region for the first time and quantifies the increase in shaking that was experienced for multiple different earthquake rupture scenarios at different location throughout Vancouver. It was found that increased shaking from including topography in the models was dependent on the source that generates the earthquake and the earthquake location. It was also found that for most scenarios, mountainous regions experience more increase in shaking than areas that are at lower elevations when higher frequencies were incorporated into the simulation, while there was less shaking at lower frequencies.

Co-authorship Statement

The work in this study is conducted by Alex Vanderhoeff, under the supervision of Drs. Sheri Molnar and Hadi Ghofrani. Seismic Waves, 4th order, an open-source program for simulating seismic wave propagation on parallel computers, is executed using the Compute Canada partner organization, SHARCNET's compute resources, specifically the Graham high-performance computing cluster. The base elastic physical model representative of the local geology beneath the Greater Vancouver area was provided by Dr. Sheri Molnar. The topographic data was provided by the United States Geologic Survey's GMTED2010 dataset. The Standard Rupture File used to simulate specific earthquake source scenarios were generated using the Song Rupture Model Generator (SongRMG; Song, 2016). I developed MATLAB and Python scripts to process seismic data output from the simulations. This included filtering the data, plotting, and outputting figures. Scripts to properly format the topography and velocity model files were generated in collaboration between Dr. Hadi Ghofrani and myself.

Acknowledgements

I would like to thank all members of the Good Vibrations and Excitations group for their help and support throughout my time at Western University, and to the entire Western earth science community for helping make my time at Western a wonderful experience. It was a privilege to get to meet you all and work with you for the past 7 years and I hope to cross paths with you all again soon.

I especially would like to thank Hadi Ghofrani and Sheri Molnar for their help and guidance throughout this process. Hadi was integral in understanding how SW4 worked guiding me through new and relevant literature in the field. If not for Hadi, I may still be debugging SW4. Sheri provided valuable feedback and direction throughout this process, along with perspective on the industry and career advice to help me achieve my goals, along with some enjoyable chats and a fun field school! I enjoyed getting to work with you both and hope we keep in touch.

I would like to thank my mother, father, brother and girlfriend for their love and support throughout this degree. It was challenging starting my master's during Covid-19 and delaying some of my other life goals, and I thank you for always being there and helping me work through all problems I encountered.

Table of Contents

Abstract	i
Keywords	ii
Summary for Lay Audience.....	iii
Co-authorship Statement	iv
Acknowledgements	v
Table of Figures	viii
Table of Tables	xii
List of Abbreviations and Symbols	xiii
Chapter 1 – Introduction.....	1
1.1: Seismicity in Southern British Columbia	1
1.2: Seismic Hazard and Risk	4
1.3: Topographic Resonance	6
1.4: Basin Effects	12
1.5: Thesis Aims.....	15
1.6: Thesis Organization	16
Chapter 2 – Ground Motion Simulation Methods.....	18
2.1: Finite Difference Scheme	18
2.2: Features of SW4: Topography and Mesh Refinement.....	22
2.3: 3D Physical Structure Model.....	25
2.4: Earthquake Source Model.....	26
2.5: Presentation of 3D synthetic ground motions	29
Chapter 3 - 3D Synthetic Ground Motions and Associated Topographic Effects up to 0.5 Hz	31
3.1 Seismic Stations.....	31
3.2 Velocity Ground Motion Recordings – 0.5 Hz Resolved Frequency	33
3.3 PGV Geomean and Relative Difference in PGV – 0.5 Hz Resolved Frequency.....	42
3.4 Modified Mercalli Intensity Ratings – 0.5 Hz Resolved Frequency	48
Chapter 4 - 3D Synthetic Ground Motions and Associated Topographic Effects up to 2 Hz	49
4.1 Velocity Ground Motion Recordings – 2 Hz Resolved Frequency	50
4.2 Velocity Amplitude Maps of the Greater Vancouver Area.....	54
4.3 PGV Geomean Relative Difference – 2 Hz Resolved Frequency	60

4.4 Modified Mercalli Intensity Ratings – 2 Hz Resolved Frequency	63
4.5 Frequency Spectrum and HVSR.....	64
4.6 Traverse Up Mt. Cypress	68
Chapter 5 - Discussion and Conclusions	70
5.1 Thesis Contributions	73
5.2 Future Work	73
References.....	74
Appendix	80
Curriculum Vitae.....	112

Table of Figures

Figure 1: The tectonic setting off the coast of Vancouver Island has strike-slip, convergent, and divergent boundaries. This map shows plate motions of the Juan de Fuca, Gorda, and Explorer oceanic plates and the direction of these motions. Retrieved from Molnar et al., (2014b).....	1
Figure 2: (a) Seismic waves propagating through the subsurface increase in amplitude when transitioning from hard to soft soils. (b) Seismic waves focusing and de-focusing dependent on the interface boundary in the subsurface. Retrieved from Hayek (2016).....	6
Figure 3: (a) Steep slope focussing seismic waves towards the peak, increasing ground motions at the peak of the slope. (b) A gentle slope focussing seismic waves away from the peak, decreasing the ground motions at the peak. (c) One side of the slope receiving higher amplification than the other due to the incident angle of the seismic waves. Retrieved from Shafique et al., (2010).....	7
Figure 4: (a) Focussing of seismic waves due to the slopes of the mountain causes an increase in ground motions at the peak of the slope. (b) De-focussing of seismic waves away from valleys and towards mountainous regions causes de-amplification of seismic waves in the valleys. Retrieved from Shafique et al., (2010).....	10
Figure 5: Topography of the GVA simulation domain, showing very low elevations on the Georgia basins and higher elevations in the mountainous regions surrounding the GVA.....	23
Figure 6: A velocity model with two MR layers and a topography layer. Retreived from Petersson and Sjogren, (2012).....	24
Figure 7: Modified Mercalli Intensity units and corresponding perceived shaking, peak motion type attributes, and damage potential. PGV values represent the minimum value for corresponding instrumental intensity. Retrieved from Worden and Wald (2016).....	30
Figure 8: Map of recording stations in the shallow crustal scenarios. The blue markers indicate sites where velocity ground motions were recorded. The yellow markers are other interesting sites that are out of the scope of the study but have important infrastructure nearby.....	33
Figure 9: The propagation of the ground motions away from the Georgia Strait rupture from time t = 5 seconds until t = 70 seconds.....	35

Figure 10: Velocity ground motions at several seismic stations with and without topography at resolvable frequencies up to 0.5 Hz for the Mt. Cypress (a), Delta (b), Mt. Seymour (c), and the Richmond (d) seismic recording sites.....	39
Figure 11: Shot gather plot ground motions for the Deming 1 (a), Mt. Vernon (b), Deming 2 (c), and the Georgia Strait (d) scenarios.....	40
Figure 12: Shot gather plot ground motions for the San Juan Island (a), Skip Jack (b) Victoria (c), and Salt Spring Island (d) scenarios.....	42
Figure 13: (a) Georgia Strait velocity time series with MR at Delta station. (b) Georgia Strait simulation with MR at Cypress Mountain station. (c) Georgia Strait simulation with MR at Richmond station. (d) Georgia Strait simulation with MR at Mt. Seymour station.....	52
Figure 14: (a) Georgia scenario velocity ground motions recorded at the Delta, Richmond, Airport, UBC, Pt. 1 (West Vancouver), pt. 2, pt. 3, pt. 4 and pt. 5 (Mt. Cypress peak) stations in the E-W direction with and without topography. Simulations without MR have much lower amplitude ground motions than those with MR. (b) The Deming 1 scenario. (c) The Deming 2 scenario. (d) The Mt. Vernon scenario.....	54
Figure 15: (a) Victoria rupture velocity amplitude map with no topography at 34 seconds. (b) Victoria rupture velocity amplitude map with topography at 34 seconds.....	57
Figure 16: (a) Georgia Strait rupture velocity amplitude map without topography at 34 seconds. (b) Georgia Strait rupture velocity amplitude map with topography at 34 seconds.....	57
Figure 17: (a) Mt. Vernon rupture velocity amplitude map without topography at 34 seconds. (b) Mt. Vernon rupture velocity amplitude map with topography at 34 seconds.....	58
Figure 18: (a) Deming 1 rupture velocity amplitude map without topography at 34 seconds. (b) Deming 1 rupture velocity amplitude map with topography at 34 seconds.....	58
Figure 19: (a) Deming 2 rupture velocity amplitude map without topography at 34 seconds. (b) Deming 2 rupture velocity amplitude map with topography at 34 seconds.....	59
Figure 20: (a) Salt Spring Island rupture velocity amplitude map without topography at 34 seconds. (b) Salt Spring Island rupture velocity amplitude map with topography at 34 seconds.....	59

Figure 21: (a) San Juan Island rupture velocity amplitude map without topography at 34 seconds. (b) San Juan Island rupture velocity amplitude map with topography at 34 seconds.....	60
Figure 22: (a) Skip Jack rupture velocity amplitude map without topography at 34 seconds. (b) Skip Jack rupture velocity amplitude map with topography at 34 seconds.....	60
Figure 23: Fourier frequency spectrum for the Georgia scenario at the (a) Delta, (b) Mt. Cypress, (c) Airport, (d) Downtown, (e) Mt. Seymour, and (f) Richmond stations with topography and MR. The E-W, N-S and vertical directions are shown.....	66
Figure 24: (a) HVSR for Delta, with and without topography for the Georgia Strait scenario. Increases in amplification are apparent with topography at most frequencies, although there is more variability. (b) HVSR for Mt. Cypress, with and without topography for the Georgia Strait scenario. Frequencies from 1.5Hz to 3.5Hz show amplification with topography included, while frequencies below 1.5Hz do not show amplification.....	68
Figure 25: Velocity amplitude maps for the Georgia scenario with MR from 2-66 seconds of simulation duration.....	80
Figure 26: Velocity amplitude maps for the Georgia scenario without topography and MR from 2-66 seconds of simulation duration.....	82
Figure 27: Velocity amplitude maps for the Mt. Vernon scenario with MR from 2-66 seconds of simulation duration.....	84
Figure 28: Velocity amplitude maps for the Mt. Vernon scenario without topography and MR from 2-66 seconds of simulation duration.....	86
Figure 29: Velocity amplitude maps for the Salt Spring Island scenario with MR from 2-66 seconds of simulation duration.....	88
Figure 30: Velocity amplitude maps for the Salt Spring Island scenario without topography and MR from 2-66 seconds of simulation duration.....	90
Figure 31: Velocity amplitude maps for the San Juan Island scenario with MR from 2-66 seconds of simulation duration.....	92
Figure 32: Velocity amplitude maps for the San Juan Island scenario without topography and MR from 2-66 seconds of simulation duration.....	94
Figure 33: Velocity amplitude maps for the Deming 1 scenario with MR from 2-66 seconds of simulation duration.....	96

Figure 34: Velocity amplitude maps for the Deming 1 scenario without topography and MR from 2-66 seconds of simulation duration.....	98
Figure 35: Velocity amplitude maps for the Deming 2 scenario with MR from 2-66 seconds of simulation duration.....	100
Figure 36: Velocity amplitude maps for the Deming 2 scenario without topography and MR from 2-66 seconds of simulation duration.....	102
Figure 37: Velocity amplitude maps for the Skip Jack Island scenario with MR from 2-66 seconds of simulation duration.....	104
Figure 38: Velocity amplitude maps for the Skip Jack Island scenario without topography and MR from 2-66 seconds of simulation duration.....	106
Figure 39: Velocity amplitude maps for the Victoria scenario with MR from 2-66 seconds of simulation duration.....	108
Figure 40: Velocity amplitude maps for the Victoria scenario without topography and MR from 2-66 seconds of simulation duration.....	110

Table of Tables

Table 1: The average recurrence and damage of various mechanism earthquakes in Southwestern British Columbia and Northwestern Washington.....	4
Table 2: Computational resources used for numerical simulations.....	25
Table 3: Rupture characteristics of simulations ran in the GVA.....	27
Table 4: PGV Geomean calculations of the 8 scenarios at 8 recording stations with topography included.....	46
Table 5: PGV geomean calculations for the 8 scenarios at 8 recording stations without topography included in the simulations.....	47
Table 6: Relative percent difference between simulations with and without topography. Negative values indicate a decrease in PGV when topography is included, and a positive number indicates an increase in PGV when topography is included.....	48
Table 7: MMI for the Georgia Scenario at select sites show strong shaking to very strong shaking at most sites, with correspondingly light to moderate damage. Mt. Seymour shows an increase in perceived shaking when topography is included.....	49
Table 8: PGV Geomean in the horizontal directions, including topography with MR. The scenarios shown are the same as was computed without MR to directly compare and quantify the effect of higher frequencies had.....	61
Table 9: Relative difference in the PGV geomean between topography including MR and topography without MR.....	63
Table 10: MMI for the Georgia Strait at select sites shows moderate to strong shaking at most sites, with correspondingly light to moderate damage.....	64
Table 11: PGV max of traverse up Mt. Cypress in E-W direction using Georgia Strait scenario. Simulations with topography show a greater increase in PGV with increasing elevation over the simulations without topography. The simulations with MR showed even greater increases in PGV due to increasing elevation.....	70

List of Abbreviations and Symbols

AWP - ODC	Anelastic Wave Propagation – Olsen, Day, Ciu
B.C	British Columbia
CSZ	Cascadia Subduction Zone
DEM	Digital Elevation Model
FD	Finite Difference
GVA	Greater Vancouver Area
HPC	High Performance Computing
HVSR	Horizontal to Vertical Spectral Ratio
JDF	Juan de Fuca
LiDAR	Light Detection and Ranging
MR	Mesh Refinement
MMI	Modified Mercalli Intensity Scale
NA	North American
PGA	Peak Ground Acceleration
PGV	Peak Ground Velocity
SRF	Standard Rupture File
SSR	Standard Signal Ratio
SW4	Seismic Waves, 4 th Order
TR	Topographic Ratio
USGS	United States Geological Survey
WPS	Wave Propagation Simulations
3D	Three-Dimensional

ρ	Density
$u(x, t)$	Displacement Vector
Ω	Computational Domain
t_0	Offset time
t	Time
n	Unit normal vector from the surface of the model
$F(x, t)$	Forcing function
T	Stress tensor
$g(t)$	Moment history time function
f	Frequency
f_0	Frequency of the time function
p	Nodes per wavelength
h	Grid spacing
f_{\max}	Maximum resolvable frequency
V_s	S-waves
V_p	P-waves
$\tau(x, y),$	Elevation in the topography model
ω	Angular Frequency
L_{\min}	Shortest wavelength

Chapter 1 – Introduction

1.1: Seismicity in Southern British Columbia

The Greater Vancouver Metropolitan Area (GVA) is located near the northern end of the Cascadia Subduction Zone (CSZ), where the Juan de Fuca (JDF) and Explorer oceanic plates are subducting in a northeast direction underneath the North American (NA) continental plate (Figure 1; NRCAN, 2017). The rate of subduction is 33-41 mm/yr (Gripp and Gordon, 2002). Once significant stress is accumulated, Earth's brittle crust will break or fail along planes of weakness (active faults), releasing energy in the form of heat and propagating seismic body waves.

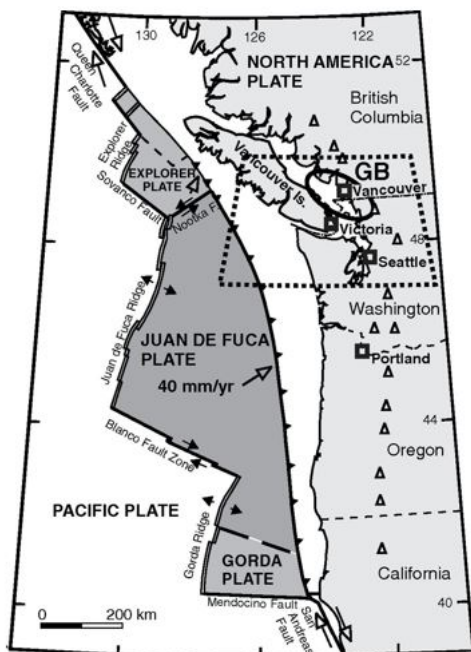


Figure 1: The tectonic setting off the coast of Vancouver Island has strike-slip, convergent, and divergent boundaries. This map shows plate motions of the Juan de Fuca, Gorda, and Explorer oceanic plates and the direction of these motions. Retrieved from Molnar et al., (2014b).

There have been several moderate (**M5-M6.4**) to large (**M6.5+**) magnitude earthquakes in British Columbia (B.C) and Washington State over the last several hundred years. These include 561 potentially damaging moderate earthquakes occurring from 1660-2009 (Ghofrani and Molnar, 2019), including the 1997 **M4.7** Georgia Strait earthquake, with an epicentre 30 km West of Vancouver, the 2001 **M6.8** Nisqually earthquake (Cassidy et al. 2003; Molnar 2003), the **M7.8** Haida Gwaii earthquake of October 27th, 2012, the stronger **M8.1** Queen Charlotte Island earthquake of 1949, and the **M9** megathrust earthquake offshore Vancouver Island of 1700 (Goldfinger et al., 2012). These earthquakes occurred before extensive seismic networks were deployed or in regions too far for strong shaking to reach the Greater Vancouver Area (GVA), limiting the availability of high-quality ground motion data in the GVA. Recordings on seismograms in the region could provide meaningful ground motion data and aid in the determination of shaking during such events. Notable datasets of regional earthquake recordings in Victoria and Vancouver include 4 datasets recorded by trigger-based strong motion instruments between 1976-2001 and ~8 datasets recorded by Internet Accelerographs between 2004-2015 (Cassidy et al. 2019; Assaf et al. 2022). Of these, only recordings of the 2001 **M6.8** Nisqually earthquake and the 2015 **M4.7** Victoria earthquake have been used for validation of 3D synthetic ground motions from wave propagation modelling (Molnar et al. 2014a; Ghofrani and Molnar, 2019). In these previous studies, synthetic ground motions are overestimated in the GVA by a factor of 1.6 (Molnar et al. 2014a; Ghofrani and Molnar 2019) when compared to empirical data. These historical earthquakes, along with others that have occurred near the CSZ are generated by three seismic sources:

1. The Cascadia thrust fault interface between the JDF and NA plates. This fault zone is currently locked and accumulating strain (Clague, 1997), and has a recurrence interval of about 230 years (Leonard et al., 2010) to 500 years (Clague, 1997). When this ~1000 km long fault slips, earthquakes such as the **M9** CSZ megathrust earthquake offshore Vancouver Island in 1700 occurs. A total of 14 partial-to-full rupture Cascadia interface earthquakes with $M > 7$ are known to have occurred from paleoseismic studies (Leonard et al., 2010; Goldfinger et al., 2012), the last occurred on Jan. 26th, 1700 (Atwater et al., 2005).
2. Within the NA plate that is overriding the JDF plate. Compressional stress is stored and results in shallow (< 30 km) NA plate earthquakes (termed ‘crustal’ earthquakes here). The assumed maximum magnitude of crustal earthquakes is **M7.3** (Adams and Halchuk, 2003) based on the largest known shallow earthquakes: 1872 **M7**, 1918 **M7**, 1946 **M7.3** (Molnar et al. 2014b). No dominant faulting has been observed, with 30% strike slip, thrust, or some combination of them (Balfour et al., 2011). Rupture characteristics for this type of earthquake are unknown for the GVA, since large, historical events occurred before seismic networks were deployed in the region.
3. Within the subducting JDF plate itself. These earthquakes occur at deep depths of 30-60 km (Cassidy, 2009). An example of this was the previously stated 2001 **M6.8** Nisqually, Washington earthquake. These events are also the most frequent; the occurrence rate of **M5** inslab earthquakes is approx. 1 per decade. The assumed maximum magnitude for a deep JDF earthquake is **M7.1** (Adams and Halchuk,

2003); the largest inslab events have been the 1949 **M**7.1, 2001 **M**6.8 and 1965 **M**6.5 earthquakes (Molnar et al. 2014a).

Table 1 shows the average recurrence and area of damage of various mechanism earthquakes in Southwestern B.C and Northwestern Washington.

Table 1: The average recurrence and damage of various mechanism earthquakes in Southwestern British Columbia and Northwestern Washington.

Type of earthquake	Moment magnitude of earthquake (M_w)	Average recurrence (Years)
Subduction	8-9+	500
Crustal/Intraplate	7-7.5	30-40
Crustal/Intraplate	6	20
Crustal/Intraplate	5	5

Large magnitude earthquakes of these three seismic sources all have the potential to cause significant damage to the GVA if the region is not prepared to withstand earthquakes of these magnitudes.

1.2: Seismic Hazard and Risk

Natural hazards that are due to earthquake related phenomena, such as ground shaking, liquefaction, or fault rupture, are classified as seismic hazards (Reiter, 1999). The shaking resulting from earthquakes is a most basic form of seismic hazard. Quantifying the hazard and potential damage from future earthquakes is an important problem for cities that are near active subduction zones such as Vancouver. Seismic risk includes both the seismic hazard in a region multiplied by the (infrastructural and social)

vulnerabilities in that region (Wang, 2011). For example, an area where shaking could occur will have a larger seismic risk where there is dense population or large potential for damage due to critical infrastructure, than the risk in an area where there is a sparser population and less infrastructure. As an example, Munich Re (1992) estimated that the potential loss due to a M6.5 crustal earthquake 10 km beneath Vancouver could cause \$14-\$32 billion dollars in damage to the GVA. This kind of large loss could be due to several factors, including buildings made from un-reinforced masonry structure that were built prior to modern building codes, vulnerable infrastructure such as pipelines and power generating structures, along with additional liquefaction or landslide hazard. Vancouver and the southern GVA has a high seismic hazard due to the specific geological and tectonic setting of the area. Vancouver sits near an active subduction zone which could generate large earthquakes, has tsunami risk due to offshore earthquakes, while also being near mountainous regions, which could amplify and de-amplify shaking due to the topographic effect of mountainous topography, and as a result of soft sediments located in basin regions, causing a basin effect. Natural hazards that are due to earthquake related phenomena, such as ground shaking, liquefaction, or fault rupture, are classified as seismic hazards (Reiter, 1999). The shaking resulting from earthquakes is a most basic form of seismic hazard. In simplest terms, earthquake ground shaking is a combination of source (e.g., magnitude, stress drop), path (e.g., distance, seismic kappa), and site effects. Earthquake site effects encompasses all effects that alter earthquake shaking due to local site conditions (Figure 2) including 1D site effects (upward propagation of seismic waves through the soil column leads to increasing or amplified motions due to reduced seismic impedance and resonance) and 2D and 3D site effects

(e.g., wave interactions resulting from surface topography convexities and sedimentary basin concavities).

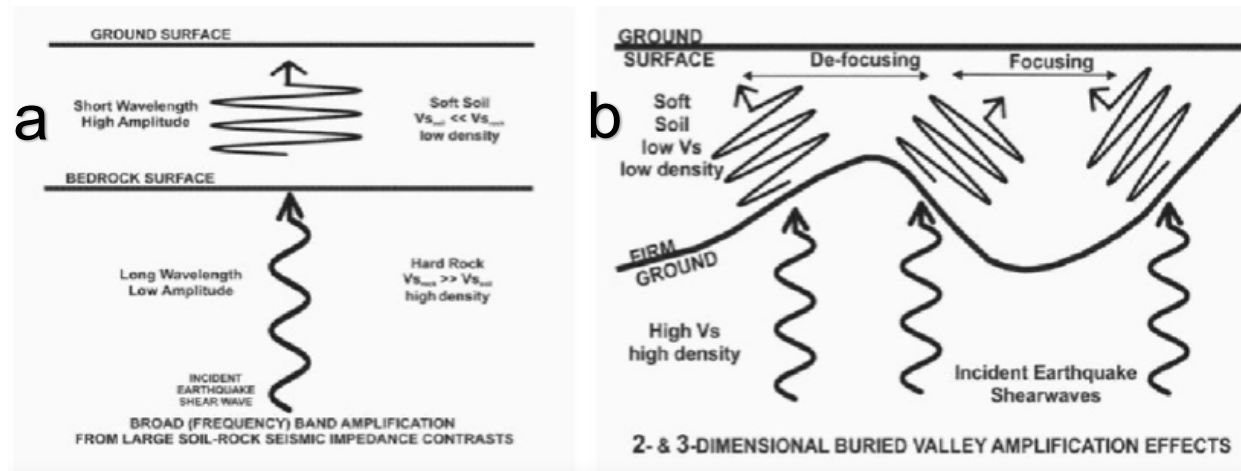


Figure 2: (a) Seismic waves propagating through the subsurface increase in amplitude when transitioning from hard to soft soils. (b) Seismic waves focusing and de-focusing dependent on the interface boundary in the subsurface. Retrieved from Hayek (2016).

1.3: Topographic Resonance

The topographical effect is caused by variations in the Earth's surface topography interacting with seismic waves that are propagating during an earthquake. The topographic effect is complex and has several main features. Topography has a larger amplification effect on the horizontal components (E-W, N-S) than the vertical components (Z) of seismic waves, causing greater amplification of S - waves and surface waves (Love, Rayleigh) than P - waves. This has the potential to cause additional damage to regions receiving this amplification, as S and surface waves are higher amplitude waves. The topographical effect also has significant impact on ground motions at topographic highs, such as hills, mountains, ridges, and cliffs, due to focusing of seismic waves causing an increase in the waves' amplitude through constructive interference.

Topographical lows such as valleys, the foot of hills, and basins can have the opposite effect, diffracting seismic waves, resulting in destructive interference and a decrease in ground shaking. This phenomenon is shown in figure 3, where focusing of seismic waves are shown in the subsurface of a mountain and de-focusing of seismic waves is shown in the buried valley.

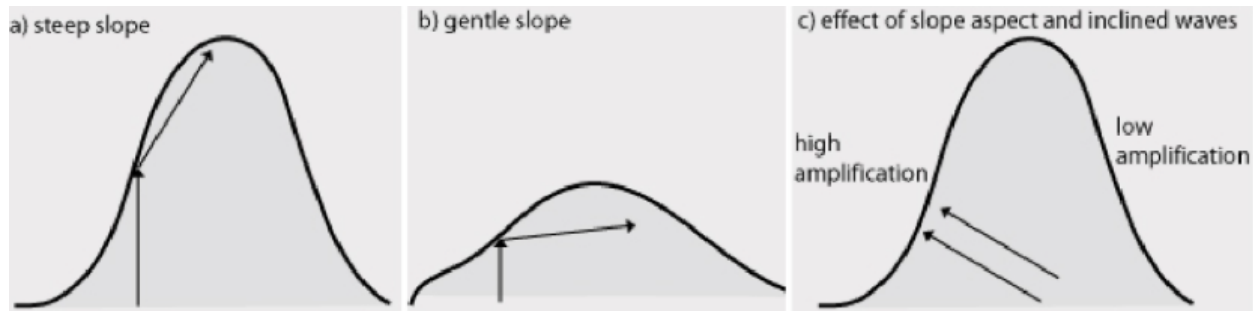


Figure 3: (a) Steep slope focussing seismic waves towards the peak, increasing ground motions at the peak of the slope. (b) A gentle slope focussing seismic waves away from the peak, decreasing the ground motions at the peak. (c) One side of the slope receiving higher amplification than the other due to the incident angle of the seismic waves. Retrieved from Shafique et al., (2010).

Boore (1972) used finite difference from SH ground motions as well as calculations using data generated from field observations to determine that when the incident wavelengths of seismic waves are comparable to the size of the topographic feature (the seismic wavelength is comparable to the basal width of the structural feature) and when the topographic feature is steep, topography can have significant effects on seismic waves, with models considered in Boore (1972) having amplification of up to 75% compared to models without topography. Boore also determined that the magnitude of these amplifications is dependent on the frequency and the azimuth of the incident wave, and if the topographic feature has an axis of elongation where it is longest, amplification is greatest for waves that are polarized orthogonal to this axis. This phenomenon is called topographic resonance, and it reduces rapidly as the wavelength increases relative to the

basal width (Stone et al., 2022). The height of the topographic feature also influences the response, with amplification increasing with ratio of height over basal width (Sanchez-Sesma, 1990). It was also determined that over a certain structural ratio (top: base, length: width) topographic resonance is at a maximum, with Martell et al., (1977) showing that Rayleigh waves interacting with cliff-like features experience increasing deflection and therefore increasing amplification when the cliff height/wavelength ratio over is greater than 0.3.

There are many difficulties that arise when trying to determine the effect of topography on ground motions during an earthquake. The topographic effect is heavily dependent on the azimuth and frequency of the incident seismic waves relative to the feature, which are determined by the earthquake's location and rupture characteristics. This makes it very difficult to decouple the contribution of topography from amplification of ground motions from other causes when analyzing seismic data. The attractiveness of numerical modelling permits comparing simulated or synthetic ground motions when topography is included and not included. However, topography can also be very difficult to include in simulations, since topographic features can be tens to hundreds of metres in width, or very narrow ridges where accurate topographic data is difficult to include in the model because it is often too coarse (needs to include the seismic source or depth of input motions), and if the data is very fine, may be too computationally expensive to include in the simulations. Some of these topographic features may also only show resonance at higher frequencies (>1 Hz), increasing the importance of incorporating higher frequencies in numerical simulations. These higher frequencies can be computationally difficult and expensive, particularly over larger areas, since it increases

the size of the velocity model files used to construct the grid. Variability in the 1 Hz frequency range due to shallow velocity structures and source distributions is high, complicating the prediction of the topographic effect as well (Stone et al., 2022).

Numerical, experimental, and analytical methods have all been employed to determine the seismic site effects of topography, as well as the topographic response in an area due to a certain seismic event of a specific frequency and rupture mechanism. Geli et al., (1988) determined that topography may more than double the strength of ground motions at a crest of a mountain relative to the foot, with some observations noting amplification factors greater than 30 (3000% increase in ground motions) at certain frequencies. Bouchon (1996) used a semi - analytical, semi - numerical method to calculate diffraction of elastic waves by an irregular topography of an arbitrarily shaped hill. Bouchon determined that the amplification near the top of the hill was a factor of 2 at 10 Hz. Celebi (1987) conducted site response experiments 5 months after the M7.8 1986 Chile earthquake to explore the role of topography and geology in amplification and found significant amplification at the ridges of Canal Beagle and was the first such set of data depicting topography amplification at heavily populated regions. Lovati et al., (2011) used experimental results and numerical simulations to show amplification factors on Narni ridge in Italy to be up to 4.5 in the direction orthogonal to the main elongation of the ridge. Lee et al., (2008) used a spectral element mesh method to determine the topographic effect of earthquakes near the Taipei basin on the nearby Central Mountain Range and on the nearby valleys. Lee found that for shallow earthquakes, the Central Mountain Range had increased amplification of shaking at mountain tops and ridges due to the focusing of seismic waves towards the peaks of these topographic highs, while valleys

have reduced ground motions because of de-focusing of seismic waves due to interaction with nearby topographic highs. This phenomenon is shown in figure 4. For deeper hypocenter earthquakes, the topography scattered body waves propagated as surface waves into the basin and created complex amplification patterns in the Taipei basin with a PGV increase of 250%.

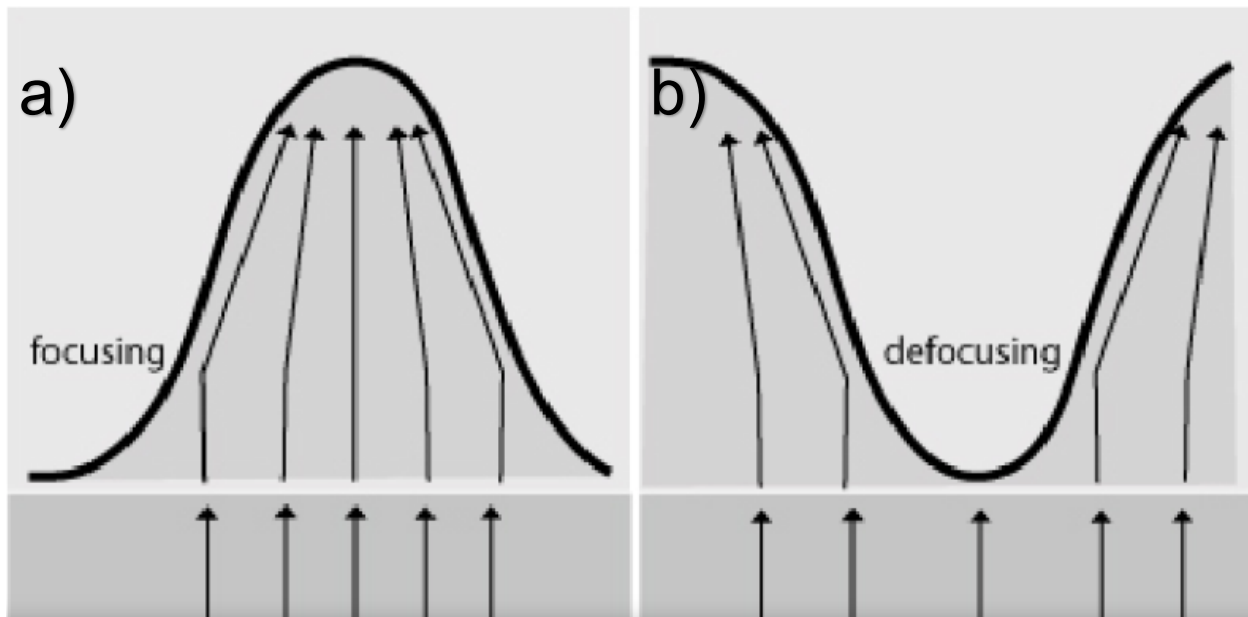


Figure 4: (a) focussing of seismic waves due to the slopes of the mountain causes an increase in ground motions at the peak of the slope. (b) de-focussing of seismic waves away from valleys and towards mountainous regions causes de-amplification of seismic waves in the valleys. Retrieved from Shafique et al., (2010).

Lee et al., (2009) then used a high-resolution light detection and ranging (LiDAR) digital elevation model (DEM) of 2 m resolution in similar simulations, showing that increasing topographic resolution increased the complexity of the ground motions in the model and showed more detail in the amplification maps produced. Ma et al., (2007) showed mountains scatter surface waves away, shielding the areas beyond the mountain range. Restrepo (2016) conducted 3D ground motion simulations for Medellin, Colombia, with 4 M5 ruptures used to determine a topographic effect amplification of 100-500% caused by

the high elevation (> 100 m) peaks nearby. Hartzell et al., (2014) used seismic data recorded over a year in 8 locations on Poverty Ridge, California to create Horizontal to Vertical Spectral Ratios (HVSР) and Standard Spectral Ratios (SSR) to determine site response from ground motions and ambient noise. They found that higher frequency amplification peaks are found to be transverse to the major axis of the topographic features of the ridge. This is in contrast with Massa et al., (2010), who computed HVSР for small, local earthquakes in Northern Italy. They found the amplification factor increased when the direction of ground motion was transverse to the elongation of the ridge, or the longest part of the topographic feature. Hough et al., (2010) used ground motion recordings at a ridge station compared to an adjacent valley station near the Petionville district of Port-au-Prince to estimate amplification due to topography during the 2010 M7 Haiti earthquake. They found that ground motions on the ridge were amplified relative to sites in the valley and relative to a hard rock site nearby, indicating topographic resonance played a significant factor in damage caused to Petionville. Khan (2019) studied the impact of topography on seismic amplification during the 2005 Kashmir earthquake using a spectral finite element method. It was shown that there was significant amplification on the ridges relative to the valleys, with 98% of highly damaged areas located in topographically amplified seismic response zones, and that slopes facing away from the source received large amplification of the seismic response.

As computational power increased, the ability to simulate ground motions at higher frequencies has become possible, resulting in some large simulations recently that have computed the topographic effect for large areas at high frequencies. Pitarka (2022) used SW4 and broadband simulations to simulate ground motions at < 5 Hz including surface

topography for the 2016 M6.5 Norcia, Italy earthquake. They were able to include a low velocity region in the upper depths of the model, allowing higher frequencies to be simulated. This is because the stability criteria for simulations of ground motions indicates that as the minimum shear wave velocity in a model decrease, the maximum resolvable frequency of the simulation increases. Local topography amplified Peak Ground Velocity (PGV) by 30%, with the highest PGVs on hilltops. Stone et al., (2022) used a 3D spectral element code with surface topography and a near surface low velocity layer with mesh spacing of 30 m to simulate M6.5-7 ruptures scenarios on the Seattle fault and thereby generate synthetic motions up to 3 Hz. A total of 20 earthquakes were simulated with different location and slip distributions on a planar fault surface. The average ground motions with and without topography were then calculated at select seismic recording stations. They found shaking amplification due to topography to be at topographic highs, with 25% of sites experiencing short period (≤ 2 s) ground motion amplification greater than 25-35% compared to without topography. Topographic amplification showed sensitivity to frequency, and no relationships between source location or site azimuths with strength of topographic amplification was determined.

1.4: Basin Effects

Vancouver is located on the Georgia basin, which is in the Georgia Strait off the west coast of B.C, and is a low-lying area infilled with soft sediments separating Vancouver Island from the mainland which could amplify shaking due to the basin effect. Sedimentary basins such as the Georgia basin can convert shear waves at the basin edges and walls (Bard & Bouchon, 1980), trap and focus the shear waves at basin edges (Graves et al., 1998), and cause constructive interference of upward propagating shear

waves and laterally propagating surface waves from basin edges. These basin effects can also cause amplification of seismic waves in the GVA. Basins also contain soft sediments that amplify shaking as seismic waves pass through them. The sequence infilling the Georgia basin is Holocene silts and sands as well as Pleistocene glacial deposits overlying irregular tertiary clastic sedimentary rock surface (Molnar et al., 2014a). The Georgia basin is wide and shallow, with dimensions of 130 km x 70 km x 5 km (Frankel et al., 2007) and because of the basin shape and the sedimentary soil sequence, causes significant amplification of seismic waves. An example of amplification due to basin effects is the 1985 M8.1 Michoacán earthquake. Mexico City sits on a sedimentary basin 300 km away from the epicenter of the earthquake, but had 14 times higher shaking (Singh et al., 1988) and lasted three times as long as the motion on firmer soil nearby (Rouillé and Chávez-García, 2006). Amplification has been shown to be dependent on the earthquake source, as demonstrated by Wirth et al., (2019), who used 3D simulations of point sources around the Seattle basin to examine the dependence of basin amplification on source azimuth, depth, and rupture type in the area. They found shaking was dependent on the location and type of rupture, with the far side of the basin experiencing the greatest amplification for close-in earthquakes, while crustal earthquakes had more amplification than deeper, intraplate earthquakes. Frankel et al., (2009) determined the sedimentary basin effects in Seattle by modelling 5 earthquakes using Anelastic Wave Propagation – Olsen, Day, Ciu (AWP – ODC) and determined that amplification is dependent on the direction to the earthquake. Amplification of seismic waves due to basin effects is also dependent on the frequency of the incoming seismic waves, demonstrated by Frankel (2018), who produced a set of broadband (0-10 Hz)

synthetic seismograms for **M9** earthquakes along the CSZ by combining synthetic seismograms from 3D FD code of Liu and Archuleta (2002). The **M9** Tohoku, Japan and **M8.8** Maule, Chile earthquake rupture models were used, and large amplification at 1-10 second periods were found for sites in sedimentary basins. Simulating earthquakes at higher frequencies can be computationally challenging, with Molnar (2014a; 2014b) able to simulate ground motions of frequencies resolved up to 0.5 Hz. Molnar (2014a; 2014b) computed ground motions for the GVA and to quantify the basin effects. In Molnar (2014a), the ground motions of deep Juan de Fuca subduction earthquake scenarios were simulated. A **M6** earthquake was modelled in locations with known seismicity. The earthquake simulation used the source-rupture model of the 2001 **M6.8** Nisqually earthquake, which was well determined by previous simulations using this model, such as Pitarka et al., (2004) and Frankel et al., (2007). The ground motions were simulated accounting for the amplification of shaking due to the soft sediments in the Georgia basin, and without accounting for the soft sediments in the basin, to determine the effect of the Georgia basin on shaking. It was found that the Georgia basin increased the ground motions by an average amplification factor of 4.5 in the basin, with a max PGV of 4.6 cm/s in the basin. The max PGV in Vancouver was found to be 3.2 cm/s, with an amplification factor of 3.1. Molnar (2014b) then simulated the ground motions of a shallow blind thrust earthquake. The source-rupture model used for this simulation was the **M6.7** Northridge, California blind thrust earthquake. 8 simulations were conducted within 100 km of the greater Vancouver area. The average PGV at stiff soil sites was found to be 17.8 cm/s, with an increase in peak PGV of an amplification factor of 4.1 from the basin edge effect. More recently, Roten and Olsen (2019) were able to simulate ground motions in the GVA

and Puget sound region with frequencies resolved up to 1.25 Hz. Roten and Olsen (2020) used a discontinuous mesh version of AWP-ODC, to simulate ground motions from a **M9** megathrust subduction earthquake along the CSZ, looking specifically at the ground motions in Seattle and Vancouver metro regions. A PGV of 0.25-0.54 m/s along with a spectral acceleration of 1-1.3 m/s² was computed for downtown Vancouver, while downtown Seattle had PGVs of 0.57-1.0 m/s and a spectral acceleration of 1.7-3.6 m/s².

1.5: Thesis Aims

The basin edge effect has been quantified by numerous studies in the GVA and Puget Sound regions such as by Molnar (2014a; 2014b) and Roten and Olsen (2019) for different types of earthquake scenarios, while the effects of topography and topographic resonance has not been quantified in the GVA. The aim of this study is to advance 3D wave propagation computations applied to seismic hazard of southwest B.C and to quantify the effects of including surface topography and higher frequency seismic waves on the synthetic ground motions in the GVA. A 3D velocity model of the Georgia basin region will be updated to include surface topography to perform 3D wave propagation simulations using SW4. The eight shallow crustal scenarios of Molnar (2014b) with the same rupture characteristics will be simulated, and the difference in ground motions with and without topography included in the simulations is quantified. There will be two sets of eight simulations, with the maximum resolvable frequency of 0.5 Hz for one set of eight and another set having a maximum resolvable frequency of 2 Hz. The effects caused by topography, soil stiffness, and the basin edge effect will be more complex and realistic than previous modelling.

1.6: Thesis Organization

This thesis consists of the methodology and two main chapters that attempt to quantify the ground motions generated from shallow crustal earthquake scenarios throughout the GVA, and the effects of higher frequency waves and topography on these ground motions.

Chapter 2 presents the methods used to conduct the numerical simulations and the different features and decisions that were made. This includes a discussion on the finite difference scheme used, the topography and mesh refinement parameters chosen, the 3D physical structure model containing the geological data of the simulation domain, the 8 earthquake sources simulated and how the rupture files were generated, and the presentation of the results of the simulations.

Chapter 3 contains the results from running numerical simulations of the shallow crustal earthquake rupture with resolved frequencies up to 0.5 Hz with and without topography. Time series of the velocity ground motions were generated and plotted at sites of importance due to their location and topography. Shot gather styled plots were generated to trace different wave packets spatially as the ground motions propagate away from the source. The PGV geometric mean with and without topography and the relative percent difference between them was calculated to quantify the effect of topography at lower frequencies.

Chapter 4 contains the results from running the numerical simulations of the shallow crustal earthquake rupture with resolved frequencies up to 2 Hz with topography. Time series of the velocity ground motions were generated and plotted at sites of

importance due to their location and topography. Shot gather styled plots were generated to trace different wave packets spatially as the ground motions propagate away from the source. The PGV geometric mean with and without topography and the relative percent difference between them was calculated to quantify the effect of topography at higher frequencies. The frequency content of the ground motions with topography and mesh refinement was analyzed by taking the Fourier transform of the acceleration ground motion data.

Chapter 2 – Ground Motion Simulation Methods

Chapter 2.1 presents a discussion of the governing equations used to model earthquakes, analysis of the finite difference scheme used to solve the elastodynamic equations and simulate the ground motions.

Chapter 2.2 discusses the topography and mesh refinement features of SW4 and describes their use in this study to simulate ground motions with topography and to increase the maximum resolvable frequency.

Chapter 2.3 presents the 3D physical structure model that contains information about the density, shear and compressional wave velocity, location, and attenuation of the simulation domain. This model was extracted from Molnar (2011).

Chapter 2.4 presents the earthquake source model used to create the 8 rupture scenarios and described the generation of the sources using SongRMG.

Chapter 2.5 discusses the presentation of results from the simulations. Several measurements are chosen here, including the PGV, $\text{PGV}_{\text{geomean}}$ and the TR ratio.

2.1: Finite Difference Scheme

To conduct numerical simulations of ground motions for the GVA, the Finite Difference (FD) scheme SW4 will be employed. SW4 numerically solves the elastodynamic equations of motion, a variation of the wave equation, for anelastic solids. Anelastic solids are viscoelastic solids that fully regain their shape after an applied load is removed. The elastodynamic equations can be used to model seismic wave propagation in the subsurface after the waves are generated by earthquakes (Rodgers, 2020). These equations are a system of linear, hyperbolic partial differential equations

that need to be solved simultaneously and numerically due to their coupling (Peterson and Sjogreen, 2012), and are given in the elastic case as:

$$\rho u_{tt} = \nabla \cdot T + F(x, t), x \text{ in } \Omega, 0 \leq t \leq t_1, \quad (2.1)$$

$$u(x, 0) = 0, u_t(x, 0) = 0, x \text{ in } \Omega \quad (2.2)$$

where ρ is the density, $u(x, t)$ is the displacement vector, Ω is the computational domain, $T = T(u)$ is the stress tensor, $\nabla \cdot T$ is the divergence of the stress tensor, $0 \leq t \leq t_1$ is the time interval this occurs over, and $F(x, t)$ is the forcing function that drives the motion from rest. Equation 2.2 are the initial conditions. The forcing function can be specified in the input file for SW4 as a point source or by using a Standard Rupture File (SRF) to model finite-fault rupture scenarios. Absorbing boundary conditions are used to limit unrealistic reflection and refraction of seismic waves along the Ω boundaries. These absorbing boundary conditions use super-grid damping layers surrounding all sides of the computational domain to ensure that waves are not reflected at the interfaces back into the domain. Ω is a box shaped region that follows the surface topography that can be specified by the user of SW4. The free surface boundary condition at the top boundary is given by:

$$T \cdot n = 0, z = \tau(x, y), t \geq 0 \quad (2.3)$$

where n is the unit normal at the surface of the model, and the vertical extent, z , is defined by the topography (τ), which can be specified from digital elevation mapping (x, y) or is zero if no topography is specified.

SW4 is fourth order accurate in space and time, which allows for finer grid spacing and lower error, as the error reduces at a faster rate as the grid size is decreased (Peterson and Sjogren, 2017). Peterson and Sjogren (2012) showed that fourth order FD schemes can also be more accurate when calculating surface waves in high compressional ratio mediums, where $V_p/V_s \gg 1$. SW4 uses cartesian or curvilinear grids that discretize the elastodynamic equations based on the summation by parts (SBP) principle, which gives the user a stable numerical answer (Rodgers, 2020). Curvilinear grids are generally used when topography is included in the simulations. The source time function is a measure of temporal variations in slip rate, integrated over an earthquake's rupture area (all sub-faults of the finite-fault model) (Hirano, 2022). This function determines many source characteristics of the simulated earthquakes and can be varied to alter the source characteristics of the scenario earthquake. SW4 allows the user to specify the time function and has several options; however, the integral of the Gaussian time function is used for the scenarios in this thesis is the Gaussian Integral:

$$g(t, t_0, \omega) = \frac{\omega}{\sqrt{2\pi}} \int_{-\infty}^t e^{\frac{-\omega^2(\tau-t_0)^2}{2}} d\tau \quad (2.4)$$

where for moment tensor sources, $g(t)$ is called the moment history time function, ω is the angular frequency, t is time, t_0 is the offset time based on the distance of the sub-fault from the hypocentre.

Use of the Gaussian Integral for source rupture modelling is chosen for two main reasons:

- 1) SW4 calculates displacements and uses a moment history time function, instead of the derivative of this function called the moment rate time function. If the moment rate time function were used, SW4 would calculate velocities instead of displacements. This provided more flexibility in the desired output.
- 2) The maximum frequency (f_{max}) of the moment history time function can be modelled with the following:

$$f_{max} = \begin{cases} 2.5f_0 & \text{for Gaussian functions} \\ 3.5f_0 & \text{for Smooth Bump function} \\ 4.5f_0 & \text{for Brune functions} \end{cases} \quad (2.5)$$

where f_0 is the frequency for the time function ($f_0 = \frac{f}{\pi}$ for the Gaussian time function). Higher f_{max} means that the physical model's grid or mesh spacing needs to be finer; the Gaussian Integral was chosen as it allows for coarser grid spacing.

There are other limitations placed on the numerical simulations due to limited computational resources and the stability criterion. To accommodate these limitations, a limit will be placed upon the number of nodes per wavelength. The shortest shear wavelength of the grid will be sampled at 5 nodes per wavelength, which minimizes grid dispersion effects and anisotropy (e.g., Levander, 1989, Moczo et al., 2000). This limits the maximum resolvable frequency, which we can estimate using:

$$P = \frac{L_{min}}{h} = \frac{V_{s,min}}{hf_{max}} \quad (2.6)$$

where P is the nodes per wavelength, L_{min} is the shortest wavelength, h is the grid spacing and f_{max} is the maximum frequency. For a P value of 5 and given a grid spacing of 250 m

and $V_{s,\min}$ of 625 m/s, the corresponding f_{\max} will be 0.5 Hz. We will increase f_{\max} to 2 Hz by reducing the grid spacing to 125 m at 4000 m depth and 62.5 m at 2000 m depth using a unique feature of SW4 called mesh refinement (MR).

2.2: Features of SW4: Topography and Mesh Refinement

SW4 allows for the inclusion of several unique features to be included in the simulations, including surface topography, attenuation of seismic waves, and MR. Surface topography allows for the specification of the physical model's surface shape. When surface topography is specified, SW4 generates a curvilinear grid between a user specified depth $z=z_{\max}$, and the surface layer of the model (z_0). z_{\max} works well when specified as:

$$z_{\max} \geq \tau_{\max} + 3(\tau_{\max} - \tau_{\min}) \quad (2.7)$$

A topographic model for southwestern B.C. is extracted from the GMTED2010 topography model of the United States Geological Survey (USGS). This model has a 15 arc-second resolution, which corresponds to a grid point approximately every 300 m at 50° latitude and covers the entire simulation domain (OpenDEM). The maximum elevation of the B.C. physical model area is 1729 m, so z_{\max} when surface topography is included for this study is:

$$z_{\max} \geq 1549 + 3(1549 - 0) \geq 6916 \text{ m} \quad (2.8)$$

hence, a z_{\max} of 7000 m is chosen for the shallow crustal scenarios in this study. This was determined by solving equation 2.8 with the maximum and minimum topography values, which were 1549 m and 0 m, respectively. The topography is smoothed by using 10

Jacobi smoothing iterations before the velocity model is transformed, which creates a topographic grid with smoother slopes and peaks that are less sharp even when the topographic grid used in the simulation is coarse, and to make sure variations in the topography can be resolved on the mesh grid. 10 Jacobi iterations is the program default and appears satisfactory after plotting the smoothed topography, shown in Figure 5. The southwestern B.C physical (velocity) model of Molnar (2011) is then transformed into a curvilinear grid between the z_{\max} value and the topography surface.

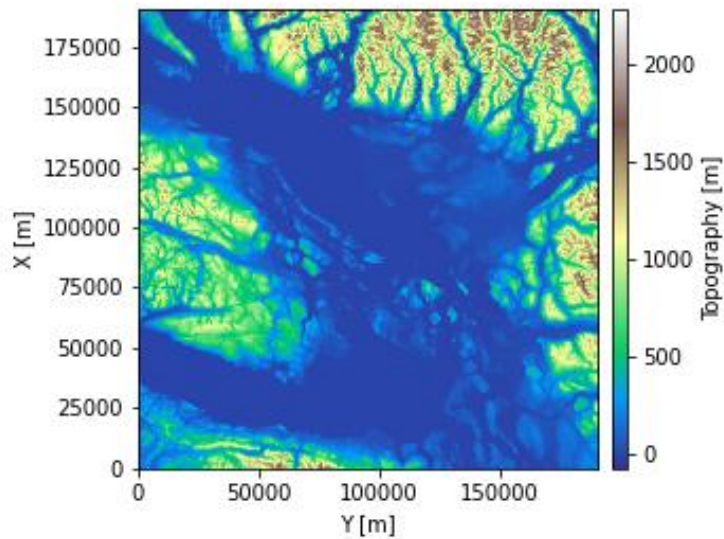


Figure 5: Topography of the GVA simulation domain, showing very low elevations on the Georgia basins and higher elevations in the mountainous regions surrounding the GVA.

SW4 has the capability to conduct MR on the grid mesh, which allows the grid mesh to have refined spacing in the upper sediment layers while keeping the mesh size larger for the lower rock layers. An example of a mesh refined block model is shown in Figure 6 with surface topography included. In this study, the original 250-m uniform grid of the Molnar (2011) velocity model is altered by SW4's MR to a grid spacing of 62.5 m in the upper 2000 m and 125 m from 2000 - 4000 m depth with the original 250 m gridding

maintained below 4000 m. MR allows for higher frequency waves to be simulated via equation 2.6, which can make the ground motions more realistic. The depths at which MR layers are introduced are chosen through trial and error, since MR can increase the computation time for simulations, making it unfeasible to place MR layers too deep. This is evident in Table 2, which shows increasing computational resources and computation time as topography and MR are included for different simulations.

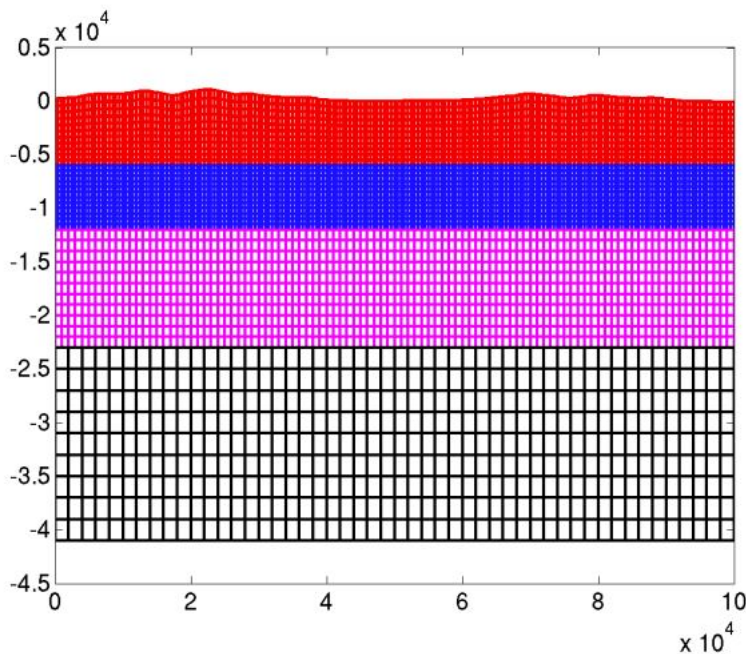


Figure 6: An example velocity model with two MR layers (at -12500 and -22500 m) and a topography layer (-5000 to >0 m). Retrieved from Petersson and Sjogren, (2012).

The SW4 FD code is run on the CPU Graham cluster of SHARCNET, a high-performance computing (HPC) network of Compute Canada. Table 2 provides further details on the computational resources needed to run each group of simulations and shows that simulations with further MR or deeper MR would not be feasible.

Table 2: Computational resources used for numerical simulations.

Simulation type	Resources (memory/CPU)	Time (hours)	Number of Tasks	f _{max}
Shallow crustal sources with mesh refinement and topography	20400	21-23	20	2 Hz
Shallow crustal sources with topography	16400	12-15	20	0.5 Hz
Shallow crustal sources without topography	16400	10-12	16	0.5 Hz

2.3: 3D Physical Structure Model

The elastodynamic equations of motion are solved from initiation of a source model within a 3D grid mesh of the physical structure (velocity) model which determines how quickly seismic waves will travel in the subsurface. The physical structure models used in this study's simulations are extracted from the Molnar (2011) southwest B.C. velocity model. This velocity model is a modified version of the Pacific Northwest Community Velocity Model of Stephenson (2007). Molnar (2011) updated the upper 1 km of the Stephenson (2007) velocity model in the Greater Vancouver region. This modification helped to reduce the overprediction of long-period ground motions of the 2001 M6.8 Nisqually, Washington, earthquake from a factor of 2.1 to 1.6 in the Greater Vancouver region (Molnar et al. 2014a). The physical structure model includes the compressional and shear wave velocities (V_p and V_s , respectively) and density (ρ) at an uniform 250 m grid resolution in southwest British Columbia. The physical model is represented by six geological units (continental basin sediments, crust, and mantle; and oceanic sediments, crust, and mantle). For this study, a 78 km (y, north-south) by 62.5 km (x, east-west) by 30 km (z, depth) grid was extracted from Molnar's (2011) southwest B.C. model. The

study area ranges from -124° to -122°E longitude and 48° to 50°N latitude. The physical model used in this study is discretized into 250 m units, i.e., 800 million grid points.

2.4: Earthquake Source Model

The earthquake source model determines the rupture dynamics of the earthquake source in the simulations. The same 8 shallow crustal **M6.7** earthquake scenarios of Molnar et al. (2014b) are chosen, 8 different hypocentres capture spatial variability of such large magnitude earthquakes in the region based on historical and/or recorded seismicity (Table 3). The selection process and numbering of these scenarios is outlined in Molnar (2014b). All 8 scenarios utilize the same kinematic earthquake source (slip distribution) model of the 1994 **M6.7** Northridge, California earthquake (Wald et al. 1996) with a modification by Molnar et al. (2014b) that flips the highest slip (seismic moment) to shallower depths. Following Molnar et al. (2014b), the fault is set to a width of 17.5 km and a down-dip length of 24.5 km. The fault plane is divided into 14 sub-faults in each direction such that 196 gridded point sources are used to construct the rupture model. The total seismic moment is 1.8×10^{19} Nm, corresponding to a **M6.7** event. The strike, dip and rake are generally set to N270° E, 45° N, and 101°, respectively, with some small variation depending on the rupture location (Table 3). For each sub-fault point source, a constant rise time of 2 s is used; the short 2 s rise time is characteristic of similar thrust mechanism earthquakes such as the 1999 **M7.6** Chi-Chi, Taiwan earthquake (Molnar et al. 2014b).

The accuracy of this study's SW4 simulated ground motions (without topography) are verified by comparing with the AWP-ODC ground motions generated by Molnar (2014b). Differences in the simulated ground motions ($f_{\max} = 0.5$ Hz) would be due to the different

3D FD algorithms. The earthquake source model is input into SW4 as an SRF file, generated using the Song Rupture Model Generator (SongRMG; Song, 2016). To generate the SRF file, SongRMG uses 1-point statistics, which are the mean, standard deviation, and 2-point statistics, which is a correlation matrix containing autocorrelation and cross-correlation components, to compute statistics of kinematic source parameters. These source parameters include the slip and rupture velocity and the peak slip with Gaussian distributions. The 1- and 2-point statistics compute the point source parameters comprising the source model's sub-faults by creating a source statistics model. Once constructed, the source statistics model is randomly sampled and the selected values are input into a stochastic rupture generating model, which uses Cholesky factorization of the covariance matrix, created from the 1- and 2-point statistics, to generate the rupture model. The same rupture models as Molnar et al. (2014b) are used (e.g., hypocentre, total seismic moment, constant rise time), noting there is some randomization of source model parameters (slip distribution, rupture velocity, peak slip) via the SongRMG. No further assessment of the generated SW4 SRF source input file is performed to verify 'sameness' with the Molnar et al. (2014b) source model.

Table 3: Rupture characteristics of simulations ran in the GVA.

Scenario	Name	Distance from Vancouver (km), direction	Epicenter latitude (° N)	Epicenter longitude (° W)	Fault Details	Observed Seismicity
1	Georgia Strait, British Columbia	40, west	49.2	123.6	N270°E strike, 45° dip north, rake 101°	Cassidy et al. (2000)

2	Salt Spring Island, British Columbia	45, southwest	48.9	123.4	N300°E strike, 45° dip northeast, rake 101°	Shallow cluster
3	Skipjack Island, British Columbia	50, south	48.8	123.0	N270°E strike, 45° dip north, rake 101°	Shallow cluster
4a	Deming 1, Washington	80, east-southeast	48.9	122.2	N90°E strike, 45° dip south, rake 101°	Dragovitch et al. (1997)
4b	Deming 2, Washington	80, east-southeast	48.9	122.1	N240°E strike, 45° dip northwest, rake 101°	Dragovitch et al. (1997)
5	Victoria, British Columbia	90, south-southwest	48.5	123.3	N270°E strike, 45° dip north, rake 101°	Shallow cluster
6	San Juan Island, Washington	80, south	48.5	123.0	N270°E strike, 45° dip north, rake 101°	Balfour, Cassidy, and Dosso (2011)
7	Mt. Vernon, Washington	110, south-southeast	48.4	122.2	N270°E strike, 45° dip north, rake 101°	Shallow cluster

2.5: Presentation of 3D synthetic ground motions

Simulations including topography and without topography are first conducted for all 8 M6.7 scenarios using a uniform 250-m grid with $V_{S,\min}$ of 625 m/s ($f_{\max} = 0.5$ Hz). The same 8 M6.7 scenarios are also used to produce simulated ground motions including topography and MR in the physical structure model ($f_{\max} = 2.0$ Hz).

Various outputs are saved using SW4 for each simulation. The velocity amplitude at each grid cell for a particular time step of the simulation are saved and plotted spatially, referred to here as velocity snapshots.

The synthetic velocity time-history (waveforms) are saved for 23 select locations based on their geographic location, their proximity to important infrastructure, or their topographic variability (discussed further in Section 3.1). These 23 select locations are referred to here as seismic stations but are not instrumented seismic recording stations in reality. From the synthetic waveform, the geometric mean of the peak ground velocity (PGV) is calculated. The geometric mean is given by:

$$PGV_{geomean} = \sqrt{V_{EW}V_{NS}} \quad (2.9)$$

where V_{EW} is the maximum (peak) velocity in the East-West direction and V_{NS} is the maximum velocity in the North-South direction. The geometric mean is used to capture ground motions in both the N-S and E-W horizontal directions, as one direction may have stronger or weaker ground motions due to the rupture characteristics of the scenario and computing the mean of both directions should remove some of those effects.

PGV is converted to Modified Mercalli Intensity (MMI) using Worden and Ward (2012):

$$MMI = 2.89 + 3.16 \log (PGV)$$

(2.10)

Lower MMI values (< VI) correspond to intensity of the perceived shaking and/or non-structural damage (e.g., pictures knocked off walls) whereas higher MMI values (> VI) correspond to intensity associated with observed structural damage (e.g., chimney cracked or broken). Figure 7 shows the relationship between PGV and other measures with MMI (termed instrumental intensity in Figure 7).

PERCEIVED SHAKING	Not felt	Weak	Light	Moderate	Strong	Very strong	Severe	Violent	Extreme
POTENTIAL DAMAGE	none	none	none	Very light	Light	Moderate	Mod./Heavy	Heavy	Very Heavy
PEAK ACC.(%g)	<0.05	0.3	2.8	6.2	12	22	40	75	>139
PEAK VEL.(cm/s)	<0.02	0.1	1.4	4.7	9.6	20	41	86	>178
INSTRUMENTAL INTENSITY	I	II–III	IV	V	VI	VII	VIII	IX	X+

Figure 7: Table relating quantitative intensity measures (PGA, PGV) with qualitative intensity measures (MMI or instrumental intensity, perceived shaking, potential damage). Retrieved from Worden and Wald (2016).

Our chosen quantitative measure of the topographic effect is referred to as the topographic ratio (TR), or the relative percent difference, and is calculated as the percent difference in PGV between simulations including topography (PGV_{Topo}) and not including topography(PGV_{No_Topo}) for the same select location, i.e.,

$$TR = [PGV_{Topo} - PGV_{No_Topo}/PGV_{No_Topo}] \times 100$$

(2.11)

Chapter 3 - 3D Synthetic Ground Motions and Associated Topographic Effects up to 0.5 Hz

Chapter 3 contains the results from running WPS of the 8 shallow crustal earthquake rupture scenarios with resolved frequencies up to 0.5 Hz with and without topography. Velocity time series data of the ground motions were generated and plotted at sites of importance due to their location and nearby topography. Shot gather styled plots were generated to trace different wave packets spatially as the ground motions propagate away from the source. The PGV geometric mean with and without topography and the relative percent difference between them was calculated to quantify the effect of topography at lower frequencies.

3.1 Seismic Stations

Ground motions are generated for each of the 8 shallow crustal **M6.7** rupture scenarios outlined in Table 3 using physical structure models with and without surface topography. The 23 seismic stations at which to retrieve synthetic velocity waveforms are selected based on their elevation (peak, slope or base of hills and mountains) and/or whether important infrastructure is located near the site (representative for a local municipality).

A map of the GVA and all recording stations is shown in Figure 8. The blue markers show the location and name of the selected seismic station. The yellow markers are locations with important infrastructure, but synthetic waveforms are not retrieved in this study. The two highest peaks, Mt. Cypress (> 1500 m above sea level in the model) and Mt. Seymour (964 m elevation), both have adjacent valleys and as a result, could display topographic resonance where the topography focuses incoming seismic waves towards

the peak, resulting in constructive interference and greater shaking. The Vancouver International Airport is of critical importance to the GVA and is located on the Georgia basin, sitting atop soft sediments that could amplify shaking (Molnar 2014a; 2014b). Topographic lows can receive de-amplification due to surrounding topography defocusing seismic waves away from lower elevations to higher peaks. Although the airport has a low elevation of 20 m, de-amplification is unlikely to occur due to the airport's large distance from topographic highs. The cities of Delta and Richmond are also low-lying areas with elevations of 8 m and 10 m, respectively. They have soft Fraser River delta sediments with significant civilian populations and expensive infrastructure in the region. They can also act as a reference point without topography since they are located around sea level. UBC is located on the Vancouver Uplands at an elevation of 134 m, significantly higher than nearby Delta and Richmond. Vancouver stations in nearby low elevation areas could act as a valley relative to the hill that UBC is located on, resulting in topographic amplification. Burnaby is located further inland and sits on firmer soils than Richmond or Delta, with a higher elevation of 45 m. The topographic response in Burnaby is of interest due to mountains to the north and closer to the east, since these mountains (narrowing of the Fraser Valley) could trap seismic waves. Most of Downtown Vancouver has a significant seismic risk due to the expensive infrastructure and a large civilian population living in the area, so ground motions need to be accurately modelled in the area including topography. There are also some nearby topographic highs such as Stanley park that could trap some seismic energy and channel it towards Downtown. West Vancouver has a large civilian population and sits below Mt. Cypress, which could cause de-amplification from the nearby mountain, or trapping of seismic waves from the

nearby mountains, causing amplification. Five stations (referred to as Point 1-5) at varying elevations along Mt. Cypress are chosen to provide a SW traverse since they are geographically located close together, but with large changes in topography. A traverse of close seismic stations permits detailed study of the effect topography has on shaking while eliminating most effects from moving the recording station closer or further from the rupture source.

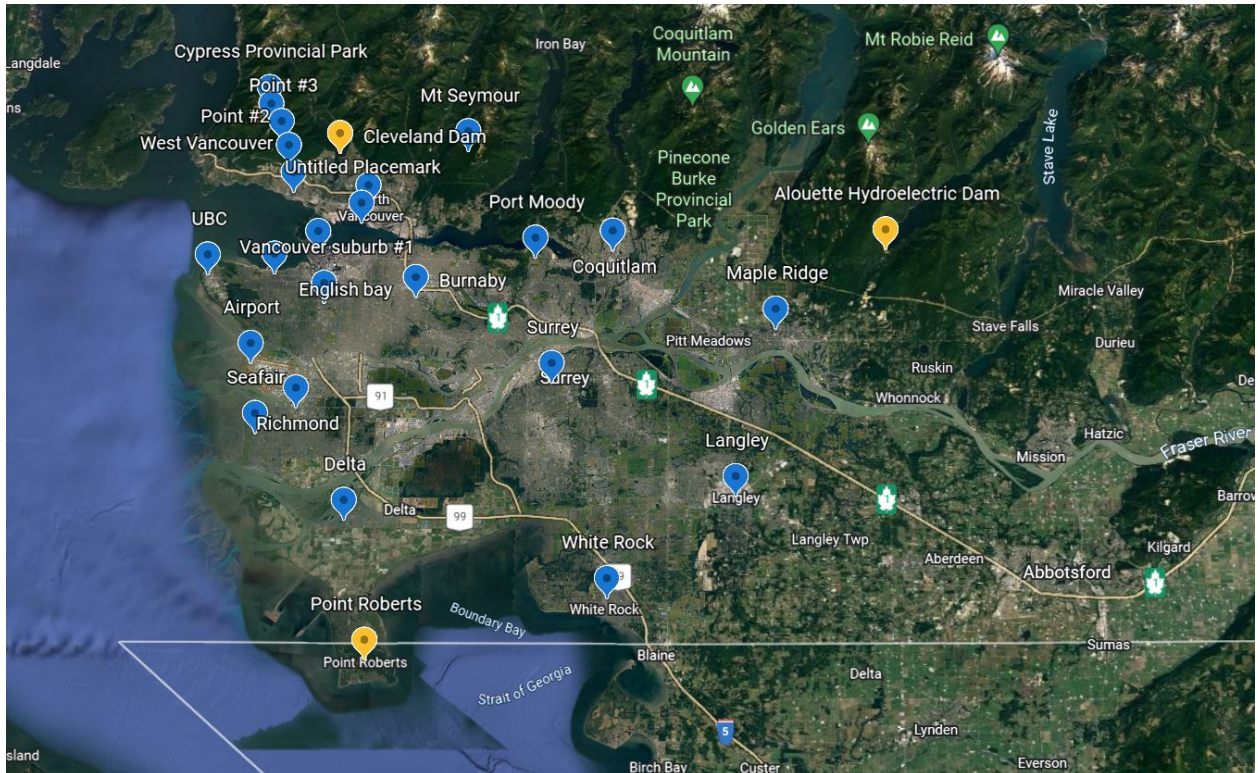


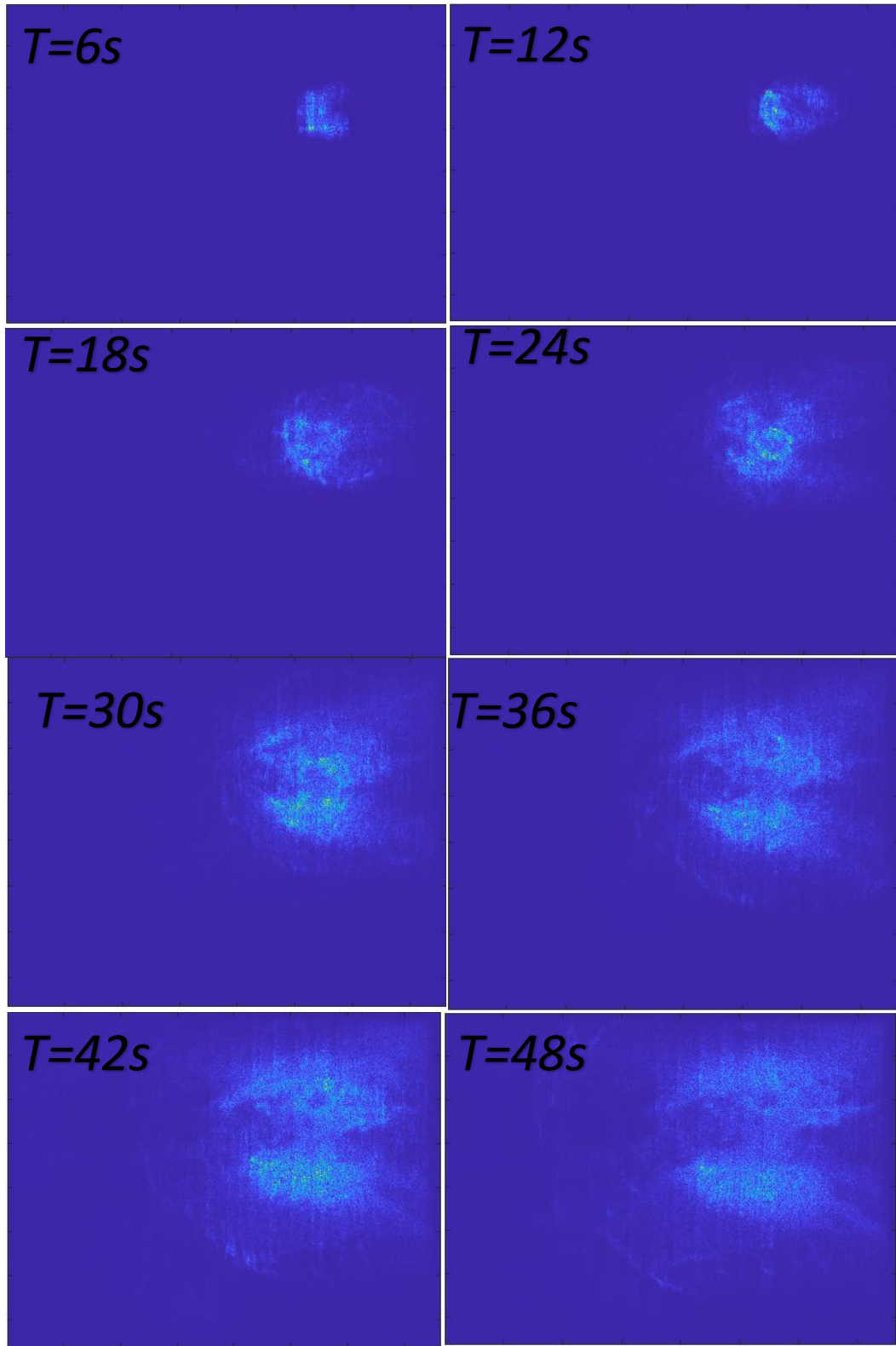
Figure 8: Map of recording stations in the shallow crustal scenarios. The blue markers indicate sites where velocity ground motions were recorded. The yellow markers are other interesting sites that are out of the scope of the study but have important infrastructure nearby.

3.2 Velocity Ground Motion Recordings – 0.5 Hz Resolved Frequency

Numerical simulations were run with and without topography, with a maximum resolvable frequency of 0.5 Hz. To verify the ground motions generated from the

simulations had reliable results, the average PGV geomean of the Georgia Strait scenario without topography was compared to the average from Molnar (2014b). The ground motion simulations of the Georgia Strait scenario in Molnar (2014b) had an average PGV geomean of 15.7 cm/s across Vancouver. The average value over the 23 different sites in the GVA in this study was calculated, with a value of 11.3 cm/s without topography. Any difference between this value and Molnar (2014b) is likely due to different methods of computing the rupture files (SRF) and different FD schemes used for the simulations.

Figure 9 shows an example of the ground motions generated from these numerical simulations, specifically from the Georgia Strait scenario described in Table 3. This scenario is closest to the GVA and had less effects caused by rupture azimuth and location than some other sites. The simulations were run for 70 seconds to capture as much shaking duration as computationally possible, and each image is a snapshot of the propagating seismic waves at 6-7 second intervals. Due to the rupture azimuthal direction that was chosen for most of the scenarios, waves appear to primarily propagate in the N-S directions.



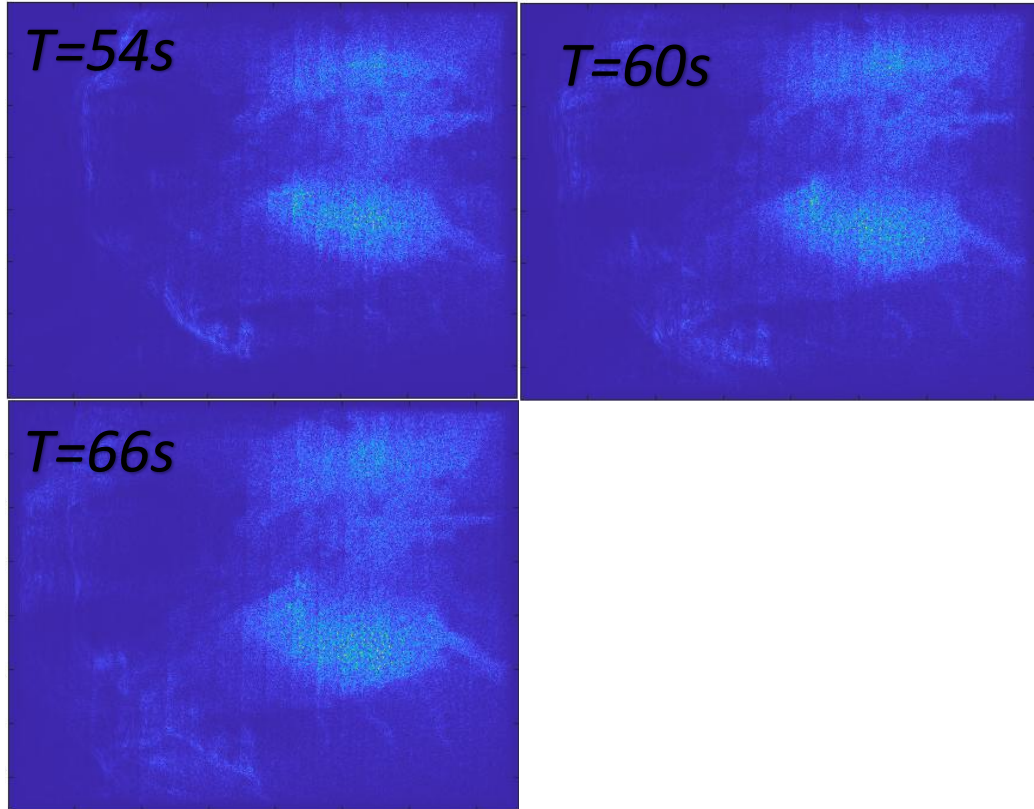


Figure 9: The propagation of the ground motions away from the Georgia Strait rupture from time $t = 5$ seconds until $t = 70$ seconds.

Frequencies above 0.5 Hz were filtered out of the ground motions recordings at the sites described in Figure 3 using a low-pass filter, with a sampling rate of 30 samples per second. The velocity time series data was then plotted and the geometric mean of the PGV max in the horizontal directions (E-W, N-S) was calculated for each of the sites.

The velocity ground motions generated by the Georgia Strait scenario simulation, with and without topography at Mt. Cypress, Delta, Mt. Seymour, and Richmond are plotted in Figure 10a, 10b, 10c, and 10d, respectively. The simulations without topography (black) at the Mt. Cypress site in Figure 10a have higher amplitude ground motions in the horizontal and vertical directions, particularly in the E-W direction, where a large amplitude signal is present at around 20 seconds in all 3 directions. The same signal is

present with topography, but the amplitude of the arrival is significantly lower by a factor of about 5. Since most of the amplification should be present at higher frequencies, the ground motions are lower than simulations without topography. The velocity ground motions for the Georgia scenario at the Delta station, shown in Figure 10b, shows that the ground motions had higher amplitudes when including topography in the E-W horizontal direction and were nearly identical to simulations without topography in the N-S and vertical directions. This could be because the topographic effect is very minimal at the low elevation of the Delta station, so the difference in ground motions when including topography is not much different to those simulations without topography (only 20m higher elevation). At higher frequencies, there should be a much smaller increase due to topography when compared to higher elevation sites.

The Georgia Strait Scenario velocity ground motions, with and without topography at the Mt. Seymour site, is shown in Figure 10c. Like the ground motions at the Mt. Cypress site, the ground motions show de-amplification when topography is included at lower frequencies. This could be caused again by the effects of topography affecting more high frequency waves, causing the ground motions to be lower than simulations without topography. The ground motions display significant amplification with topography in the E-W direction while having slightly lower amplitude ground motions in the vertical direction and the N-S direction, which could be caused by the azimuth and location of the source as ground motions are highly source dependent, or the axis of elongation of Mt. Seymour, which is in the N-S direction and therefore not orthogonal to the N-S ground motions. Since the a given structure receives maximum amplification for waves propagating orthogonal to the axis of elongation, the E-W could have received more topographic

effects while the N-S had less. The Mt. Seymour site is also at a high elevation with a valley to the east and has the recording station located closer to the eastern ridge of the mountain. Since the slopes away from the source receive larger amplification (Khan, 2019), this could cause more amplification at this station.

The Georgia Strait Scenario velocity ground motion motions at the Richmond site are shown in Figure 10d. The ground motions show lower amplitude velocity ground motions in the E-W horizontal direction and in the vertical direction for the simulation without topography. The ground motions in the N-S direction are very similar with and without topography but slightly higher amplitude without topography. This could again be due to only low frequencies being included in these simulations.

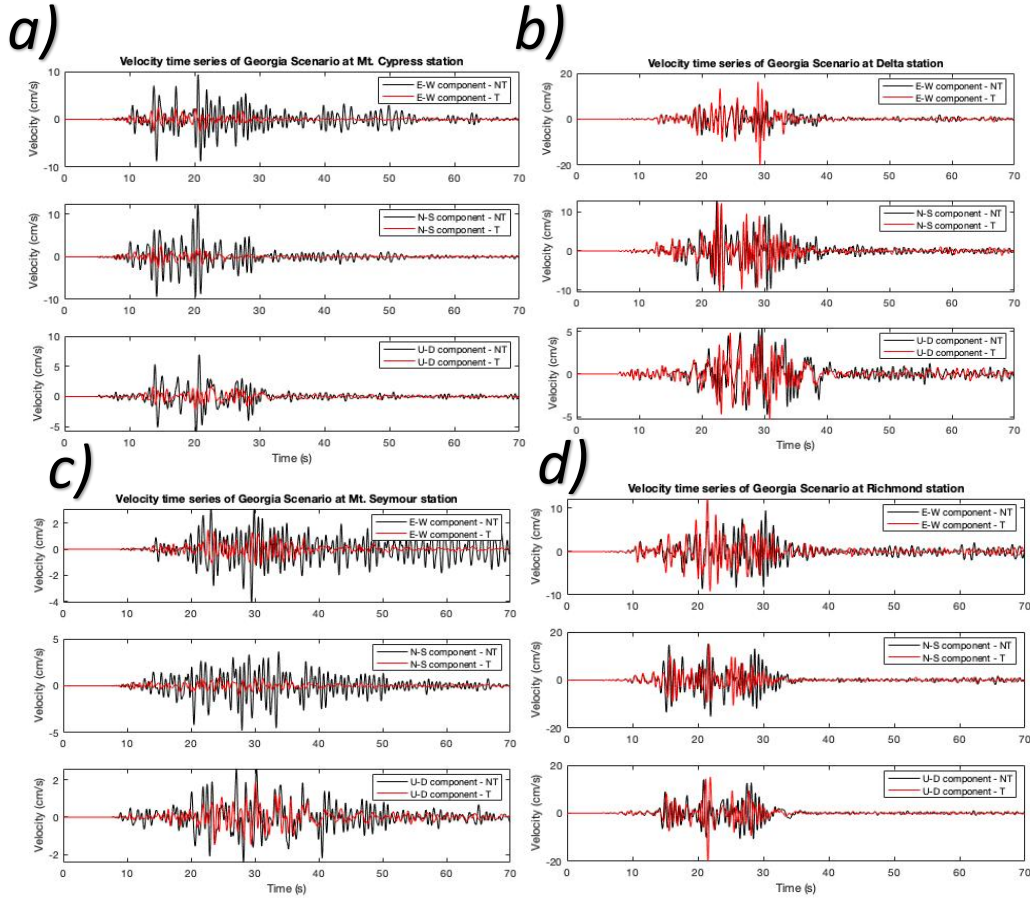


Figure 10: Velocity ground motions at several seismic stations with and without topography at resolvable frequencies up to 0.5 Hz for the **(a)** Mt. Cypress site. **(b)** Delta site. **(c)** Mt. Seymour site. **(d)** Richmond site.

Velocity time series data plotted as a “shot gather” of the ground motions in the E-W horizontal direction are plotted in Figure 11a, 11b, 11c, and 11d for the Deming 1, Mt. Vernon, Deming 2, Georgia Strait scenarios, respectively. A shot gather is a display of seismic traces side-by-side that have a common acquisition parameter, which in this figure is the same source. The data are plotted in order as a function of distance from the epicentre of the rupture, with the bottom time series in each shot gather, Delta, having approximately the shortest distance from the epicentres while the velocity time series at the top, Point 5 at the peak of Mt. Cypress, having the greatest distance from the epicentre. Plotting data as a shot gather allows various arrivals to be traced across

seismic recording stations more easily. The Deming 1 rupture scenario has the clearest arrivals out of these four scenarios, with clear P-waves arriving at about 20-28s depending on distance from the source, and S-waves arriving between 25-35s. Other surface waves arrive later, between 35-45s and brought the highest amplitude ground motions. All arrivals are more clearly defined in the scenario without topography, as topography can add increased complexity to the ground motions.

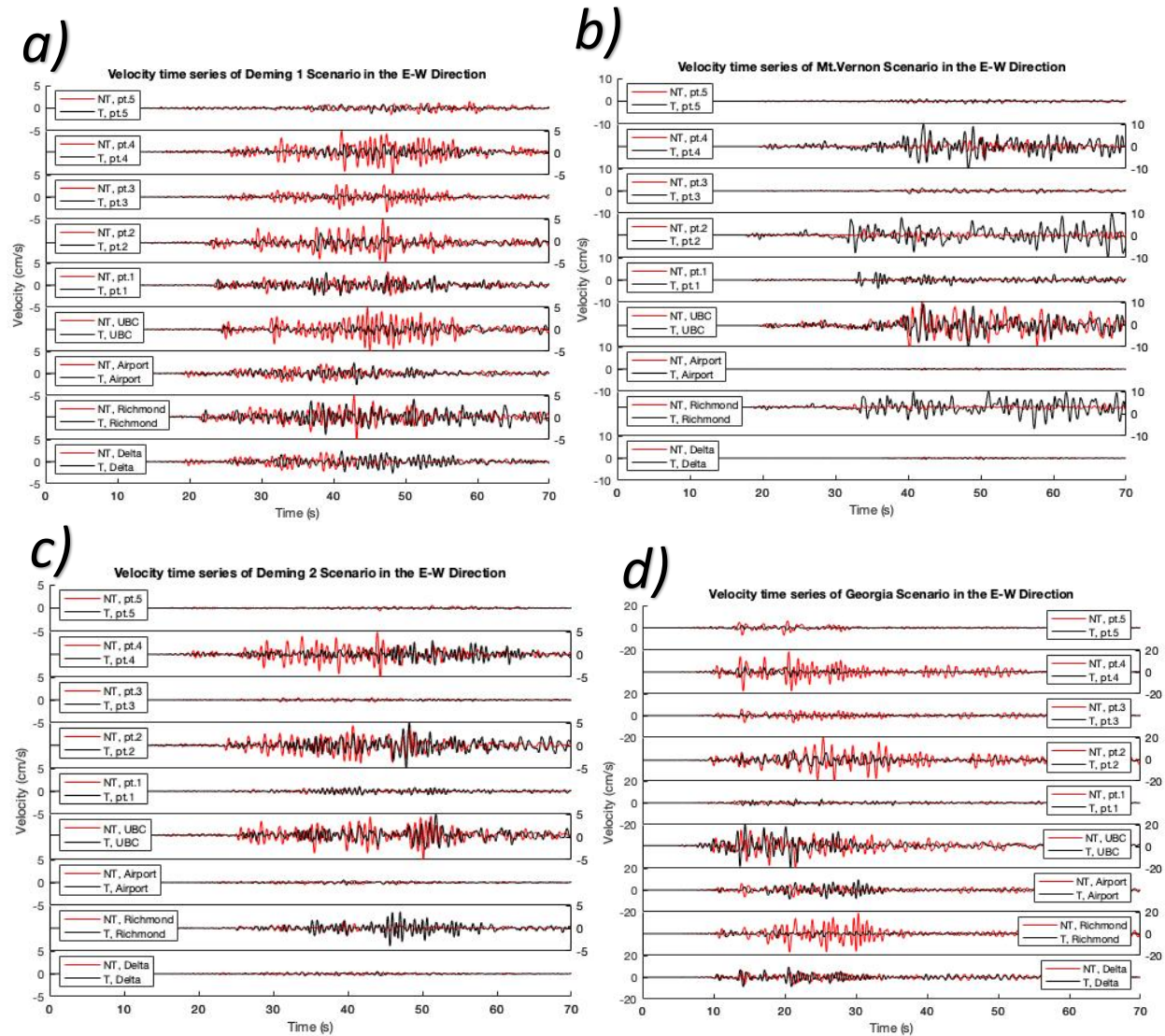


Figure 11: Shot gather plot ground motions for the Deming 1 (**a**), Mt. Vernon (**b**), Deming 2 (**c**), and the Georgia Strait (**d**) scenarios.

Velocity time series data plotted as a “shot gather” of the ground motions in the E-W horizontal direction are plotted in Figures 12a, 12b, 12c, and 12d for the San Juan Island, Skip Jack, Victoria, and Salt Spring Island scenarios, respectively. The Salt Spring Island scenario has clear P-wave first arrivals starting at the Delta station at 10s and ending on the peak of Mt. Cypress at about 25s. There are clear S-waves about 5-8s after the P-wave first arrivals. The scenario without topography has much larger ground motions, and arrivals are unclear for scenarios with topography due to the low amplitude of most of the waves.

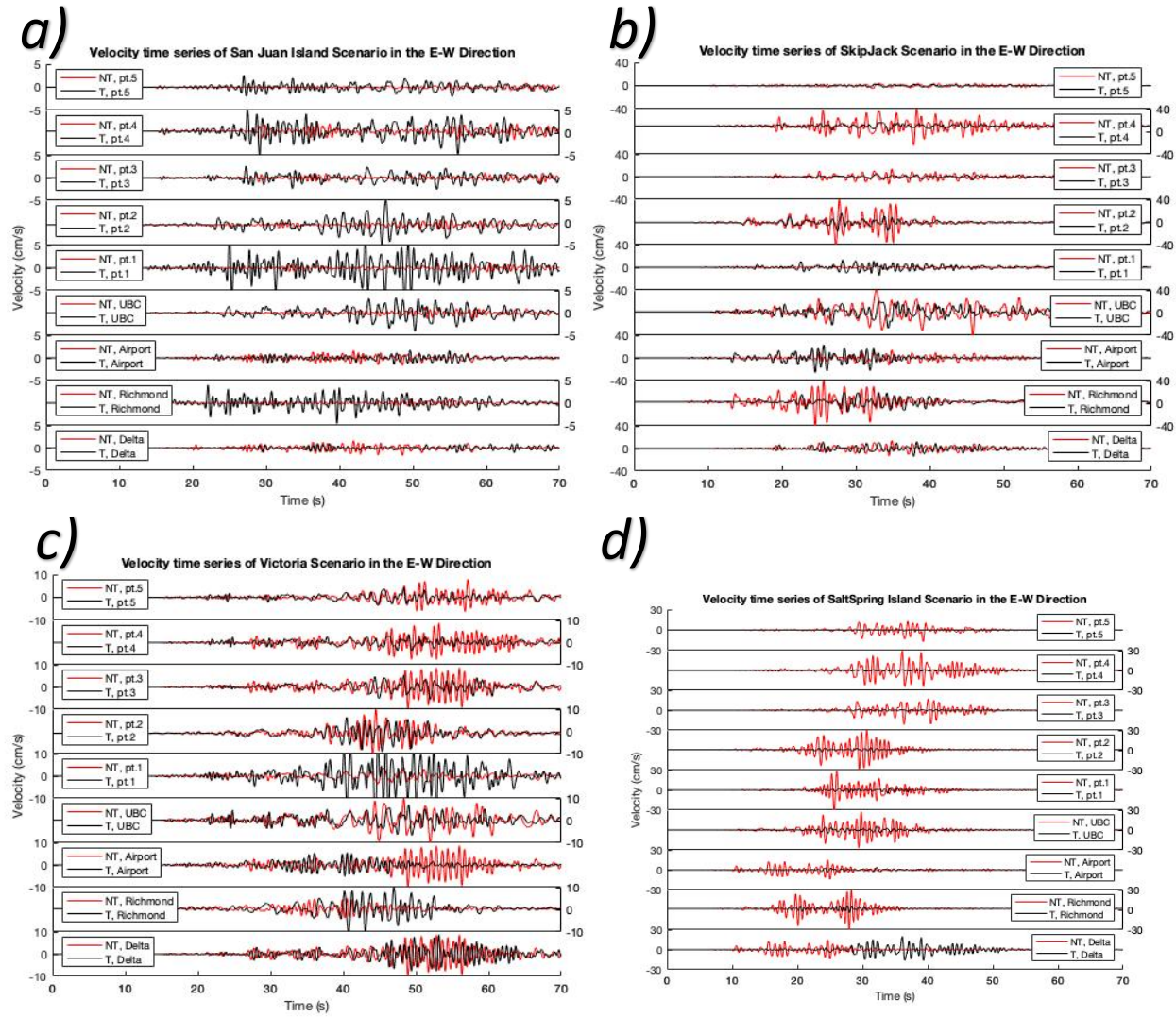


Figure 12: Shot gather plot ground motions for the San Juan Island **(a)**, Skip Jack **(b)**, Victoria **(c)**, and Salt Spring Island **(d)** scenarios.

3.3 PGV Geomean and Relative Difference in PGV – 0.5 Hz Resolved Frequency

The geometric mean of the PGV in the horizontal directions was calculated for each of the 8 scenarios at 8 sites of interest, with and without topography, and are shown in Table 4 and Table 5, respectively. These sites are at the Vancouver International Airport, Burnaby, Mt. Cypress, Mt. Seymour, Delta, Richmond, Downtown Vancouver, UBC, and West Vancouver. The relative percent difference between simulations with and

without topography were then calculated and are shown in Table 6. A negative difference in Table 6 indicates the ground motions were less with topography than without topography (received potential topographic de-amplification).

The computed results are highly dependent on the rupture scenario, which is to be expected as topographic resonance was determined to have a high degree of variability below the 1 Hz frequency range (Boore, 1972) and heavily depend on the rupture location (Stone et al., 2022). The Georgia Strait scenario displays lower amplitude ground motions and possibly de-amplification at most notably the hard soil, higher elevation sites of Mt. Seymour and Mt. Cypress, where the PGV geomean of the simulations are 72% and 76% less than simulations without topography, respectively. The soft soil and low elevation sites displayed the opposite, with the soft soil, low elevation sites of Delta and Richmond having increases in PGV Geomean for simulations with topography versus those without, with an increase of 51% and 11%, respectively. Typically, sites that are at higher elevations would be expected to have higher ground motions due to the topographic effect at those elevations, while low lying areas should have a very marginal increase in PGV or a decrease due to topography. As previously described, the higher frequencies are where most topographic amplification occurs, so the mountainous sites should have more amplification when higher frequencies are included. The combined effect of being located on hard soils and hard rock while also not having topographic amplification could be causing the mountain sites to have unrealistically low ground motions. The results of the Georgia Strait simulations show the effect that frequency content, source location, and azimuth can have on simulations. Not including higher frequencies and the choice of

specific sources and rupture locations created a notably different outcome than would be expected.

The Victoria scenario showed an increase in PGV with topography at 6/8 stations, with particularly large increases at Burnaby (+137%) and Downtown (+150%) with topography versus without. The higher elevation sites again displayed de-amplification and lower PGV values, with UBC, Mt. Cypress, and Mt. Seymour having 18%, 61%, and 31% drops in PGV when topography was included versus without. This is again likely due to the inclusion of only low frequency content in the simulations, removing the topographic effect that would otherwise occur if higher frequencies were resolved in the simulations.

The Salt Spring Island scenario shows significantly lower PGV values at all stations in simulations including topography. The decrease in PGV when including topography was 69-95% at the chosen sites. This could be a result of the rupture mechanism, as the strike of the fault was N300E instead of N270E that 6 of the other scenarios were, and topographic effects are highly dependent on rupture azimuth, frequency and geographic location. The local topography on Salt Spring Island could have also been a factor in de-amplifying the ground motions at the source, and some mountainous areas on the island could have shielded the regions beyond them to the northwest by reflecting some ground motions away from the GVA.

The Mt. Vernon, Washington scenario showed massive amplification of seismic waves at all sites, with amplification due to topography ranging from 137%-1507%. This could be because Mt. Vernon is surrounded by large mountains such as Mt. Baker and the North Cascades Mountain range to the East all the way up to Vancouver. As mountains have been shown to scatter surface waves away from them, shielding the

areas beyond (Ma et al., 2007), this could trap and amplify seismic waves in the GVA and in the west towards the ocean, causing amplification of ground motions. The mountainous, high elevation regions such as Mt. Cypress and Mt. Seymour again showed significantly less of an increase in PGV when topography was included when compared to some of the low elevation sites, which had up to 10 times the increase.

The San Juan Island Scenario also showed large amplification of seismic waves in the topographic simulations at all recording station, with amplification ranging from a 79% increase in PGV when topography was included for the Mt. Seymour scenario compared with a 584% increase including topography for the Delta scenario. Some reasons for this large amplification could include the local topography on San Juan Island, which is hilly with a maximum elevation of 329 m. This could have caused amplification of the earthquake near the source, resulting in ground motions that are larger and propagate further than without topography. The geographic location of the source may have also influenced the amount of amplification that was evident in this scenario.

The Deming, Washington scenarios (Deming1 and Deming 2) had different rupture characteristics, while having the epicentre geographically nearby. Deming 1 had a N90E strike and a 45-south dip, in contrast to Deming 2, with a N240E strike and a 45-northwest dip. Deming 2 had amplification due to topography at all stations that were not at higher elevations (Mt. Cypress, Mt. Seymour, UBC) with amplification ranging from 51%-206% for the low-lying areas and decreases in the higher elevation areas of -14% at UBC to -60% at Mt. Cypress. Deming 1 had a more broadly decreases in PGV with topography, aside from Delta and West Vancouver stations, which had very small positives. The mountainous sites such as Mt. Cypress, UBC, and Mt. Seymour experienced de-

amplification, such as -69% for Mt. Seymour and -65% for Mt. Seymour. The lower lying areas such as Richmond and Delta had de-amplification when topography was included, but less so, with much smaller decreases in PGV when topography was included. The Deming 2 scenario may have had similar effects as the Mt. Vernon scenario and saw the trapping and amplification of seismic waves due to the North Cascades to the east and similar subsurface structures as Mt. Vernon. Deming 1 also had a different azimuth and dip for the fault, which could account for some of the computed PGV values

Table 4: PGV Geomean of the 8 scenarios at 8 recording stations with topography included.

Site	Georgia	Salt Spring Island	San Juan Island	Skipjack Island	Mt. Vernon	Deming 1	Deming 2	Victoria
Airport	9.38	5.35	6.76	24.3	3.91	1.98	0.62	14.6
Burnaby	5.28	2.76	6.83	8.88	7.21	3.42	0.99	9.4
Cypress Mountain	2.64	0.98	2.91	4.05	1.35	0.86	0.71	3.39
Delta	15.76	16.14	7.65	19.6	0.42	1.88	1.47	8.69
Downtown	5.87	19.56	6.55	8.42	0.45	3.72	1.33	19.6
Richmond	13.38	25.42	6.52	36.21	0.48	2.51	1.55	10.27
Mt. Seymour	1.24	11.03	2.53	2.16	0.64	2.96	0.36	2.96
UBC	3.30	21.33	3.21	9.84	0.51	2.35	0.66	9.42
West Vancouver	9.62	17.62	6.93	9.02	0.69	2.90	1.37	15.75

Table 5: PGV geomean for the 8 scenarios at 8 recording stations without topography.

Site	Georgia	Salt Spring Island	San Juan Island	Skipjack Island	Mt. Vernon	Deming 1	Deming 2	Victoria
Airport	12.24	19.69	1.30	33.4	0.43	2.11	1.89	10.38
Burnaby	4.93	23.69	1.31	9.4	0.65	3.77	1.49	3.98
Cypress Mountain	10.8	20.87	0.96	11.3	0.57	2.79	0.31	8.72
Delta	10.4	16.14	1.32	23.9	0.42	1.88	1.47	3.97
Downtown	7.65	19.56	1.31	10.8	0.45	3.72	1.33	7.85
Richmond	12.0	25.42	1.32	23.67	0.48	2.51	1.55	4.73
Mt. Seymour	4.42	11.03	1.41	8.33	0.64	2.96	0.36	4.27
UBC	6.96	21.33	1.47	17.27	0.51	2.35	0.66	11.5
West Vancouver	6.99	23.03	1.38	10.87	0.69	2.90	1.37	7.0

Table 6: Relative percent difference between simulations with and without topography. Negative values indicate a decrease in PGV when topography is included, and a positive number indicates an increase in PGV when topography is included.

Site	Georgia	Salt Spring Island	San Juan Island	Skipjack Island	Mt. Vernon	Deming 1	Deming 2	Victoria
Airport	-20	-72	419	-27	812	-7	206	40
Burnaby	7	-88	423	-5.5	1006	-9	51	137
Cypress Mountain	-76	-95	203	-64	137	-69	-57	-61
Delta	51	-82	584	-18	649	2	138	118
Downtown	-23	-80	504	-22	1507	-27	60	150
Richmond	11	-78	506	53	751	-13	151	116
Mt. Seymour	-72	-93	79	-74	176	-65	-60	-31
UBC	-53	-84	232	-43	357	-057	-14	-18
West Vancouver	29	-69	472	-17	955	3.3	92	125

3.4 Modified Mercalli Intensity Ratings – 0.5 Hz Resolved Frequency

MMI at a site is a measure of the perceived shaking found at that site and was calculated at important locations for the Georgia Strait scenario, shown in Table 7. The Georgia Strait scenario was chosen out of the 8 scenarios for visualization as it is closest geographically to the GVA and appears to have less source specific ground motions generated, in contrast to others such as the Mt. Vernon scenario. Most sites are expected

to have significant perceived shaking for this scenario, with most experiencing strong or very strong shaking with some light damage. Other significant scenarios with high perceived shaking include for the Skip Jack Island and Salt Spring Island scenarios, where the Richmond site is expected to have strong shaking with light-moderate damage.

Table 7: MMI for the Georgia Strait at select sites shows moderate to strong shaking at most sites, with correspondingly light to moderate damage.

Site	Perceived Shaking with topography	Perceived shaking without topography
Airport	VI (Strong)	VI (Strong)
Burnaby	V (Moderate)	V (Moderate)
Cypress Mountain	IV (Light)	VI (Strong)
Delta	VI (Strong)	VI (Strong)
Downtown	V (Moderate)	V (Moderate)
Richmond	VI (Strong)	VI (Strong)
Mt. Seymour	IV (Light)	IV (Light)
UBC	IV (Light)	VI (Moderate)
West Vancouver	VI (Strong)	VI (Moderate)

Chapter 4 - 3D Synthetic Ground Motions and Associated Topographic Effects up to 2 Hz

Chapter 4 are the results from running the numerical simulations of the shallow crustal earthquake rupture with resolved frequencies up to 2 Hz with topography compared to the 0.5 Hz simulation without topography. Time series of the velocity ground motions were generated and plotted at sites of importance due to their location

and topography. Shot gather styled plots were generated to trace different wave packets spatially as the ground motions propagate away from the source. The PGV geometric mean with topography and the relative percent difference between the topographic and 0.5 Hz non-topographic simulation was calculated to quantify the effect topography could have at higher frequencies. The ground motion amplitudes at different frequencies with topography at 2 Hz was computed by taking the Fourier Transform of the acceleration ground motion data and the HVSR was calculated to compare with the 0.5 Hz simulations.

4.1 Velocity Ground Motion Recordings – 2 Hz Resolved Frequency

Topographic resonance increases with increasing frequency, which increases the importance of utilizing methods and techniques to model the ground motions at higher frequencies. Modelling ground motions at higher frequencies can be computationally expensive, limiting how high the resolved frequency in the 3D WPS can be. MR at 2000 m and 4000 m was implemented with simulations including topography, increasing the maximum resolved frequency in the simulations to 2 Hz from 0.5 Hz in chapter 3. These depths for the MR layers were chosen as thin MR layers can decrease model stability. Thinner layers and simulations without topography at higher frequencies can be experimented with in future studies to allow for higher frequency ground motions to be generated while still limiting the computational cost.

Velocity ground motions were modelled with topography and MR and were compared to the simulations without topography and MR from the previous chapter in Figures 13a, 13b, 13c and 13d at the Delta, Mt. Cypress, Richmond, and Mt. Seymour

sites, respectively. The ground motions at the Delta site show higher amplitudes in simulations with MR than simulations without it in the N-S and vertical directions. The E-W direction shows slightly lower amplitude ground motions with MR, particularly at 25-30s, and at 15-20s, the MR simulations showed higher amplitude ground motions. Allowing ground motions from up to 2 Hz allowed more energy to pass through into the time series data, as the 0.5 Hz ground motions had this energy cut out due to the low pass filter. The ground motions in the E-W direction are similar and well aligned with each other, with peaks appearing at the same time in the two sets of simulations, just with slightly higher amplitudes without MR.

At the Mt. Cypress and the Mt. Seymour sites, all directions show a significant increase in the velocity ground motion amplitudes, in contrast with the E-W at the Delta station which showed a decrease in amplitudes when MR was included. This may be because the topographic effect caused more amplification in the direction of the Mt. Cypress station than the Delta station due to its elevation and proximity to nearby valleys to the East, West and the Georgia Strait to the South of the mountain. These valleys and the Georgia Strait could cause trapping and refraction of ground motions towards the peak of Mt. Cypress. Since the Delta scenario is at low elevation and will not receive topographic amplification, but potentially de-amplification, it did not receive the same large increase in ground motions due to topography as the Mt. Cypress site.

At the Richmond site, all directions show increased amplitude ground motions with MR than without it. This is most likely due to the low-pass filter of the 0.5 Hz limited the energy shown received at the site, but more unexpected than the amplification at Mt. Cypress, since mountainous regions are expected to have more topographic amplification

and it is expected for Richmond to behave similarly to Delta. Richmond is located at lower elevations and is already experiencing a significant basin effect due to its location on the Georgia Strait. The amplification seen here should cause re-evaluation of whether the topographic effect should be included in future studies in these basin regions, since the amplification at higher frequencies in simulations with topography was high and they already have a high seismic risk.

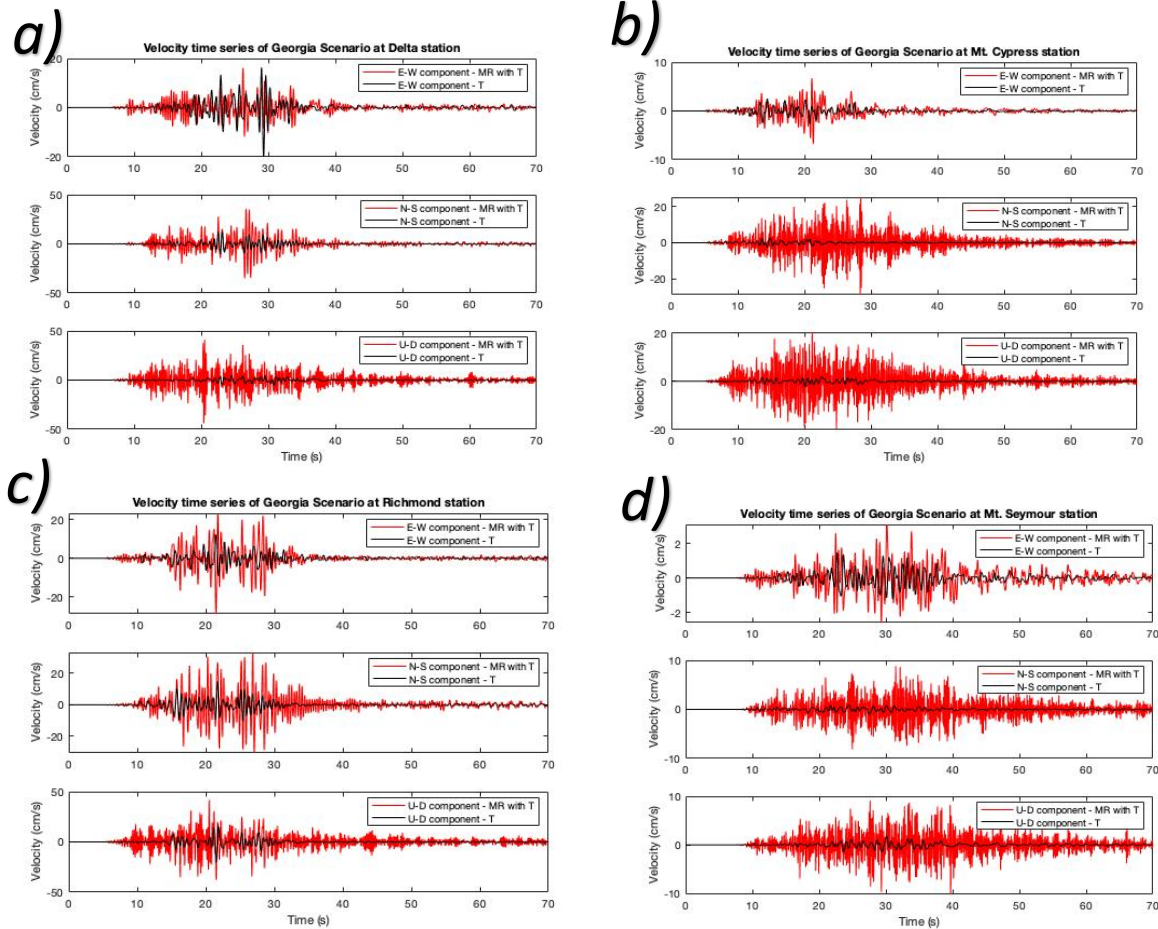


Figure 13: (a) Georgia Strait scenario velocity time series at the Delta station. (b) Georgia Strait scenario velocity time series data at the Mt. Cypress station. (c) Georgia Strait scenario velocity time series data at the Richmond station. (d) Georgia Strait scenario velocity time series data at the Mt. Seymour station.

Velocity time series data plotted as a “shot gather” of the ground motions in the E-W horizontal direction are plotted in Figures 14a, 14b, 14c, and 14d for the Georgia,

Deming 1, Deming 2, and the Mt. Vernon scenarios, respectively. Due to the various competing effects from topography, the basin, and attenuation, there is highly complex waveforms after 30 seconds in all scenarios. The first arrivals from the P-waves in all scenarios appear to arrive between 10-15 seconds, with very little difference in arrival time due to the distances from the source being small. The Mt. Vernon scenario shows the largest distance between sources, and as a result, the first arrivals arrive much later (~5 seconds) at the peak of Mt. Cypress compared to Delta. The Mt. Vernon and Deming 1 scenarios have the clearest S-wave arrivals at about 20-25s and 25-30s, respectively. The Georgia Scenario has the longest duration of high amplitude ground motions, with several stations having approximately 15-20 seconds of ground motions in excess of 20cm/s. While the duration of shaking is long for the Deming 1, Deming 2 and Mt. Vernon scenarios, the amplitude of shaking is up to 400% less than that of the same station from the Georgia Strait scenario due in large part to the increased distance of the rupture from the seismic stations.

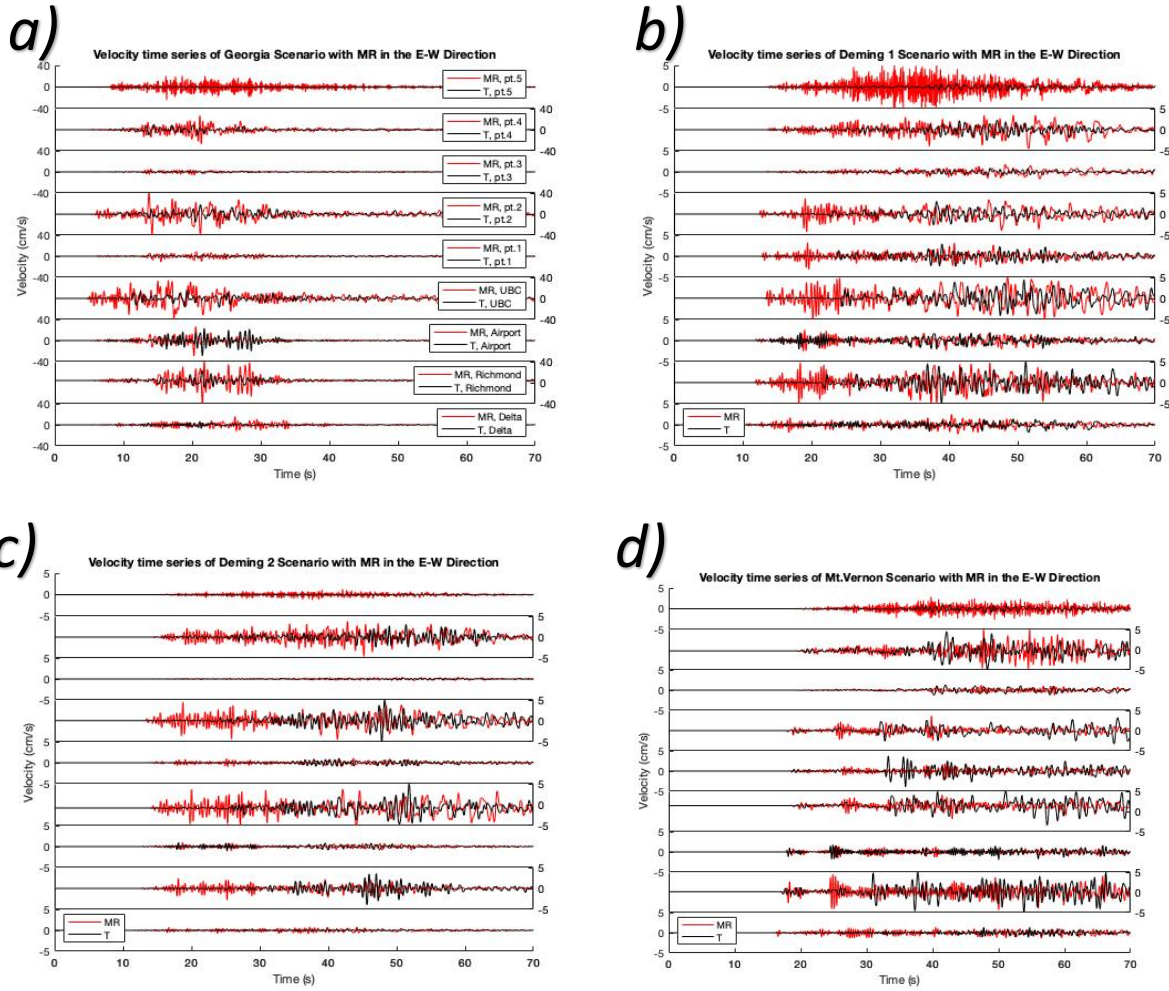


Figure 14: (a) Georgia scenario velocity ground motions recorded at the Delta, Richmond, Airport, UBC, Pt. 1 (West Vancouver), Pt. 2, Pt. 3, Pt. 4 and Pt. 5 (Mt. Cypress peak) stations in the E-W direction with and without topography. Simulations without MR have much lower amplitude ground motions than those with MR. (b) The Deming 1 scenario. (c) The Deming 2 scenario. (d) The Mt. Vernon scenario.

4.2 Velocity Amplitude Maps of the Greater Vancouver Area

SW4 takes a recording of the velocity at each point at user set time intervals, then records the values as a rudimentary image that can be used to construct a map of the velocity amplitudes at various time periods as an output. Figures 15-22 show snapshots of these velocity amplitudes for all 8 rupture scenarios. The time interval selected was the values at 34 seconds, since this time period had approximately the highest amplitude

waves in the velocity time series as well as when compared to 9 other possible time periods. Figures 15a and 15b show velocity amplitude maps for the Victoria rupture scenario with and without topography, respectively. There is increased amplification in simulations including topography, with ground motions exceeding 300 cm/s a greater distance away from the source than without topography. This could be due to higher elevations, such as mountains, near the rupture site to the west on Vancouver Island trapping and reflecting these waves back. This could also increase the ground motion amplitude near the rupture site. Figures 16a and 16b show the velocity amplitude maps for the Georgia Strait rupture scenario with and without topography, respectively. The maps have similar velocity amplitude values, with values near the source exceeding 300 cm/s and values in the GVA reaching >30 cm/s in same areas.

Figures 17a and 17b show the velocity amplitude maps for the Mt. Vernon rupture scenario with and without topography, respectively. The simulations without topography had much lower amplitude ground motions when compared to the simulation with topography. This rupture scenario appears to have significant effects caused by not only the location and geography of the rupture, but also the topography at the epicentre, with the inclusion of topography in this scenario having much larger ground motions at the epicentre than without topography. This indicates that for this scenario, the inclusion of topography not only affects the propagation and amplification of waves further from the source, but also directly at the epicentre.

Figures 18a and 18b show the velocity amplitude maps for the Deming 1 rupture scenario with and without topography, respectively. The Deming 1 scenario is closer to the GVA than the Mt. Vernon scenario to the north, so has stronger ground motions in the

GVA. The Deming 2 scenario is shown in Figures 19a and 19b. The Deming 1 scenario has much higher ground motions at the rupture site when compared to Deming 2, with the location of the rupture nearly the same but with differing rupture azimuth, indicating that any difference between these two scenarios is almost exclusively due to the rupture azimuth.

Figures 20a and 20b show the velocity amplitude maps for the Salt Spring Island rupture scenario with and without topography, respectively. The velocity ground motion amplitude is much larger without topography than with topography, and significant energy reaches the GVA due to the rupture azimuth and location channeling more energy towards the GVA, with ground motions of upwards of 30 cm/s seen in the GVA. This is contrasted with Figures 21a and 21b, which are the velocity amplitude maps for the San Juan Island rupture scenario. Larger velocity ground motions are generated in the simulations without topography than with topography, but since San Juan Island is one of the furthest scenarios from the GVA, a limited amount of energy reaches Vancouver. Figures 22a and 22b show the velocity amplitude maps for the Skip Jack Island rupture scenario with and without topography, respectively. This rupture scenario has a large amount of energy reaching the GVA, with velocity ground motions exceeding 20 cm/s in some areas but has much lower ground motions with topography included. The velocity amplitude maps shown in Figures 15-22 were selected from Figures 27-42 in the appendix.

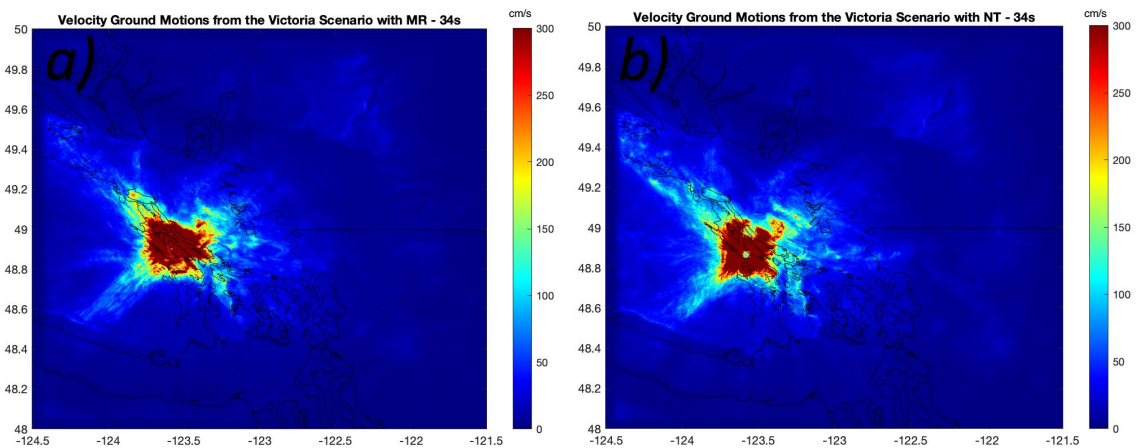


Figure 15: (a) Victoria rupture velocity amplitude map with topography at 34 seconds. (b) Victoria rupture velocity amplitude map without topography at 34 seconds.

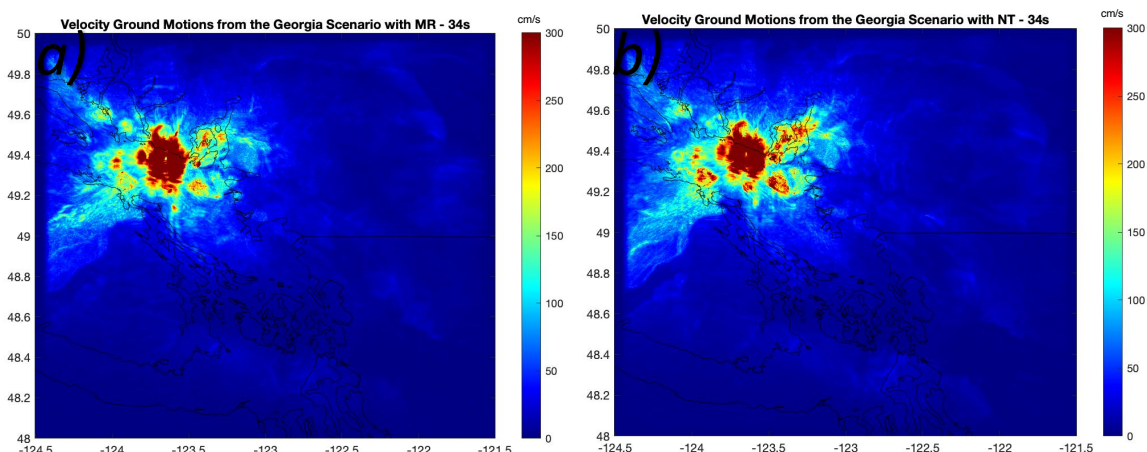


Figure 16: (a) Georgia Strait rupture velocity amplitude map with topography at 34 seconds. (b) Georgia Strait rupture velocity amplitude map without topography at 34 seconds.

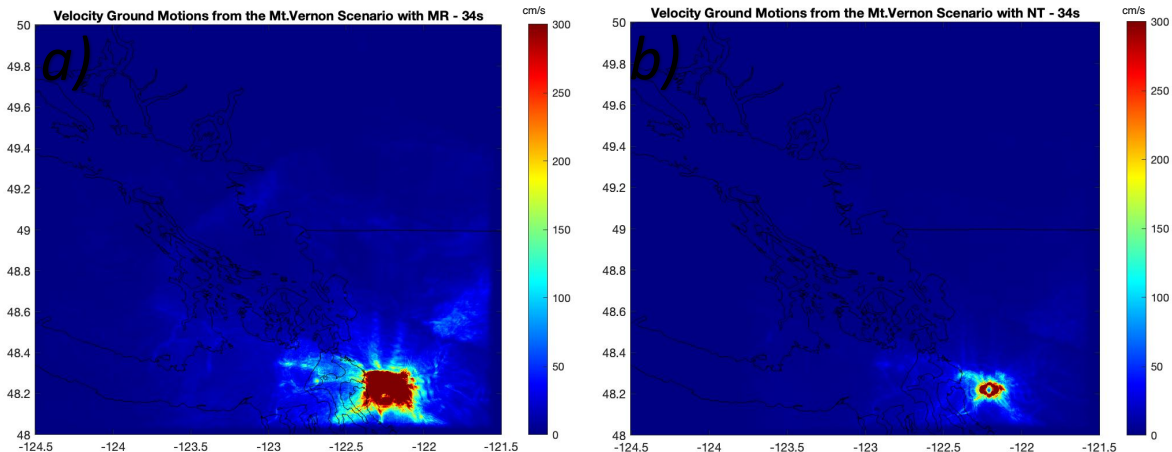


Figure 17: (a) Mt. Vernon rupture velocity amplitude map with topography at 34 seconds. (b) Mt. Vernon rupture velocity amplitude map without topography at 34 seconds.

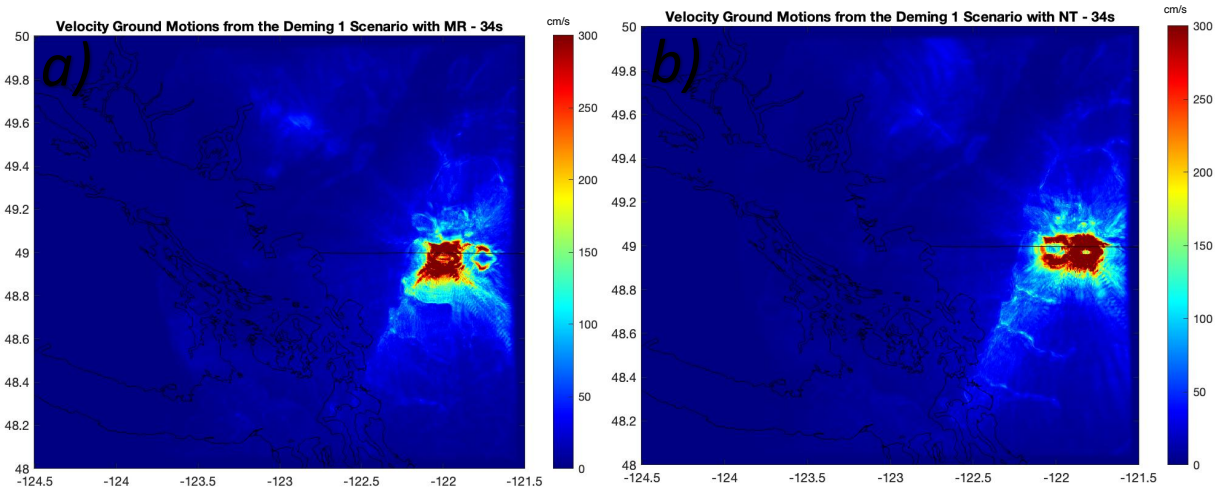


Figure 18: (a) Deming 1 rupture velocity amplitude map with topography at 34 seconds. (b) Deming 1 rupture velocity amplitude map without topography at 34 seconds.

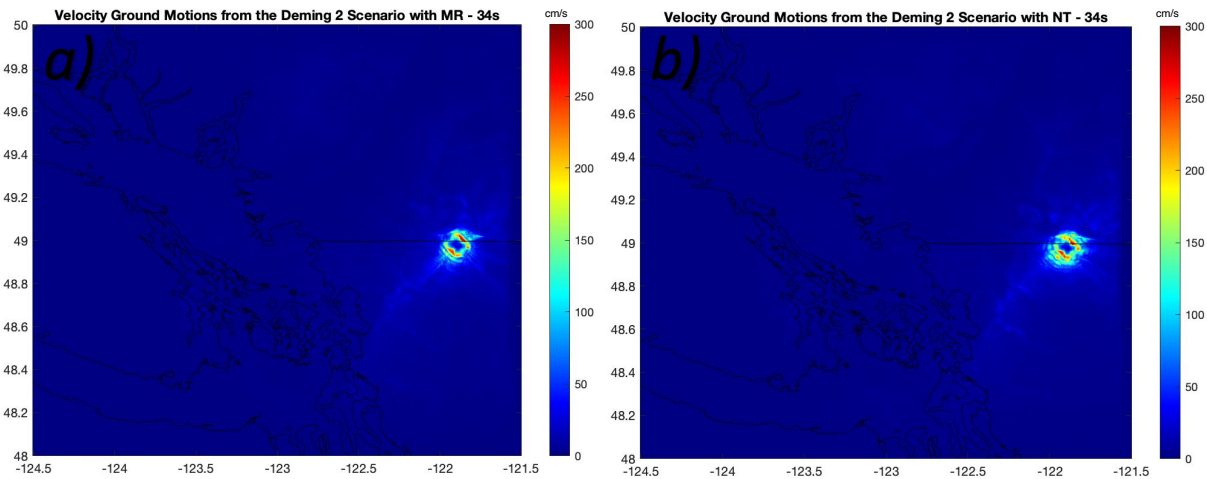


Figure 19: (a) Deming 2 rupture velocity amplitude map with topography at 34 seconds. (b) Deming 2 rupture velocity amplitude map without topography at 34 seconds.

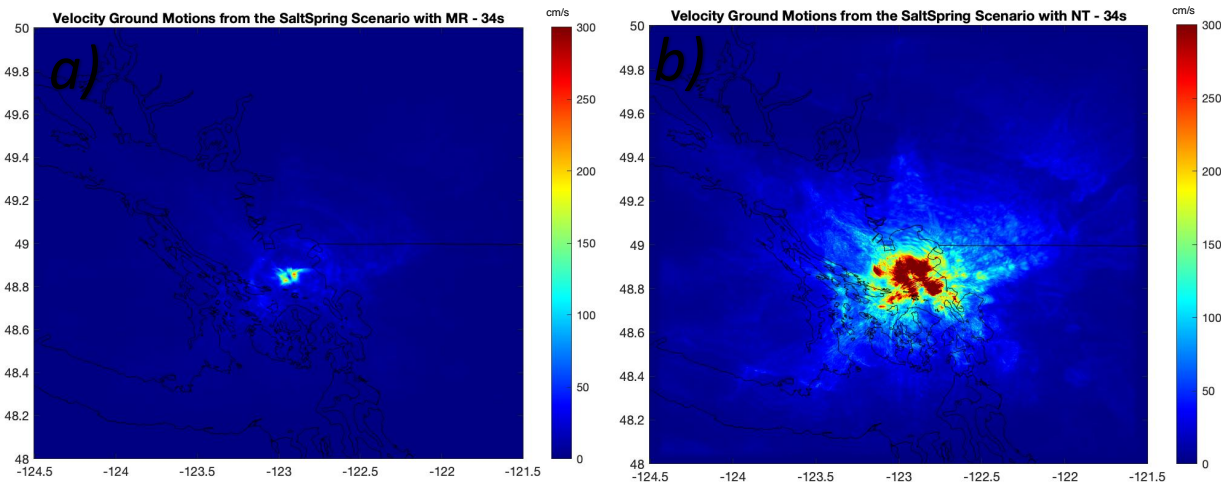


Figure 20: (a) Salt Spring Island rupture velocity amplitude map with topography at 34 seconds. (b) Salt Spring Island rupture velocity amplitude map without topography at 34 seconds.

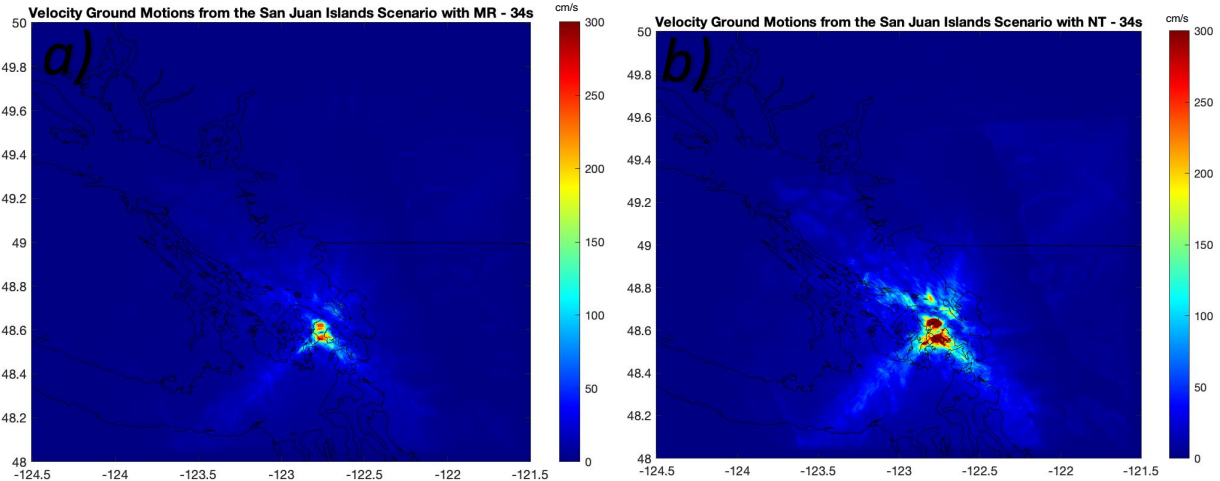


Figure 21: (a) San Juan Island rupture velocity amplitude map with topography at 34 seconds. (b) San Juan Island rupture velocity amplitude map without topography at 34 seconds.

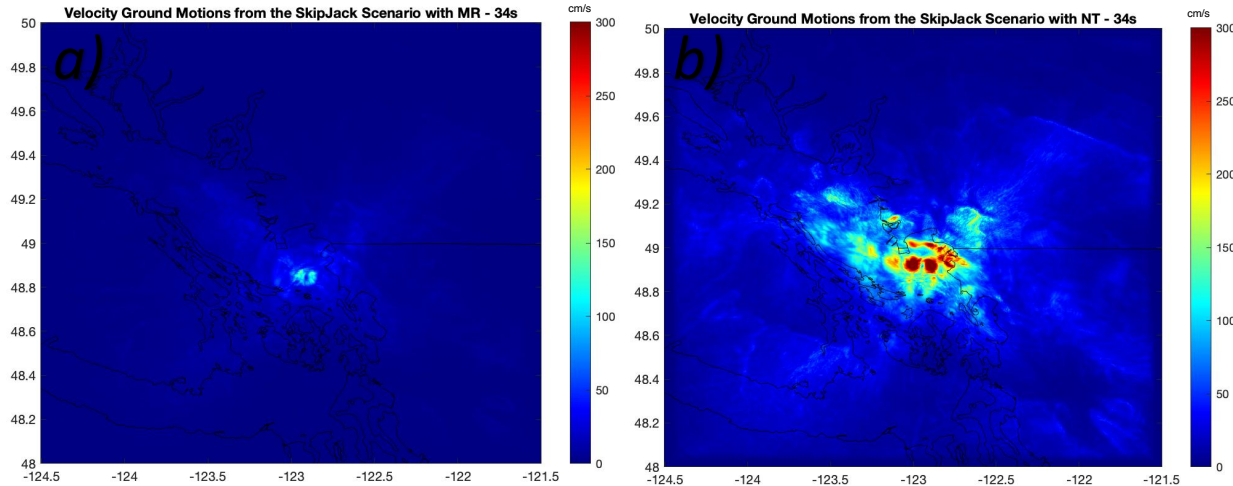


Figure 22: (a) Skip Jack rupture velocity amplitude map with topography at 34 seconds. (b) Skip Jack rupture velocity amplitude map without topography at 34 seconds.

4.3 PGV Geomean Relative Difference – 2 Hz Resolved Frequency

The PGV geometric mean was computed for 4 scenarios at 8 sites each, shown in Table 8. There were decreases in the PGV for simulations with 2 Hz resolved frequency simulations when compared to 0.5 Hz resolved frequency simulations at most sites. The PGV for 2 Hz simulations could have increased the topographic effects at each of the

sites, causing increases and decreases depending on the site's elevation. The higher frequencies also contributed to more complexity at the source and specific sites, causing some sites to experience significant decreases in PGV while other areas experienced increases. Further study is needed to further constrain the reason for the decrease in PGV at most sites for these scenarios.

Table 8: PGV Geomean in the horizontal directions, including topography with MR. The scenarios shown are the same as was computed without MR to directly compare and quantify the effect of higher frequencies had.

Site	Georgia	Mt. Vernon	Deming 1	Deming 2
Airport	31.5	3.20	3.33	1.28
Burnaby	12.23	3.59	6.36	1.56
Cypress Mountain	13.99	2.45	3.80	0.89
Delta	23.95	2.39	3.19	1.24
Downtown	15.17	3.85	5.12	1.37
Richmond	30.92	3.62	3.32	1.23
Mt. Seymour	5.24	3.21	5.62	1.10
UBC	9.59	1.76	2.29	0.69
West Vancouver	16.29	3.34	4.92	1.25

The relative percent difference between the PGV geomeans were computed for 4 scenarios at 8 sites each, shown in Table 9. The Georgia Strait scenario percent

difference shows that the MR simulations had much larger PGVs than the simulations without MR and topography, with notable increases at the mountainous sites of Mt. Cypress (+429%) and Mt. Seymour (+323%). These sites were by far the largest increases for this rupture scenario. This could be due to the increasing effects of topography at higher frequencies causing much greater amplification, while the topography simulations at lower frequencies may have caused some de-amplification for these same sites. The high seismic velocity soils have lower ground motions than lower velocity soils at Richmond or Delta would, and were not counteracted by the topographic effect, causing the site effects from the soils to dominate. This made the difference between the simulations much larger than at the other lower elevation sites, such as Delta (+52%) and Richmond (+131%).

In the Mt. Vernon scenario, there was a notable decrease at all sites located at low elevations and low velocity soils (Richmond, Delta, Airport), while the higher elevation, high seismic velocity sites increased. This same effect is present at the Deming 1 scenario, with large increases in the PGV at mountainous sites but comparatively smaller increases at non-mountainous sites. The Deming 2 scenario showed decreases in ground motions at the soft soil, low elevation sites of Delta, Richmond and at the Airport ranging from -15% to -32%, with small increases elsewhere and a large increase at Mt. Seymour of 203%. The large increase could have been present at the Mt. Seymour site as opposed to the other mountainous site, Mt. Cypress because the Deming 2 scenario is located almost directly south of Mt. Seymour and has waves travelling perpendicular to its axis of elongation, which could cause increased amplification. The North Cascade Mountain range is just east of Deming 2, Deming 1, and Mt. Vernon, and could have trapped and funneled the waves north, increasing the ground motions at Mt. Seymour at

higher frequencies because of its proximity to this mountain range. The scenarios to the west have much lower ground motions when compared to the scenarios to the S-SW, and further investigation may be needed to conclude why these scenarios also amplify shaking at topographic highs much more than topographic lows.

Table 9: Relative difference in the PGV geomean between topography including MR and topography without MR.

Site	Georgia	Mt. Vernon	Deming 1	Deming 2
Airport	220	-18	69	-32
Burnaby	132	-50	86	4.5
Cypress Mountain	429	82	341	19
Delta	52	-24	69	-15
Downtown	158	-47	89	3
Richmond	131	-11	69	-20
Mt. Seymour	323	81	305	203
UBC	191	-25	127	4
West Vancouver	69	-54	64	-9

4.4 Modified Mercalli Intensity Ratings – 2 Hz Resolved Frequency

MMI at a site is a measure of the perceived shaking found at that site and was calculated at important locations for the Georgia Strait scenario with topography and MR, shown in Table 10. The Georgia Strait scenario was chosen out of the 8 scenarios for

visualization as it is closest geographically to the GVA and appears to have less source specific ground motions generated, in contrast to others such as the Mt. Vernon scenario. Most sites are expected to have significant perceived shaking for this scenario, with most experiencing strong or very strong shaking with some light damage. The MMI are about 1 level larger at all sites when topography and MR were included when compared with the MMI without topography and without MR.

Table 10: MMI for the Georgia Strait at select sites shows moderate to strong shaking at most sites, with correspondingly light to moderate damage.

Site	Perceived Shaking with topography
Airport	VI (Very strong)
Burnaby	V (Strong)
Cypress Mountain	IV (Strong)
Delta	VI (Very strong)
Downtown	V (Strong)
Richmond	VI (Very strong)
Mt. Seymour	IV (Moderate)
UBC	IV (Moderate)
West Vancouver	VI (Strong)

4.5 Frequency Spectrum and HVSR

The Fourier transform of the acceleration time series can be used to determine the acceleration at each frequency, and which frequency had the largest contribution to ground motions. To compute the Fourier spectra, The velocity time series data are differentiated to get acceleration time series at each station. A Fourier Transform is then applied to this data to convert it from the time to the frequency domain. Fourier

frequency spectra for the Georgia Strait scenario at the Delta, Mt. Cypress, Airport, Downtown, Mt. Seymour, and Richmond stations with topography and MR are shown in Figure 23a, 23b, 23c, 23d, 23e, and 23f, respectively. In all scenarios, most of the seismic energy in the horizontal directions (N-S, E-W) is arriving at higher frequencies, specifically from 1-2 Hz. The vertical direction has a higher proportion of seismic waves arriving below 1 Hz than the horizontal directions, but still has most seismic waves arriving at 1-2 Hz. This agrees with the PGV geomean calculations for simulations, which had 50-400% greater PGV values when MR and topography are included in simulations, compared to no MR and no topography included.

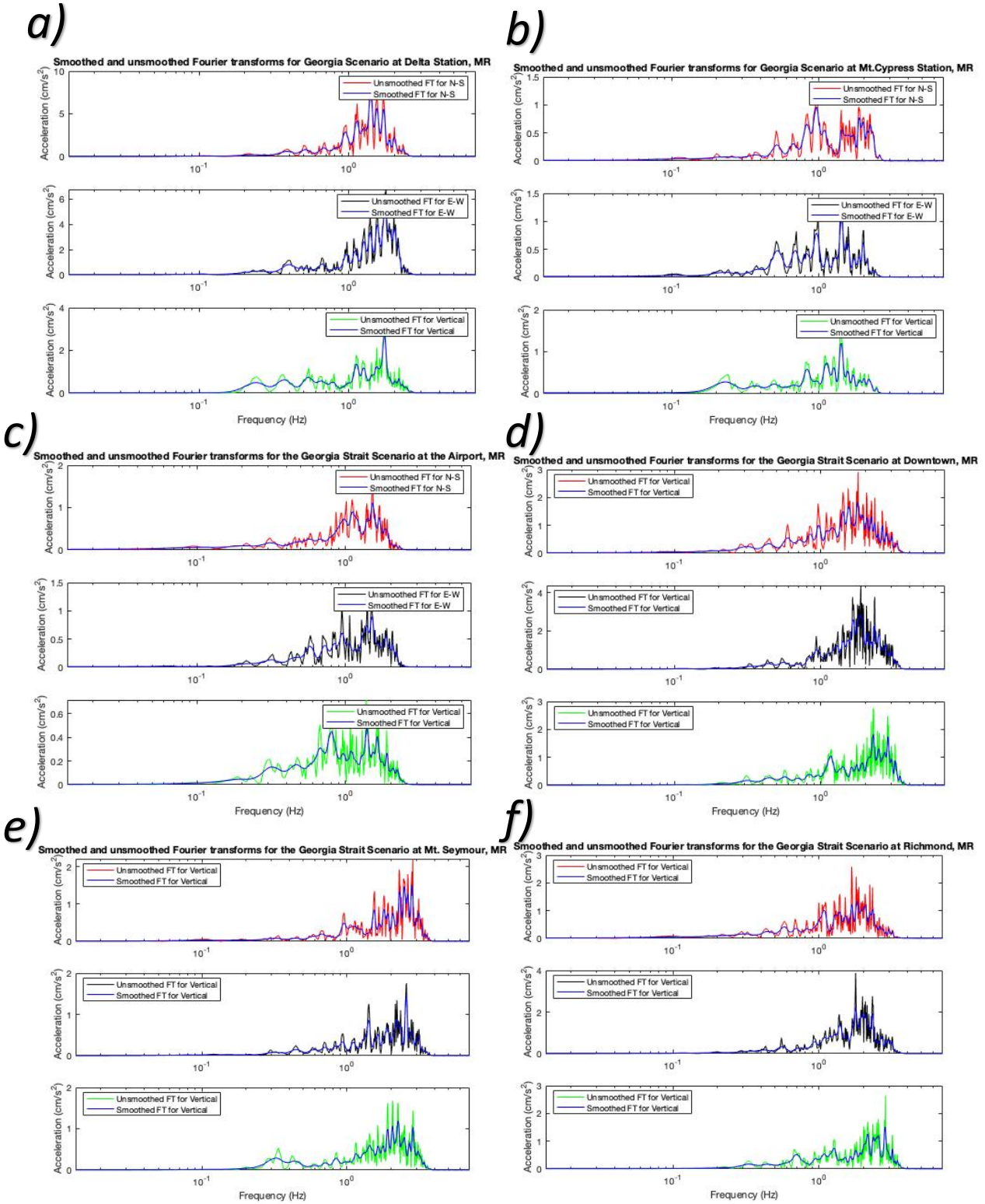


Figure 23: Fourier frequency spectrum for the Georgia scenario at the **(a)** Delta, **(b)** Mt. Cypress, **(c)** Airport, **(d)** Downtown, **(e)** Mt. Seymour, and **(f)** Richmond stations with topography and MR. The E-W, N-S and vertical directions are shown.

The geometric mean of the Fourier transforms was then taken of the horizontal components and divided by the Fourier transform of the vertical components to generate the HVSR. The HVSR is an estimate of the resonant frequency of the subsurface and any amplification of the seismic waves at a range of frequencies due to the soils. The simulations with topography and without MR, and without topography and without MR show frequency content above 0.5 Hz because there are still small amounts of high frequency waves above 0.5 Hz that cannot be removed due to the cut-off frequency not blocking all frequencies above 0.5 Hz, but a gradual slope to eliminating them. The Georgia Strait scenario is displayed since it was geographically the closest earthquake source to the recording stations. At the Delta station, shown in Figure 24a, the inclusion of topography with resolved frequencies up to 2 Hz caused an increase in the amplification compared to simulations without topography. There is a strong basin effect at this site, since it sits atop the Georgia basin, and the increase in amplification could also be caused by the basin effect. The HVSR was also calculated at the Mt. Cypress site, shown in Figure 24b, since this site appeared to have significant amplification in the higher frequency simulations for multiple scenarios. At low frequencies (≥ 0.2 Hz) there is greater amplification in simulations with no topography (green). At these lower frequencies, simulations with topography showed significant de-amplification relative to the simulation without topography. Simulations with topography at the mountainous regions had much lower ground motions relative to the simulations without topography for this reason, as the topographic effect de-amplified the ground motions at these lower frequencies. As the frequency increased, the amplification for

the MR simulation increased until the amplification was larger than in the other simulations.

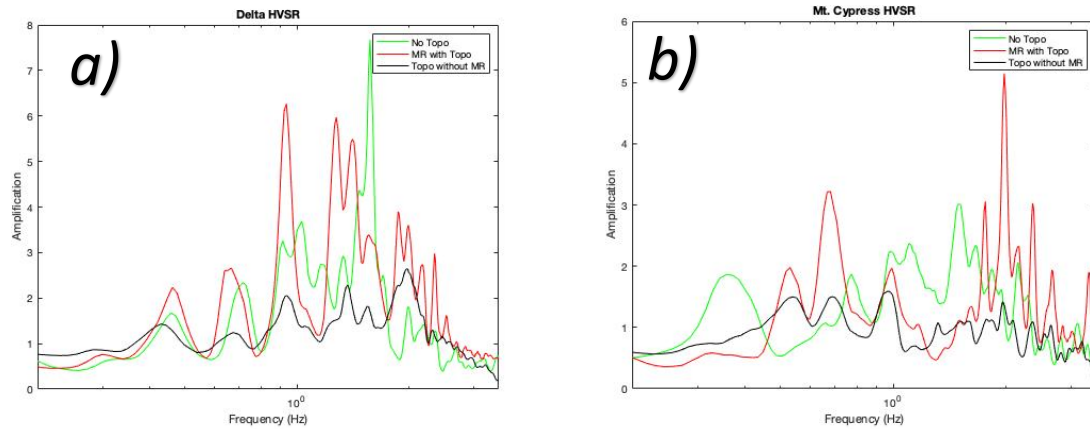


Figure 24: a) HVSR for Delta, with and without topography for the Georgia Strait scenario. Increases in amplification are apparent with topography and MR at most frequencies, although there is more variability. b) HVSR for Mt. Cypress, with and without topography for the Georgia Strait scenario. Frequencies from 1.5 Hz to 2 Hz show large amplification with topography and MR.

4.6 Traverse Up Mt. Cypress

West Vancouver and Mt. Cypress displayed strong topographic effects in most of the computed rupture scenarios and are geographically close aside from the increased elevation at the peak of Mt. Cypress. Mt. Cypress also has its axis of elongation towards the south, which is where all scenarios are located. This makes it a good candidate to study the effect increasing topography has on ground motions, as we are not moving significantly farther from the source, which could decrease the ground motions, and have seismic waves travelling directly to the mountain from sea level very nearby, providing a good reference point to the higher topographies. To study this region further, simulations were run with and without topography to record the ground motions along West

Vancouver moving up Mt. Cypress. It is expected that ground motions at the top of the mountain will display higher velocity amplitudes than the ground motions at the base of the mountain. Point 1 is a point at the base of Mt. Cypress while Point 5 is near the peak of Mt. Cypress. As we move up the mountain and gain elevation, the geomean of the PGV max increases, with simulations without topography having a small increase from Point 1 to Point 5 while simulations with topography up to 0.5 Hz have greater increases at the higher elevations and lower PGV at the base. Simulations with MR have larger PGV at higher elevations and smaller PGV max at lower elevations, showing that the increased elevation caused amplification of seismic waves in the horizontal direction and including higher frequencies further increased the amplification. While Point 1 had the highest ground motions at 15.8 cm/s in the topography simulation with MR, the points at higher elevations had the greatest increase in PGV from incorporating higher frequencies, with increases of 598% from simulations with topography and no MR, compared to an increase of 249% for Point 1. This shows topography has greater effects on ground motions at higher elevations, but only at higher frequencies.

Table 11: PGV max of traverse up Mt. Cypress in E-W direction using Georgia Strait Scenario. Simulations with topography show a greater increase in PGV with increasing elevation over the simulations without topography. The simulations with MR showed even greater increases in PGV due to increasing elevation.

Site	PGV, No Topography (cm/s)	PGV, Topography (cm/s)	PGV, Topography with MR (cm/s)	Latitude	Longitude	Elevation (m)
Point 1	6.99	6.34	15.8	49.27292	-123.1564	45
Point 2	9.36	3.74	8.78	49.22351	-123.1646	122
Point 3	9.14	3.16	13.41	49.35601	-123.1646	423
Point 4	10.8	2.64	13.99	49.37173	-123.1814	964
Point 5	9.7	2.28	13.65	49.35601	-123.1856	1010

Chapter 5 - Discussion and Conclusions

To quantify the effect topography and higher frequency seismic waves have on ground motions throughout the GVA from large, shallow crustal earthquakes, the numerical 3D FD scheme of SW4 was employed to simulate the slip distribution of the M6.7 Northridge earthquake within 100 km of the GVA at a suite of probable locations (Molnar 2014b). 8 different scenarios were simulated with and without topography included in the physical structure model, with a maximum resolvable frequency of 0.5 Hz in accordance with stability parameters of 4th order FD schemes, then at a maximum frequency of 2 Hz when two MR layers were added to the model with topography. MR allowed for further discretization of the velocity model to increase the maximum resolvable frequency. The 8 scenario locations were chosen based on active faults and historical seismicity in the region (Molnar et al., 2014b). The synthetic motions (velocity time series,

PGV) without topography and without MR were compared to synthetic motions with topography and with MR to quantify the topographic effects in the simulations.

In general, amplitudes of seismic waves were variable between different rupture scenarios, and the rupture location and source parameters had significant effects on the ground motions, with S-SW located sources such as the Georgia Strait, Victoria, and Salt Spring Island scenarios generating the largest amplitude ground motions, as shown in Molnar et al. (2014b). The Deming 1 and Deming 2 scenarios, which are located E-SE of the GVA had very different ground motion amplitudes at the recording stations and at the epicentre location, with mainly just the strike and dip varied between the two simulations. The Mt. Vernon and Georgia Strait scenarios showed this same effect, with an over 1000% difference in PGV due to different rupture locations, azimuth, and topography at the rupture location. Most scenarios showed amplification when topography and higher frequencies were included, aside from the Skipjack Island and Salt Spring Island scenarios, which had mostly de-amplification at the chosen recording stations. Seismic stations at mountainous locations showed the most amplification when higher frequencies (0.5-2 Hz) were resolved, with Mt. Seymour having amplification of 40% or greater in 6 of 8 scenarios. These same stations had significantly smaller ground motions when just low frequency ground motions were included (≤ 0.5 Hz), showing topographic de-amplification at the lower frequencies around 0.5 Hz and significant topographic amplification from 0.5-2 Hz. This could be because mountainous sites with higher model velocities (V_p, V_s) have lower amplification and even de-amplification due to high model velocities, and the effect of topographic resonance, which occurs mostly at higher frequencies and increases ground motions, cannot counteract the effect of de-amplification and the decrease in

ground motions from the high model velocities at low frequencies as a result. This caused these mountainous sites to have very low PGV values in the 0.5 Hz simulations, but dramatic increases in PGV in the 2 Hz simulations. This contrasts with the lower elevation sites such as Delta and Richmond, which showed potential amplification at very low frequencies (<0.5 Hz) but received much less amplification as the frequency in the simulations increased. The effect of soft soils and the basin effect from the Georgia basin at these sites could have dominated at lower frequencies, providing significant amplification, but had a more minimal effect at higher frequencies, as high frequency seismic waves do not contribute to these amplification factors as much as lower frequency waves do. The topography may even have a de-amplifying effect on these and similar locations. These combined effects caused the rate of increase in ground motions with increasing frequency to be lower at the basin and soft soils sites. The hard soil, mountainous sites that do not have amplification due to the soil and basin may have had de-amplification from these factors and less competing effects from the hard soil and so showed a greater increase in ground motions with just the topographic effect contributing. The MMI is a measure of the perceived shaking felt during an earthquake and was computed for the WPS with topography and MR, without topography and MR, and with topography and without MR. It was found that the MMI increased by one level at most sites when the maximum resolvable frequency was 2 Hz. This indicates that the perceived shaking increased with increasing frequency content in the simulations but may be due to additional energy present in the higher frequency simulations (≤ 2 Hz) that was filtered out in the lower frequency simulations (≤ 0.5 Hz).

5.1 Thesis Contributions

The major scientific contributions from this thesis include the successful implementation of surface topography into 3D WPS for southwest B.C, as the previous WPS did not include topography. The maximum resolvable frequency was also advanced from 0.5 Hz previously, to a maximum of 2 Hz in simulations including MR. The effect of topography on mountainous, high velocity sites and low elevation, low velocity sites were quantified by calculating the relative percent difference between the WPS with topography and MR, and without topography and MR. The effect of varying azimuth angle and rupture location on topography was determined, with scenarios S-SW the GVA having the largest ground motions, but the E-SE scenarios (Mt. Vernon, Deming 1 and 2) having much larger ground motions with topography than without, particularly when MR was included.

5.2 Future Work

Future study in the region should include further analysis on the effect of increasing frequencies on ground motions in the region by pushing the maximum resolvable frequency as high as possible, ideally up to 10 Hz, to determine whether the trend of higher rate of increase at mountainous sites than soft soil sites hold throughout the frequency spectrum to 10 Hz and potentially accelerates. Different earthquake rupture scenarios should also be explored, with the effects of topography from an earthquake occurring within the subducting Juan de Fuca plate, and megathrust earthquakes along the Cascadia Subduction Zone modelled.

References

- Adams, J. S., Halchuk, T., Allen, G., Rogers. (2015). Canada's 5th generation seismic hazard model, as prepared for the 2015 National Building Code of Canada. 11th Canadian Conference on Earthquake Engineering, Victoria, Canada, Paper 93775.
- Assaf, J., Molnar, S., El Naggar, H., & Sirohey, A. (2022). Seismic site characterization in Fraser River delta in Metropolitan Vancouver. *Soil Dynamics and Earthquake Engineering*, 161, 107384. <https://doi.org/10.1016/j.soildyn.2022.107384>.
- Atwater, B.F., Musumi-Rokkaku, S., Satake, K., Tsuji, Y., Ueda, K., & Yamaguchi, D.K. (2015). The orphan tsunami of 1700—Japanese clues to a parent earthquake in North America, 2nd ed. Seattle, University of Washington Press, U.S. Geological Survey Professional Paper 1707, 135 p.
- Balfour, N. J., Cassidy, J. F., Dosso, S. E., & Mazzotti, S. (2011). Mapping crustal stress and strain in southwest British Columbia. *Journal of Geophysics Research*. 116. doi:10.1029/2010JB008003.
- Bard, P., & Bouchon, M. (1980). The seismic response of sediment-filled valleys. Part 2. The case of incident *P* and *SV* waves. *Bulletin of the Seismological Society of America*, 70(5), 1921–1941. doi: <https://doi.org/10.1785/BSSA0700051921>.
- Boore, D. (1972). A note on the effect of simple topography on seismic *SH* waves. *Bulletin of the Seismological Society of America*, 62(1), 275-284.
- Bouchon, M., Schultz, C. A., & Toksöz, M. N. (1996). Effect of three-dimensional topography on seismic motion, *Journal of Geophysics Research*, 101(B3), 5835– 5846. doi:10.1029/95JB02629.
- Cassidy, J. F., & Waldhauser, F. (2003). Evidence for both crustal and mantle earthquakes in the subducting Juan de Fuca plate, *Geophysics Research Letters*, 30, 1095. doi:10.1029/2002GL015511.
- Cassidy, J. F., Rogers, G. C., Lamontagne, M., Halchuk, S., & Adams, J. (2010). Canada's Earthquakes: 'The Good, the Bad, and the Ugly'. *Geoscience Canada*, 37(1).
- Çelebi, M. (1987). Topographical and geological amplifications determined from strong-motion and aftershock records of the 3 March 1985 Chile earthquake. *Bulletin of the Seismological Society of America*, 77(4), 1147–1167. doi: <https://doi.org/10.1785/BSSA0770041147>.
- Clague, J. J. (1997). Evidence for large earthquakes at the Cascadia Subduction Zone. *Review of Geophysics*, 35(4), 439– 460.

Danielson, J.J., & Gesch, D.B. (2011). Global multi-resolution terrain elevation data 2010 (GMTED2010): U.S. Geological Survey Open-File Report 2011-1073, 26 p.

Frankel, A., Stephenson, W., Carver, D., Williams, R., Odom, J., & Rhea, S. (2007). Seismic hazard maps for Seattle incorporating 3D sedimentary basin effects, nonlinear site response, and rupture directivity, U.S. Geological Survey Open-File Rept. 2007-1175

Frankel, A., Wirth, E., Marafi, N., Vidale, J., & Stephenson, W. (2018). Broadband Synthetic Seismograms for Magnitude 9 Earthquakes on the Cascadia Megathrust Based on 3D Simulations and Stochastic Synthetics, Part 1: Methodology and Overall Results. *Bulletin of the Seismological Society of America*, 108, 2347–2369.
doi: 10.1785/0120180034.

Geli, L., Bard, P., & Jullien, B. (1988). The effect of topography on earthquake ground motion: A review and new results. *Bulletin of the Seismological Society of America*, 78 (1), 42–63. doi: <https://doi.org/10.1785/BSSA0780010042>.

Ghofrani, H., & Molnar, S. (2019). 3D Sedimentary Basin Effects in the Metro Vancouver Area and Its Seismic Hazard Implications: Updates and Validations of the Georgia Basin Velocity Model. *12th Canadian conference on earthquake engineering*.

Goldfinger, C., Nelson, C.H., Morey, A.E., Johnson, J.E., Patton, J.R., Karabarov, E., Gutiérrez-Pastor, J., Eriksson, A.T., Gràcia, E., Dunhill, G., Enkin, R.J., Dallimore, A., & Vallier, T. (2012). Turbidite event history—Methods and implications for Holocene paleoseismicity of the Cascadia subduction zone: U.S. Geological Survey Professional Paper, 1661-F, 170 p.

Graves, R. W., Pitarka, A., & Somerville, P. (1998). Ground-motion amplification in the Santa Monica area: Effects of shallow basin-edge structure. *Bulletin of the Seismological Society of America*, 88(5), 1224–1242. doi: <https://doi.org/10.1785/BSSA0880051224>.

Gripp, A. E., & Gordon, R. G. (2002). Young tracks of hotspots and current plate velocities, *Geophysical Journal International*, 150, 321-361.

Hartzell, S., Meremonte, M., Ramírez-Guzmán, L., & McNamara, D. (2014). Ground Motion in the Presence of Complex Topography: Earthquake and Ambient Noise Sources. *Bulletin of the Seismological Society of America*, 104(1).
doi: 10.1785/0120130088.

Hirano, S. (2022). Source time functions of earthquakes based on a stochastic differential equation. *Scientific Reports*, 12, 3936. <https://doi.org/10.1038/s41598-022-07873-2>

Hough, S. E., Altidor, J. R., Anglade, D., Given, D., Janvier, M. G., Maharrey, J. Z., Meremonte, M., Mildor, B. S.-L., Prepetit, C., & Yong, A. (2010). Localized damage caused by topographic amplification during the 2010 M 7.0 Haiti earthquake, *Natural Geoscience*, 3, 778–782.

Khan, S., Meijde, M., Werff, H., & Shafique, M. (2020). The impact of topography on seismic amplification during the 2005 Kashmir earthquake. *Natural Hazards and Earth System Science*, 20, 399–411. <https://doi.org/10.5194/nhess-20-399-2020>.

Lee, S.J., Chan, Y.C., Komatitsch, D., & Tromp, J. (2009). Effects of realistic surface topography on seismic ground motion in the Yangmingshan region (Taiwan) based upon the Spectral-Element method and LiDAR DTM. *Bulletin of the Seismological Society of America*, In press

Lee, S., Komatitsch, D., Huang, B., & Tromp, J. (2009). Effects of Topography on Seismic-Wave Propagation: An Example from Northern Taiwan. *Bulletin of the Seismological Society of America*, 99. doi: 10.1785/0120080020.

Lee, S.J., Chan, Y.C., Komatitsch, D., & Tromp, J. (2008). Three-dimensional simulation of seismic wave propagation in the Taipei basin with realistic topography based upon the spectral-element method. *Bulletin of the Seismological Society of America*, 98, 253-264.

Leonard, L., Currie, C., Mazzotti, S., & Hyndman, R. D. (2010). Rupture area and displacement of past Cascadia great earthquakes from coastal coseismic subsidence. *GSA Bulletin*, 122(11), 1951–1968. doi: 10.1130/B30108.1.

Levander, A. R. (1989). Finite-difference forward modelling in seismology. *Geophysics. Encyclopedia of Earth Science*. Springer, Boston, MA.

Lovati, S., Bakavoli, M., Massa, M., Pacor, F., & Paolucci, R. (2010). An Experimental Approach for Estimating Seismic Amplification Effects at the Top of a Ridge, and the Implication for Ground-Motion Predictions: The Case of Narni, Central Italy. *Bulletin of the Seismological Society of America*, 100, 4955.

Massa, M., Lovati, S., D'Alema, E., Ferretti, G., & Bakavoli, M. (2010). An experimental approach for estimating seismic amplification effects at the top of a ridge, and the implication for ground-motion predictions: The case of Narni, Central Italy. *Bulletin of the Seismological Society of America*, 100, 3020–3034.

Moczo, P., Kristek, J., & Halada, L. (2000). 3D Fourth-Order Staggered-Grid Finite-Difference Schemes: Stability and Grid Dispersion. *Bulletin of the Seismological Society of America*, 90(3), 587–603. doi: <https://doi.org/10.1785/0119990119>.

Ma, S. J., Archuleta, R. J., & Page, M. T. (2007). Effects of large-scale surface topography on ground motions, as demonstrated by a study of the San Gabriel Mountains, Los Angeles, California. *Bulletin of the Seismological Society of America*, 97, 2066–2079.

Molnar, S. (2011). Predicting earthquake ground shaking due to 1D soil layering and 3D basin structure in SW British Columbia, Canada, *Ph.D. Thesis*, University of Victoria, Victoria, British Columbia, 150 pp.

Molnar, S., Cassidy, J.F., Dosso, S.E., & Olsen, K.B. (2008). Seismic hazard investigations of southwestern British Columbia, Canada, 14th World Conference on Earthquake Engineering, Beijing, China, Poster 214.

Molnar, S., Cassidy, J.F., Olsen, K.B., Dosso, S.E., & He. J. (2014a). Earthquake ground motion and 3D Georgia Basin amplification in southwest British Columbia: Deep Juan de Fuca plate scenario earthquakes, *Bulletin of the Seismological Society of America*, 104, 301-320. doi: 10.1785/0120110277.

Molnar, S., Cassidy, J.F., Olsen, K.B., Dosso, S.E., & He. J. (2014b). Earthquake ground motion and 3D Georgia Basin amplification in southwest British Columbia: Shallow blind-thrust scenario earthquakes. *Bulletin of the Seismological Society of America*. 104, 321-335. doi: 10.1785/0120130116.

Molnar, S. (2003). Investigating seismic hazard and site response in Victoria, BC; Analysis of felt reports and ground motion recordings from the 2001 Nisqually earthquake. *MSC Thesis*, University of Victoria.

Morell, K., Regalla, C., Amos, S., Bennett, L., Leonard, A., Graham, T., Reedy, V., & Levson, A. (2018). Holocene surface rupture history of an active forearc fault redefines seismic hazard in southwestern British Columbia, Canada. *Geophysical Research Letters*, 45, 11,605- 11,611. doi: 10.1029/2018gl078711.

Morell, K., Regalla, L., & Leonard, C. (2017). Quaternary rupture of a crustal fault beneath Victoria, British Columbia, Canada. *GSA Today*, 27, 1-7. doi: 10.1130/GSATG291A.1.

Munich Reinsurance Company of Canada. (1992). *Earthquake: Economic Impact Study*. Toronto, Ontario, 99.

OpenDEM. "Arc2Meters Converter", *OpenDEM*,
<https://www.opendem.info/arc2meters.html>

Petersson, N. A., & Sjogreen, B. (2012). Stable and efficient modeling of anelastic attenuation in seismic wave propagation. *Communications in Computational Physics*, 12 (1), 193-225.

Petersson, N. A., & Sjogreen, B. (2017). User's guide to SW4, version 2.0. Technical report. LLNL-SM-741439, Lawrence Livermore National Laboratory, Livermore, CA.

Pitarka, A., Akinci, A., De Gori, P., & Buttinelli, M. (2021). Deterministic 3D Ground-Motion Simulations (0–5 Hz) and Surface Topography Effects of the 30 October 2016 Mw 6.5

Norcia, Italy, Earthquake. *Bulletin of the Seismological Society of America*, 112(1), 262–286. doi: <https://doi.org/10.1785/0120210133>.

Pitarka, A., Graves, R., & Somerville, P. (2004). Validation of a 3D velocity model of the Puget Sound region based on modeling ground motion from the 28 February 2001 Nisqually earthquake. *Bulletin of the Seismological Society of America*, 94: 1670–1689.

Reiter, L. (1999). Earthquake Hazard Analysis (Columbia University Press, New York), 254.

Restrepo, D., Bielak, J., Serrano, R., Gómez, J., & Jaramillo, J. (2016). Effects of realistic topography on the ground motion of the Colombian Andes – A case study at the Aburrá Valley, Antioquia, *Geophysical Journal International*, 204(3), 1801 -1816.
<https://doi.org/10.1093/gji/ggv556>.

Rodgers, A. J., Pitarka, A., Pankajakshan, R., Sjögren, B., & Petersson, N. (2020). Regional-Scale 3D Ground-Motion Simulations of Mw 7 Earthquakes on the Hayward Fault, Northern California Resolving Frequencies 0–10 Hz and Including Site-Response Corrections. *Bulletin of the Seismological Society of America*, 110(6), 2862-2881.

Roten, D., Olsen, K. B., & Takedatsu, R. (2020). Numerical Simulation of M9 Megathrust Earthquakes in the Cascadia Subduction Zone. *Pure and Applied Geophysics*, 177(5), 2125-2141.

Roullé, A., & Chávez-García, F. J. (2006). The strong ground motion in Mexico City: Analysis of data recorded by a 3D array, *Soil Dynamics and Earthquake Engineering*, 26, 71–89.

Sánchez-Sesma, F. J., & Campillo, M. (1993). Topographic effects for incident P, SV and Rayleigh waves. *Tectonophysics*, 218(1–3), 113-125.
[https://doi.org/10.1016/0040-1951\(93\)90263-J](https://doi.org/10.1016/0040-1951(93)90263-J).

Singh, S. K., Mena. E., & Castro R. (1988). Some aspects of the source characteristics and ground motion amplifications in and near Mexico City from acceleration data of the September 1985, Michoacan, Mexico earthquakes, *Bulletin of the Seismological Society of America*, 78, 451–477.

Song, S., G. (2016). Developing a generalized pseudo-dynamic source model of M_w 6.5–7.0 to simulate strong ground motions, *Geophysical Journal International*, 204, 1254–1265. <https://doi.org/10.1093/gji/ggv521>.

Stephenson, W. (2007). Velocity and density models incorporating the Cascadia Subduction Zone for 3D earthquake ground motion simulations, USGS Open File 1348.

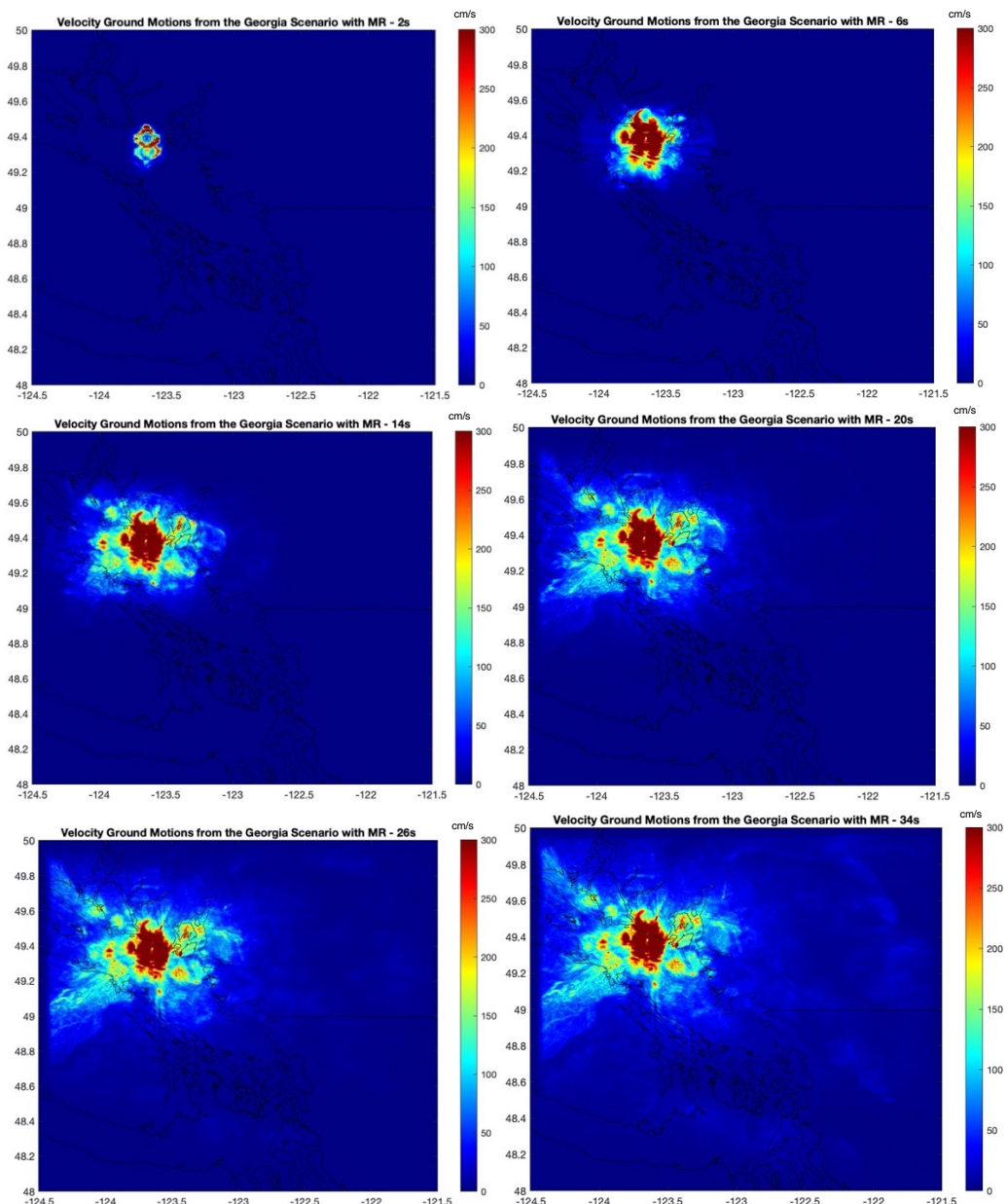
Stone, I., Wirth, E.A., & Frankel, A. (2022). Topographic Response to Simulated Mw 6.5–7.0 Earthquakes on the Seattle Fault. *Bulletin of the Seismological Society of America*, 112(3), 1436–1462. doi: <https://doi.org/10.1785/0120210269>.

Wang, Z. (2011). Seismic hazard assessment: Issues and alternatives. *Pure and Applied Geophysics*, 168, 11-25. doi: 10.1007/s00024-010-0148-3.

Wang S., & Petersson, N. A. (2019). Fourth order finite difference methods for the wave equation with mesh refinement interfaces. *Journal of Scientific Computing*, 41, 5.

Wirth, E. A., Vidale, J. E., Frankel, A. D., Pratt, T. L., Marafi, N. A., Thompson, M., & Stephenson, W. J. (2019). Source-dependent amplification of earthquake ground motions in deep sedimentary basins. *Geophysical Research Letters*, 46, 6443– 6450.

Appendix



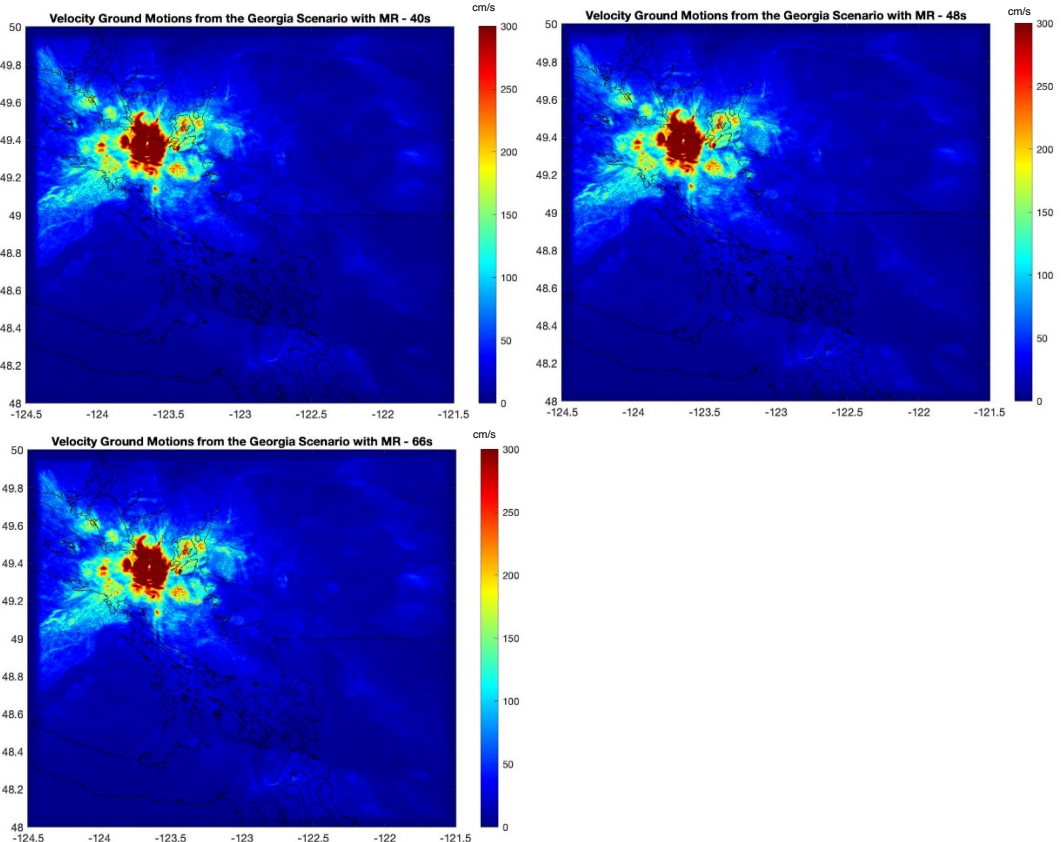
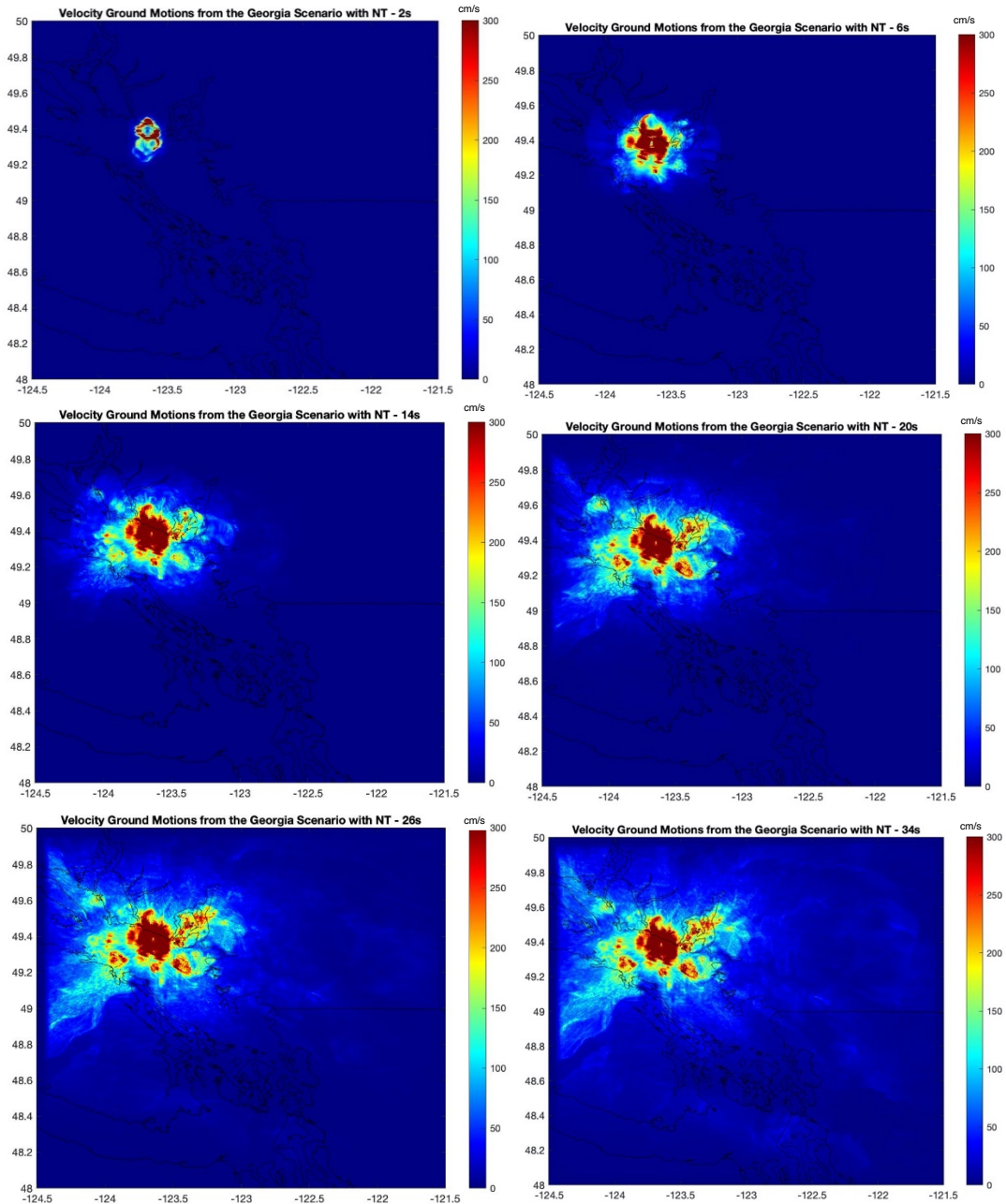


Figure 25: Velocity amplitude maps for the Georgia scenario with MR from 2-66 seconds of simulation duration.



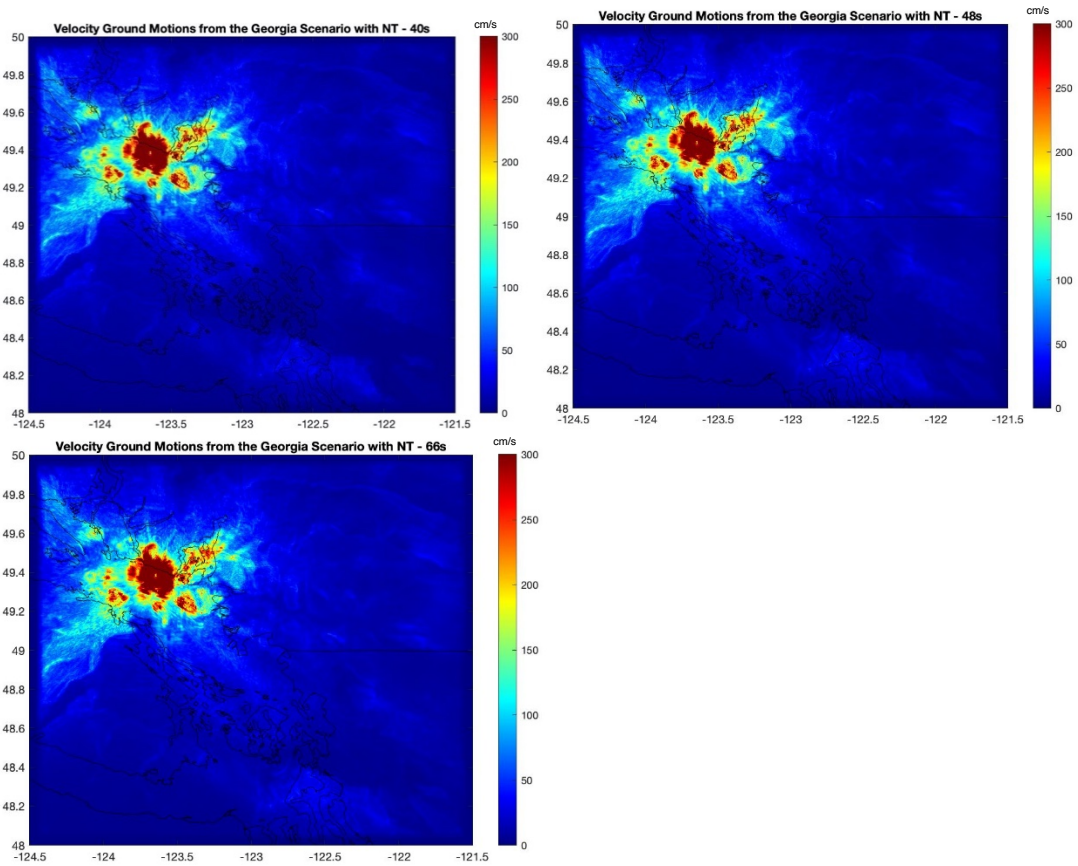
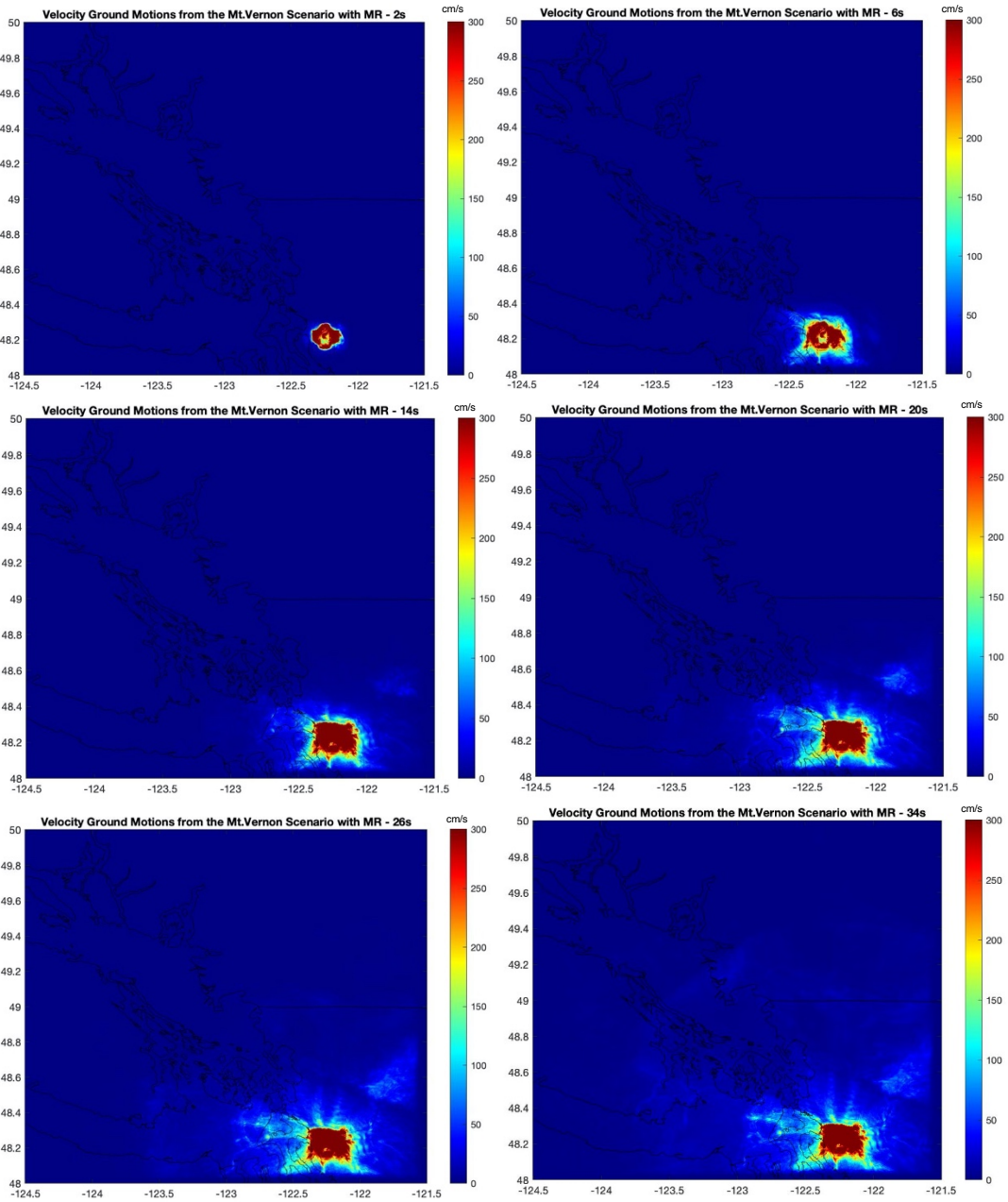


Figure 26: Velocity amplitude maps for the Georgia scenario without topography and MR from 2-66 seconds of simulation duration.



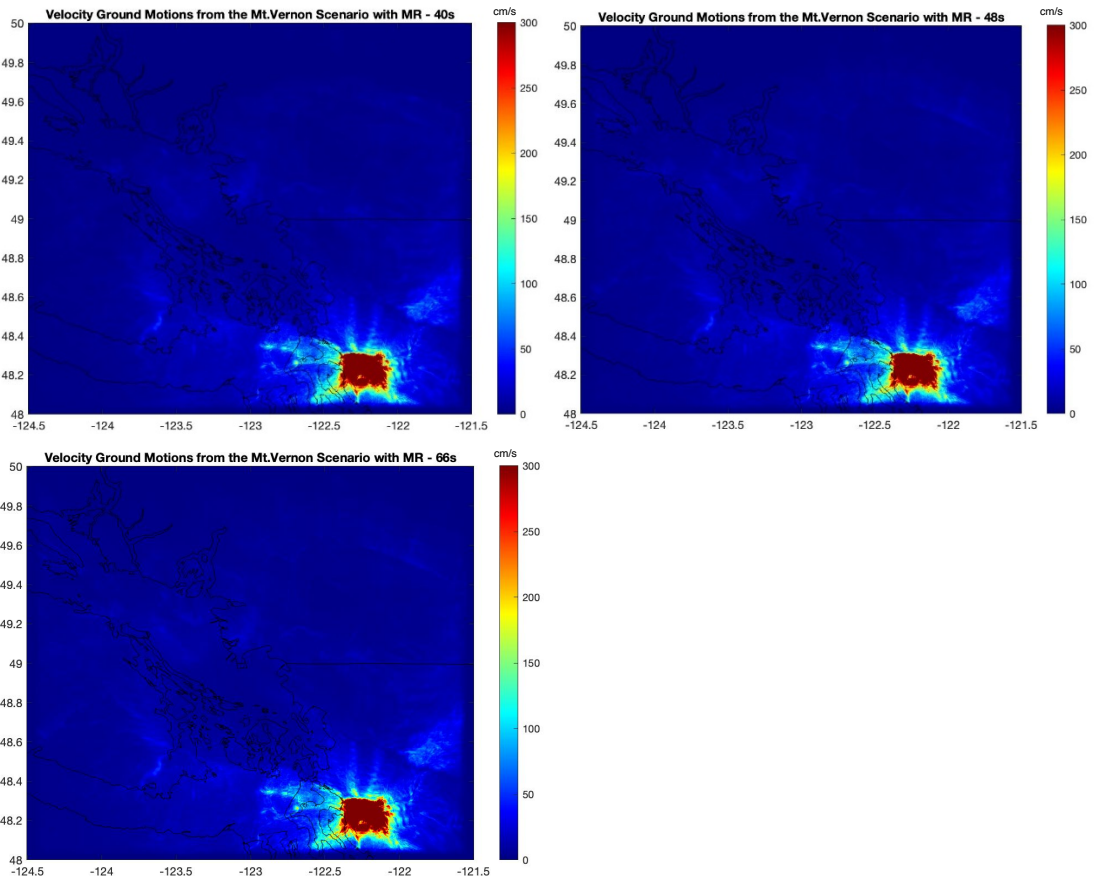
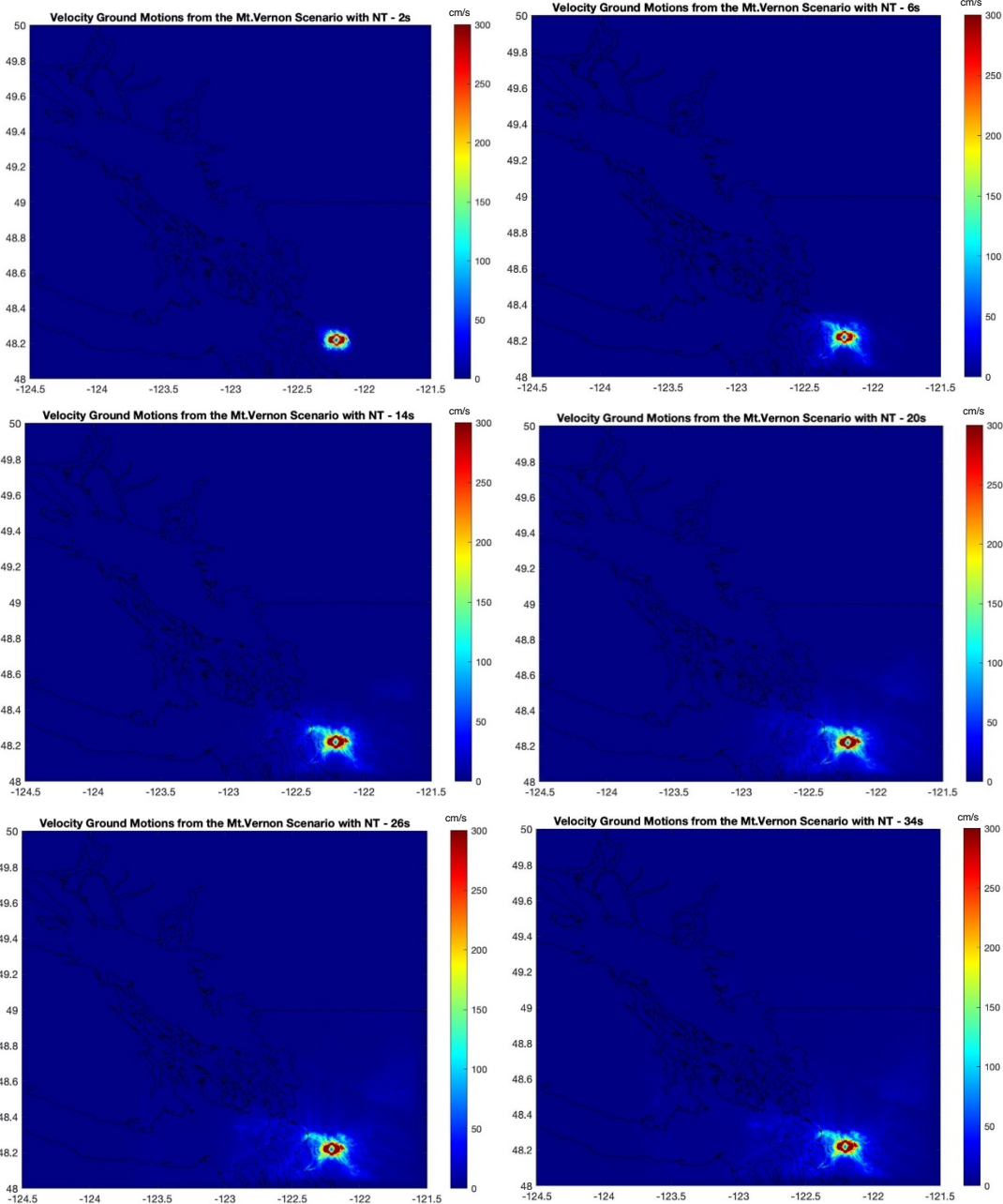


Figure 27: Velocity amplitude maps for the Mt. Vernon scenario with MR from 2-66 seconds of simulation duration.



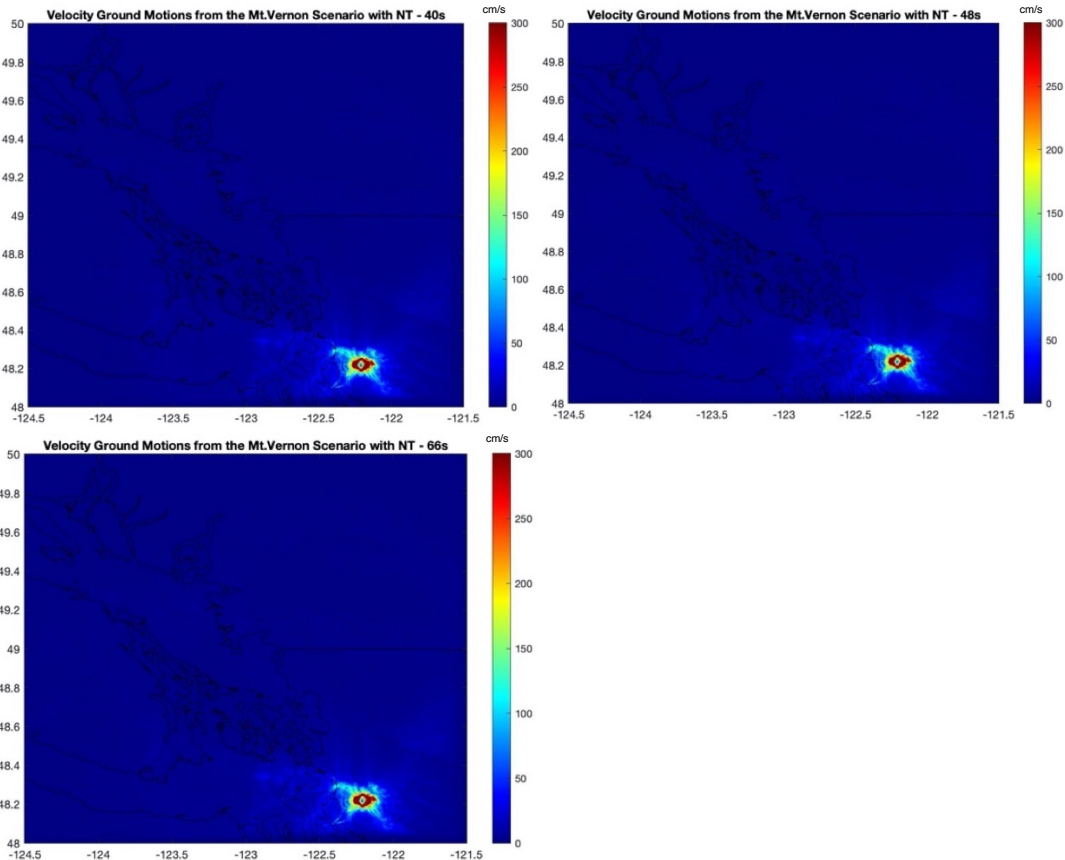
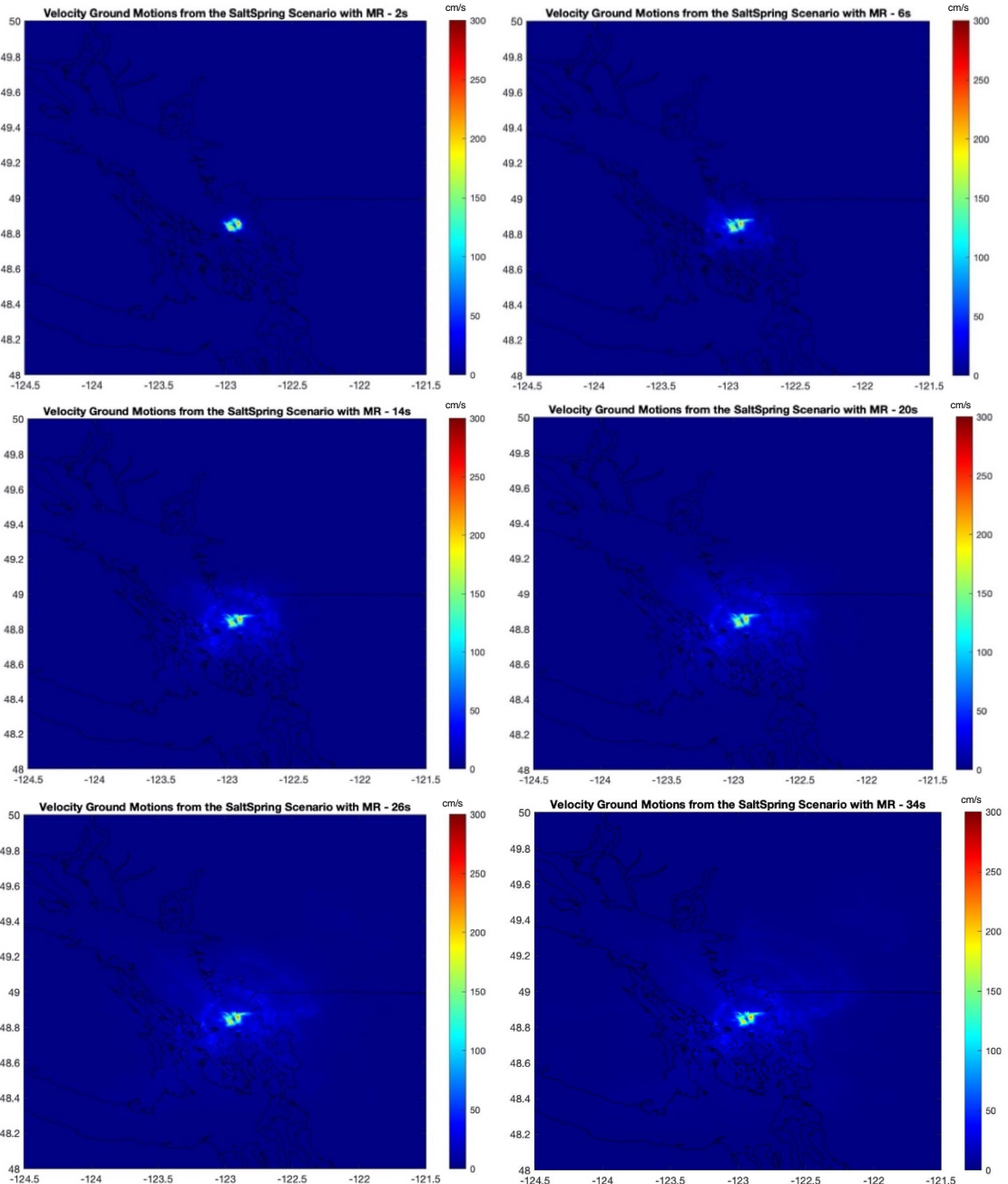


Figure 28: Velocity amplitude maps for the Mt. Vernon scenario without topography and MR from 2-66 seconds of simulation duration.



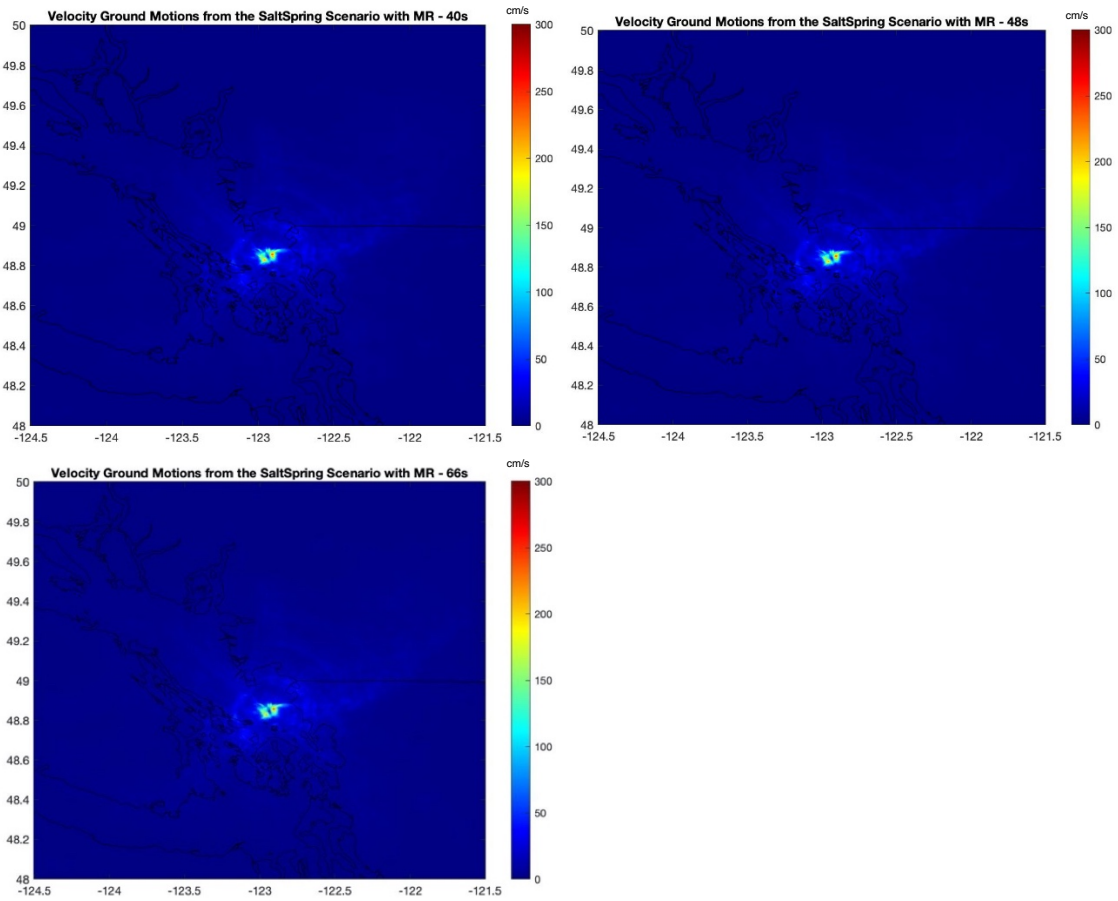
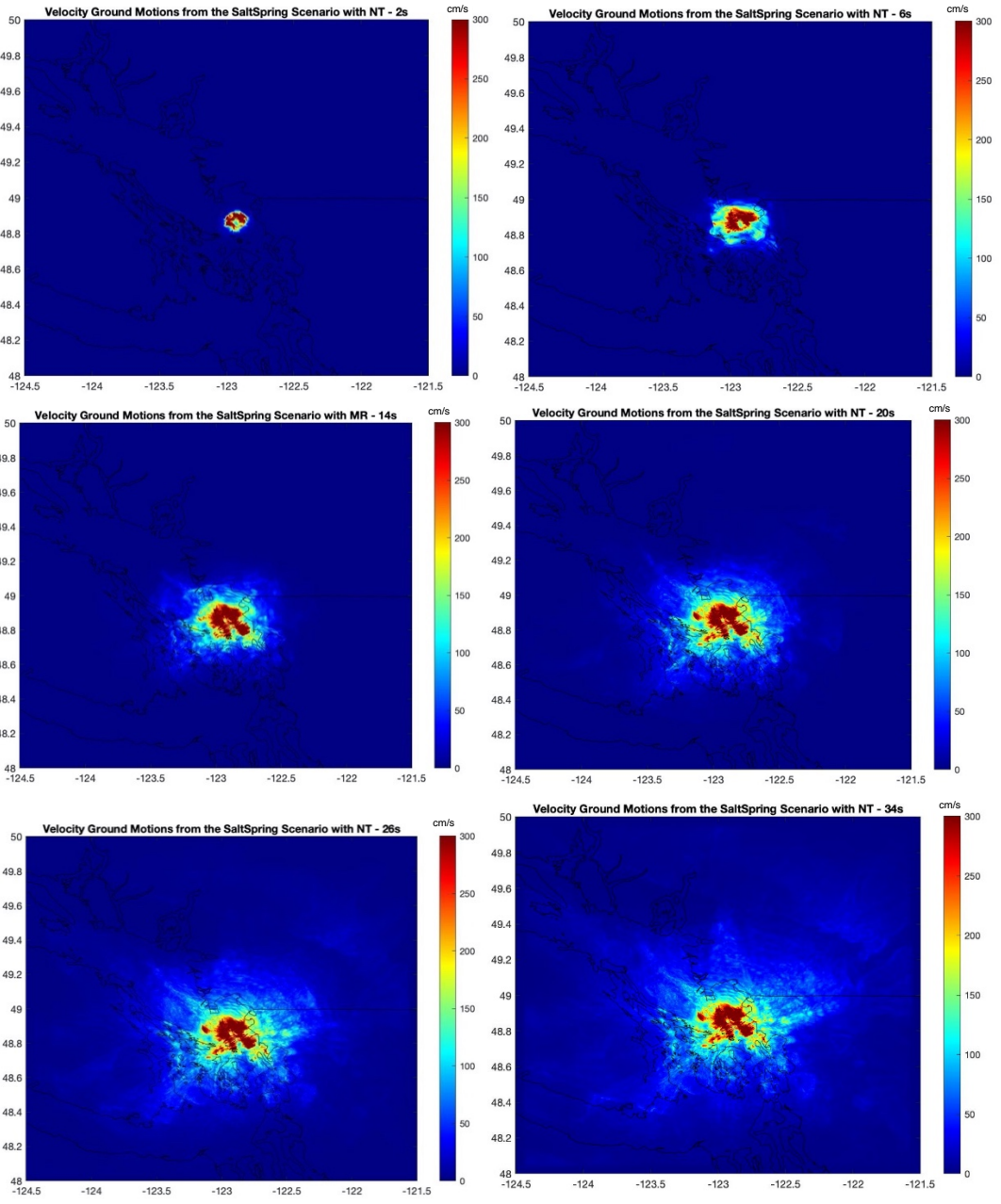


Figure 29: Velocity amplitude maps for the Salt Spring Island scenario with MR from 2-66 seconds of simulation duration.



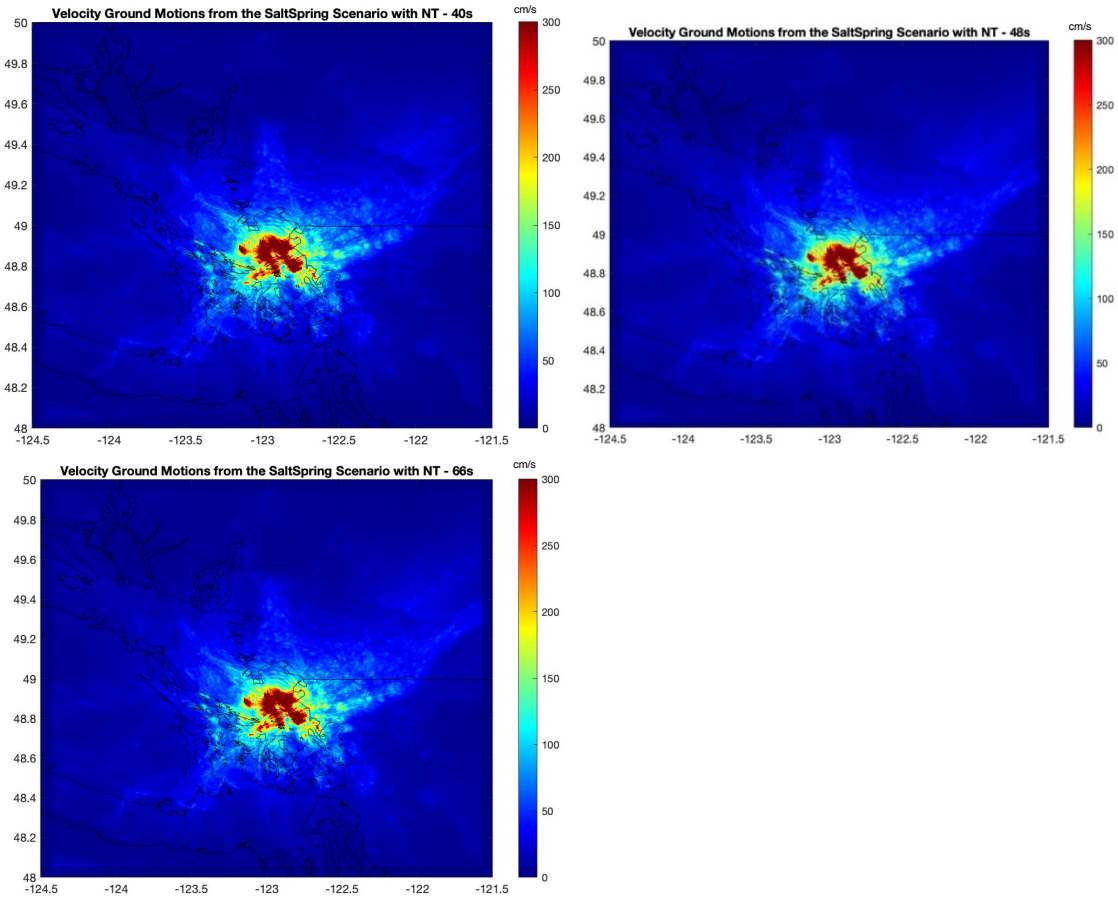
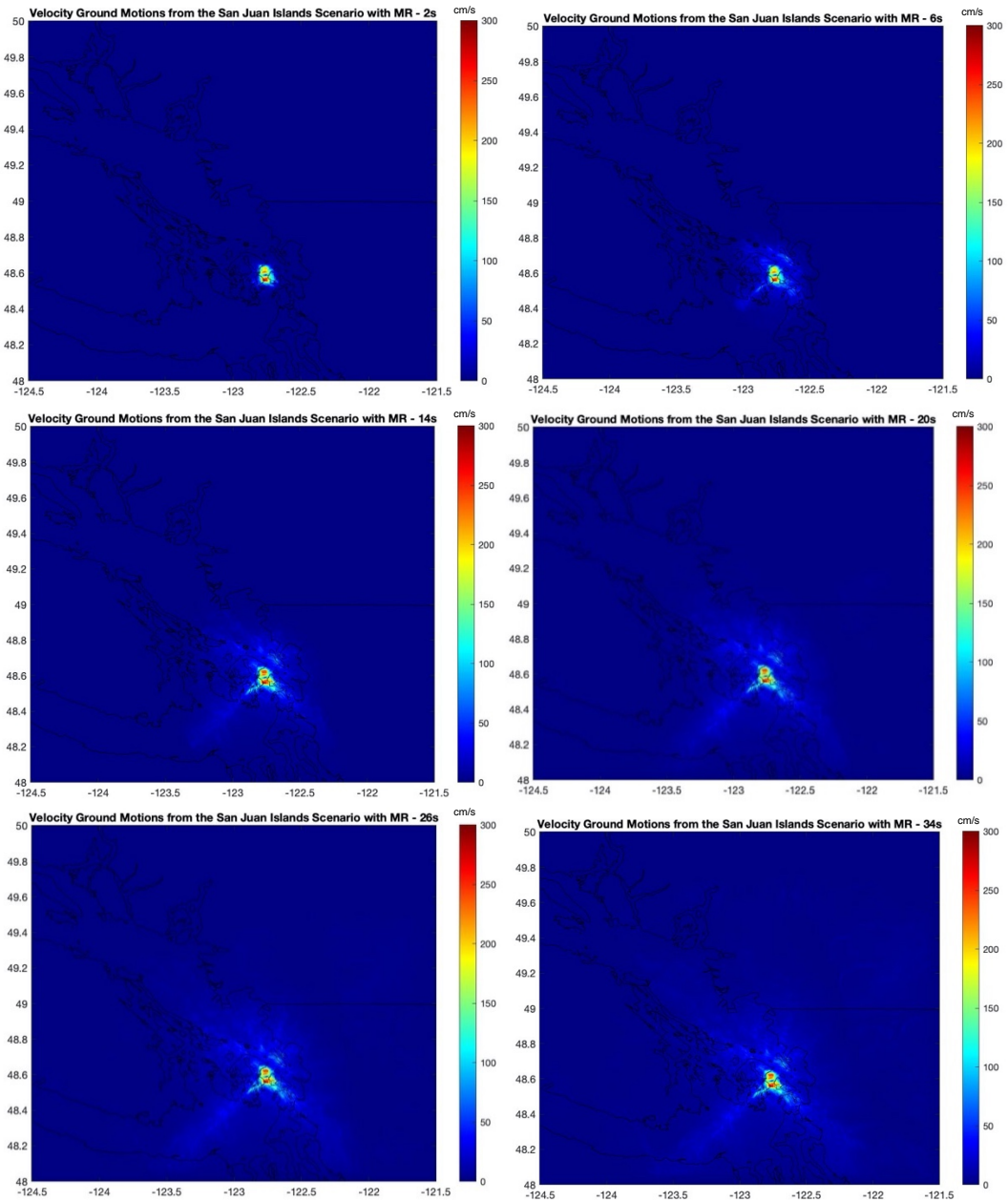


Figure 30: Velocity amplitude maps for the Salt Spring Island scenario without topography and MR from 2-66 seconds of simulation duration.



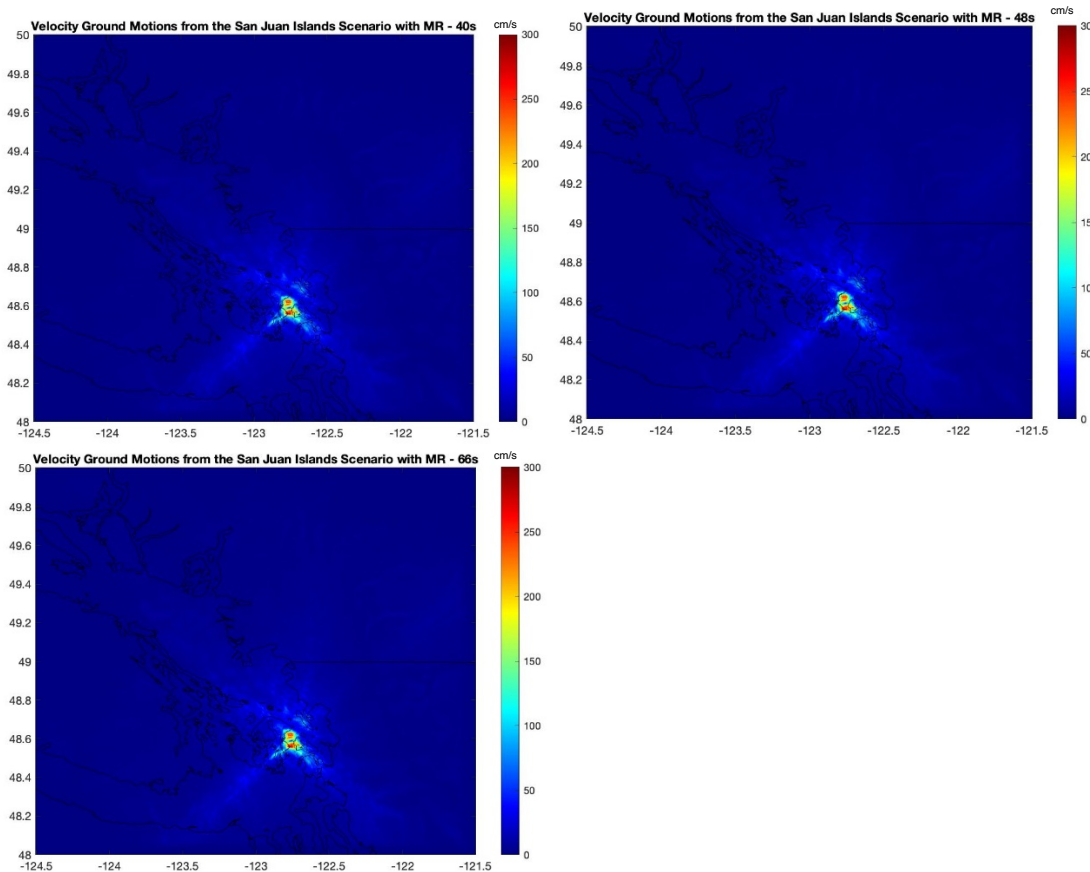
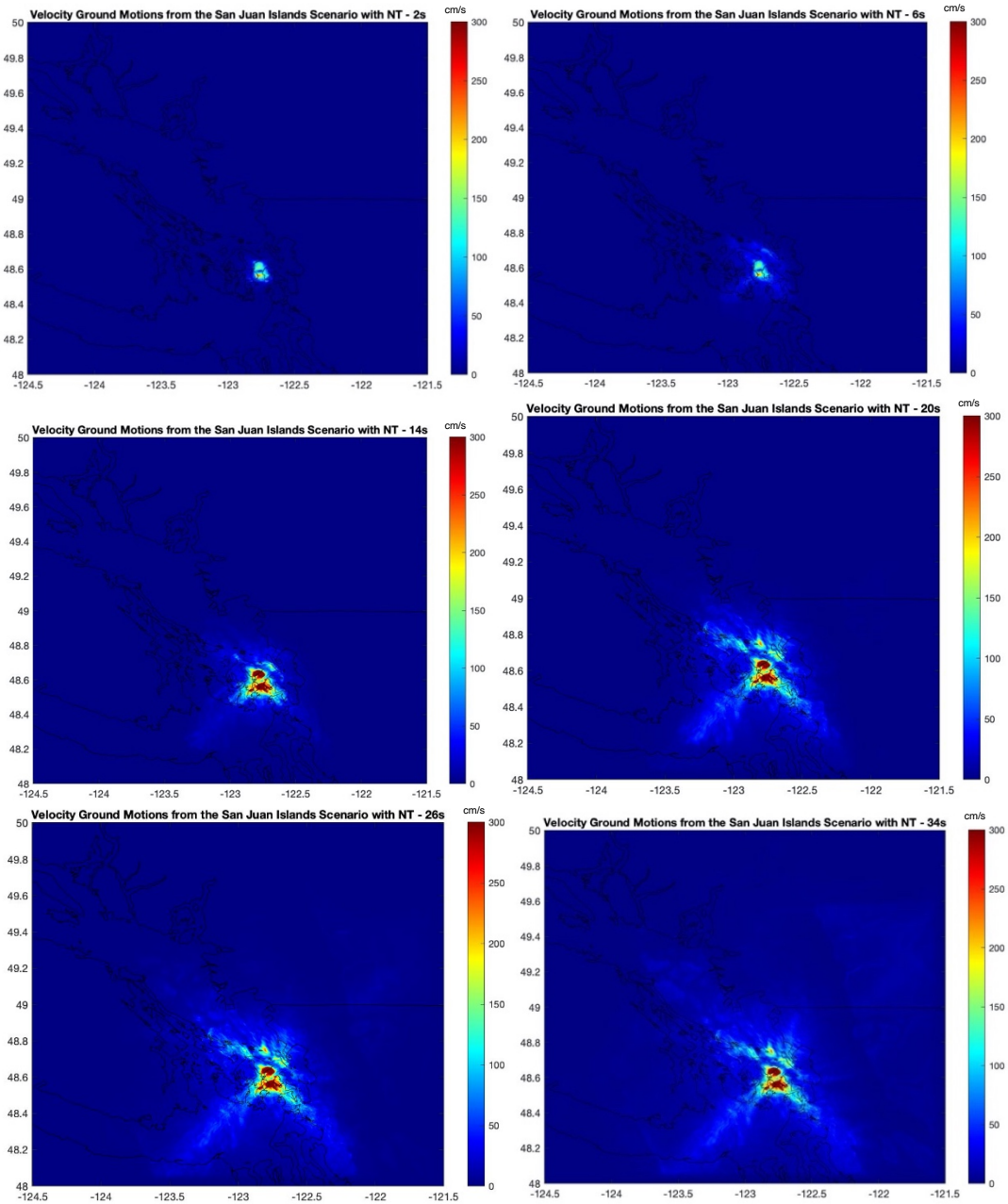


Figure 31: Velocity amplitude maps for the San Juan Island scenario with MR from 2-66 seconds of simulation duration.



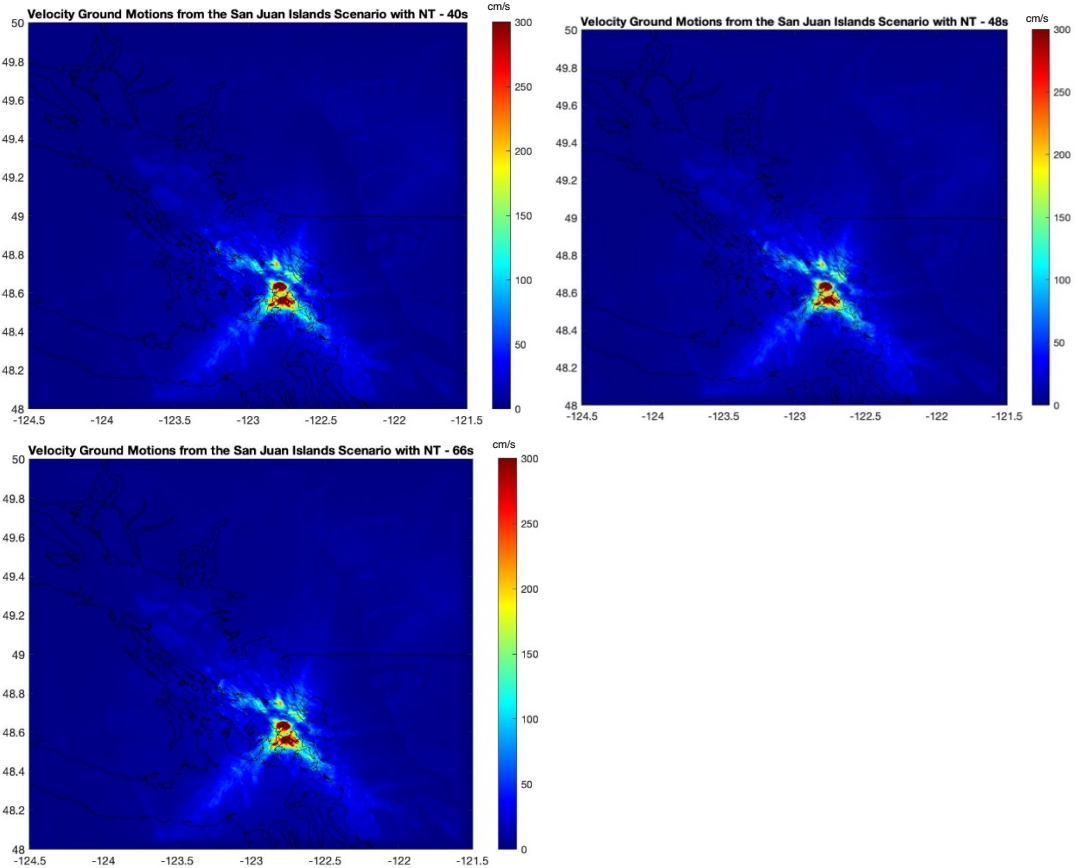
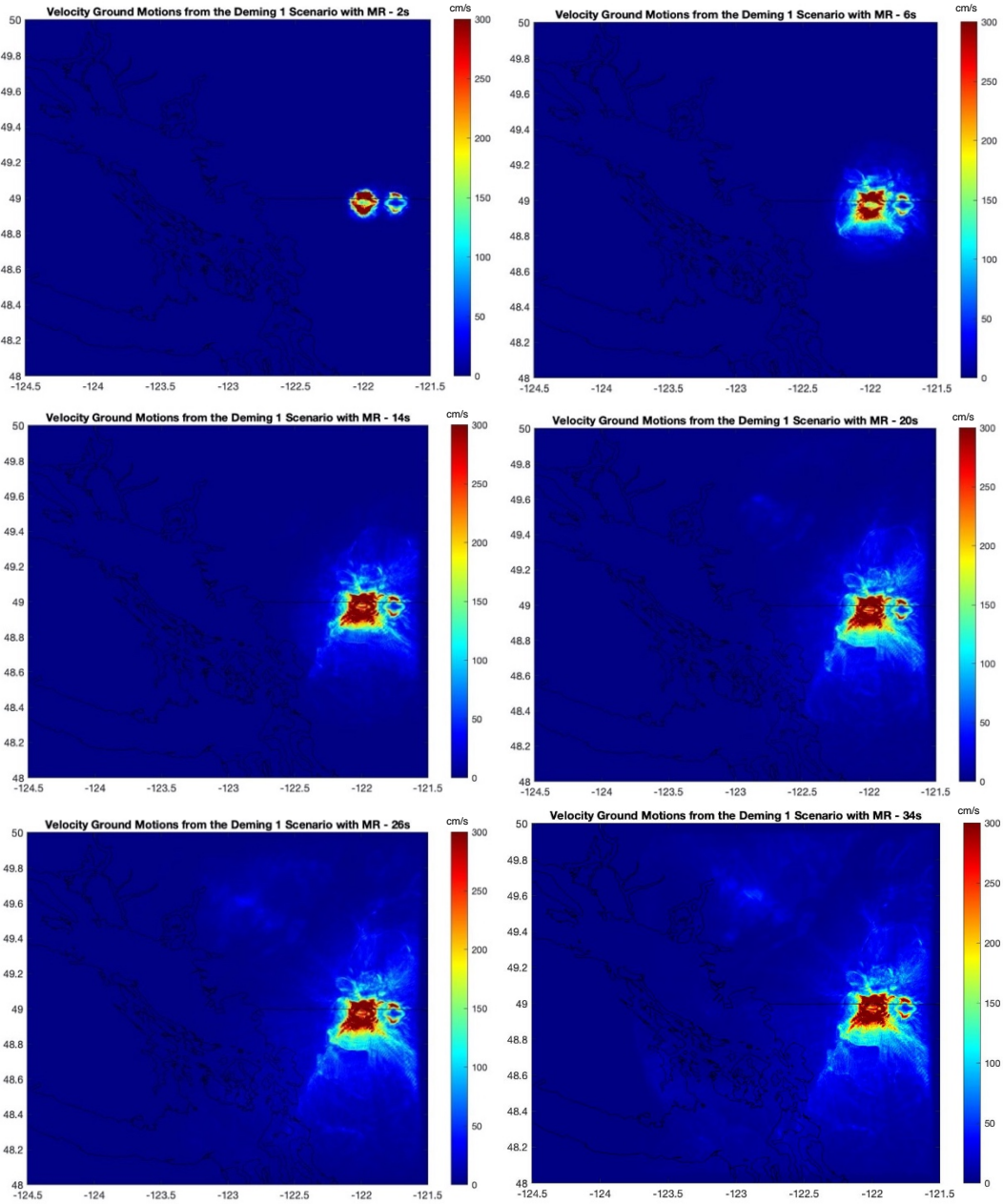


Figure 32: Velocity amplitude maps for the San Juan Island scenario without topography and MR from 2-66 seconds of simulation duration.



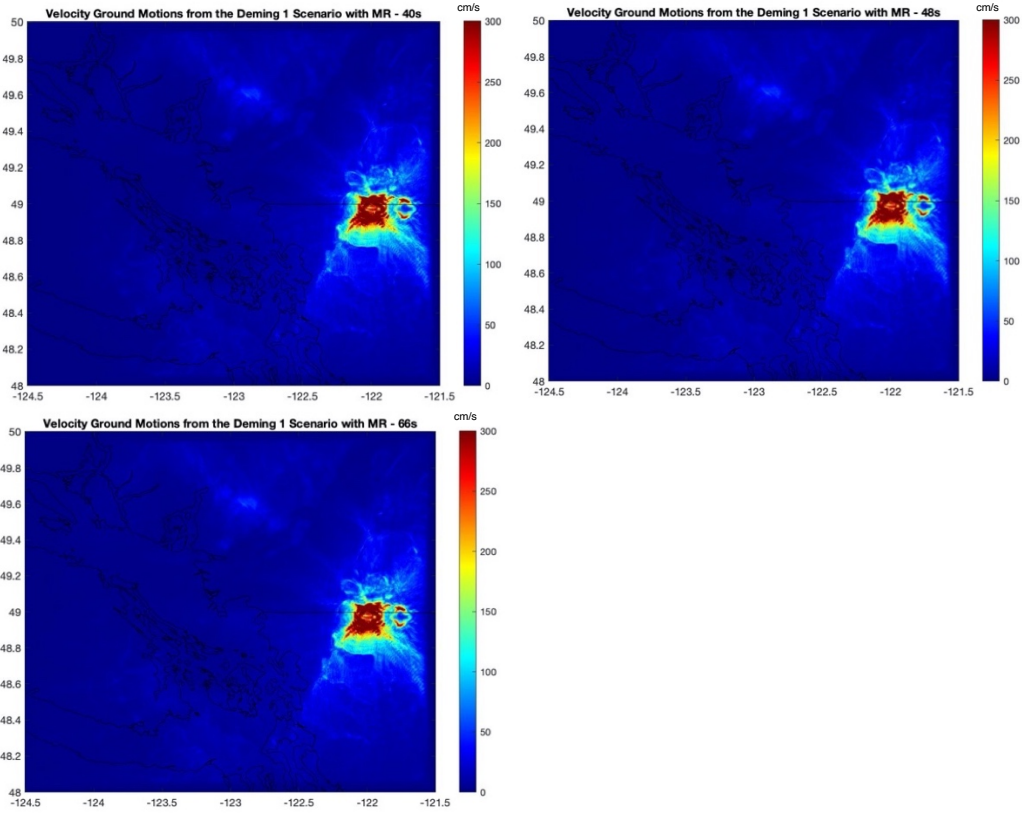
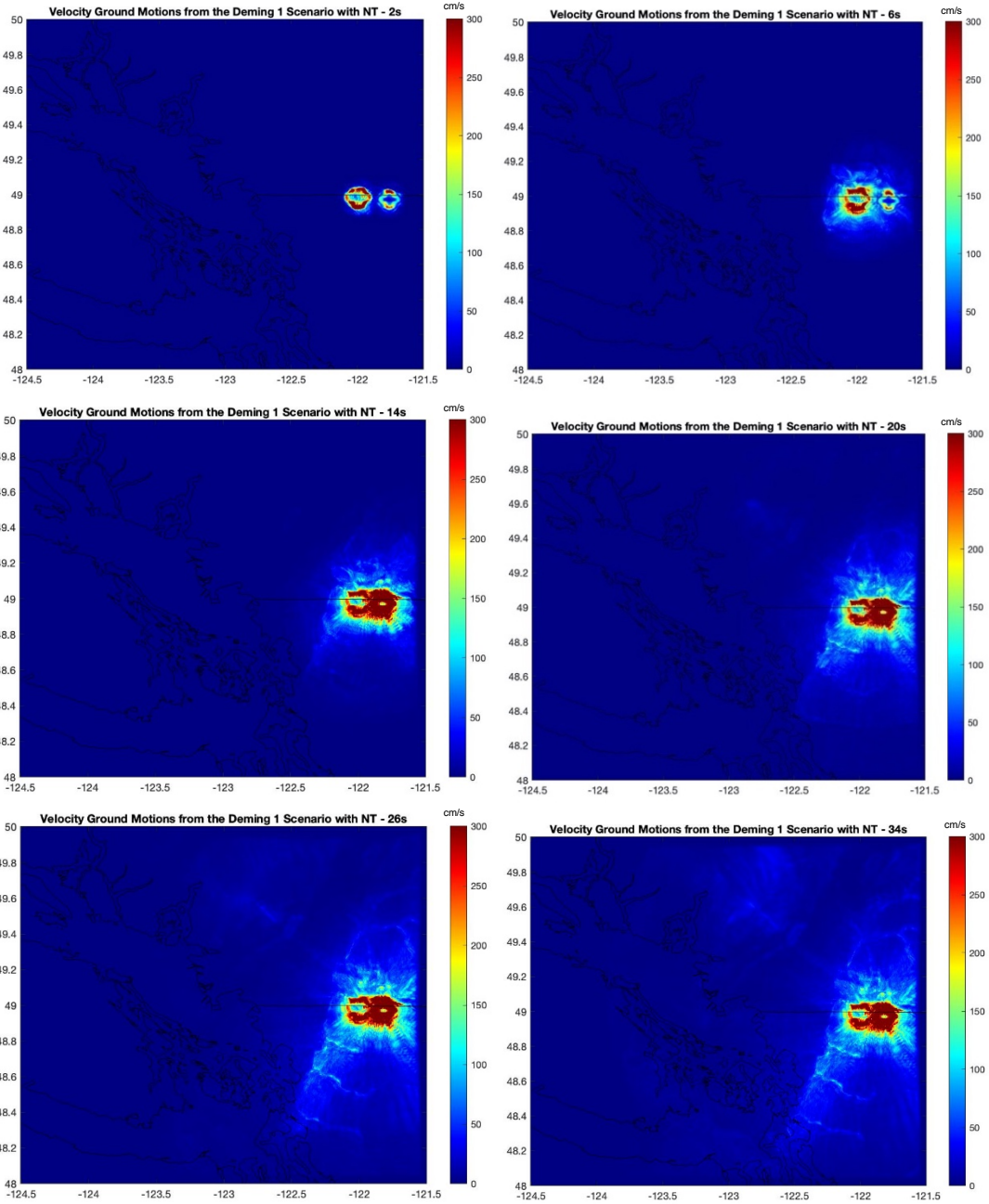


Figure 33: Velocity amplitude maps from 2-66 seconds for Deming 1 scenario with MR from 2-66 seconds of simulation duration.



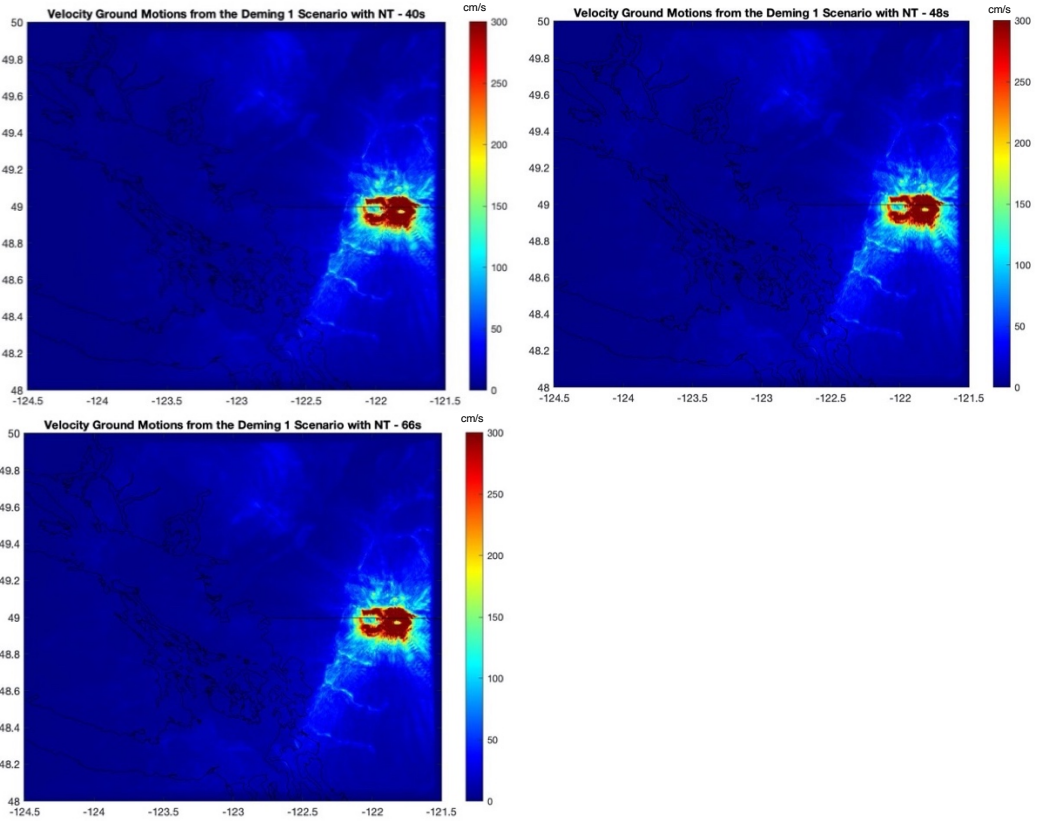
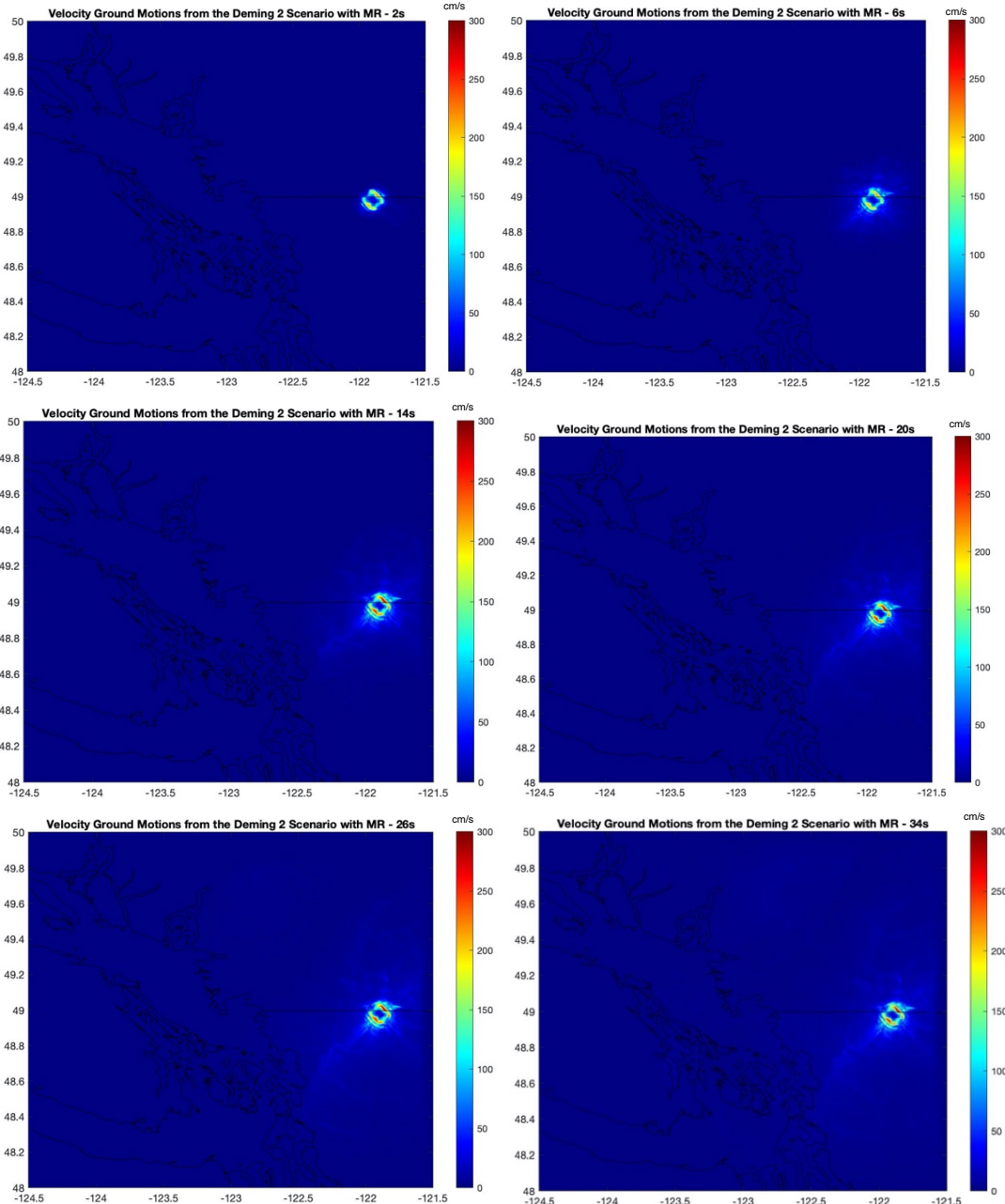


Figure 34: Velocity amplitude maps for the Deming 1 scenario without topography and MR from 2-66 seconds of simulation duration.



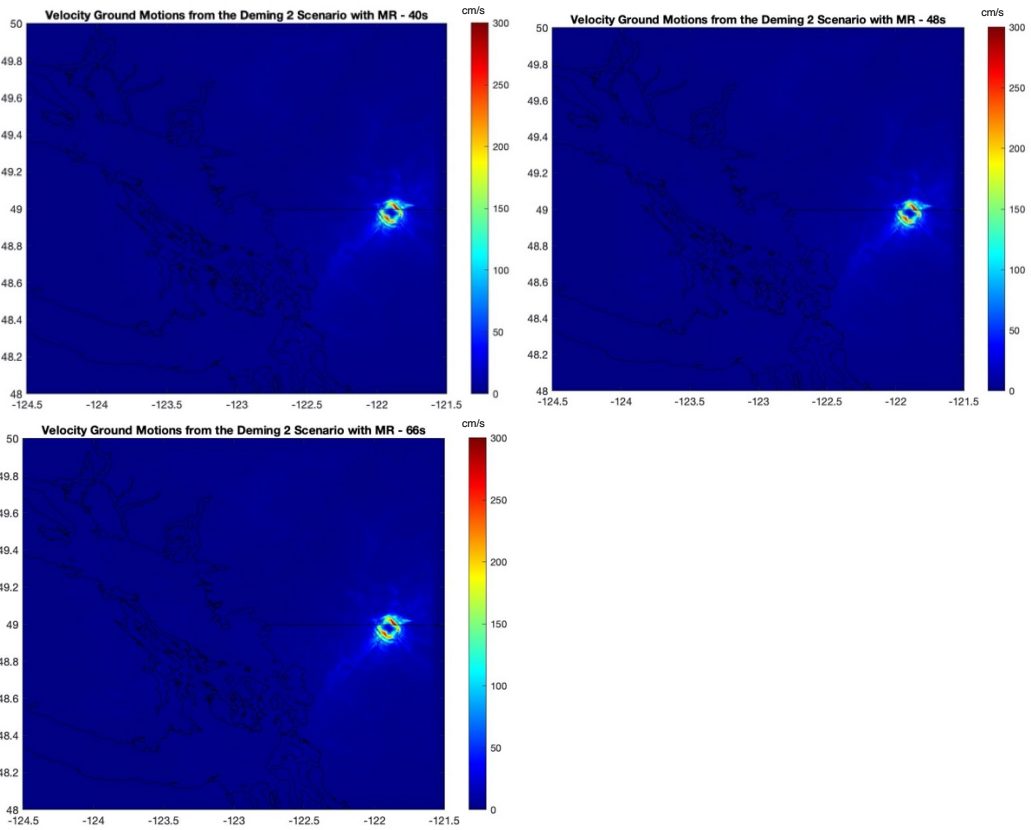
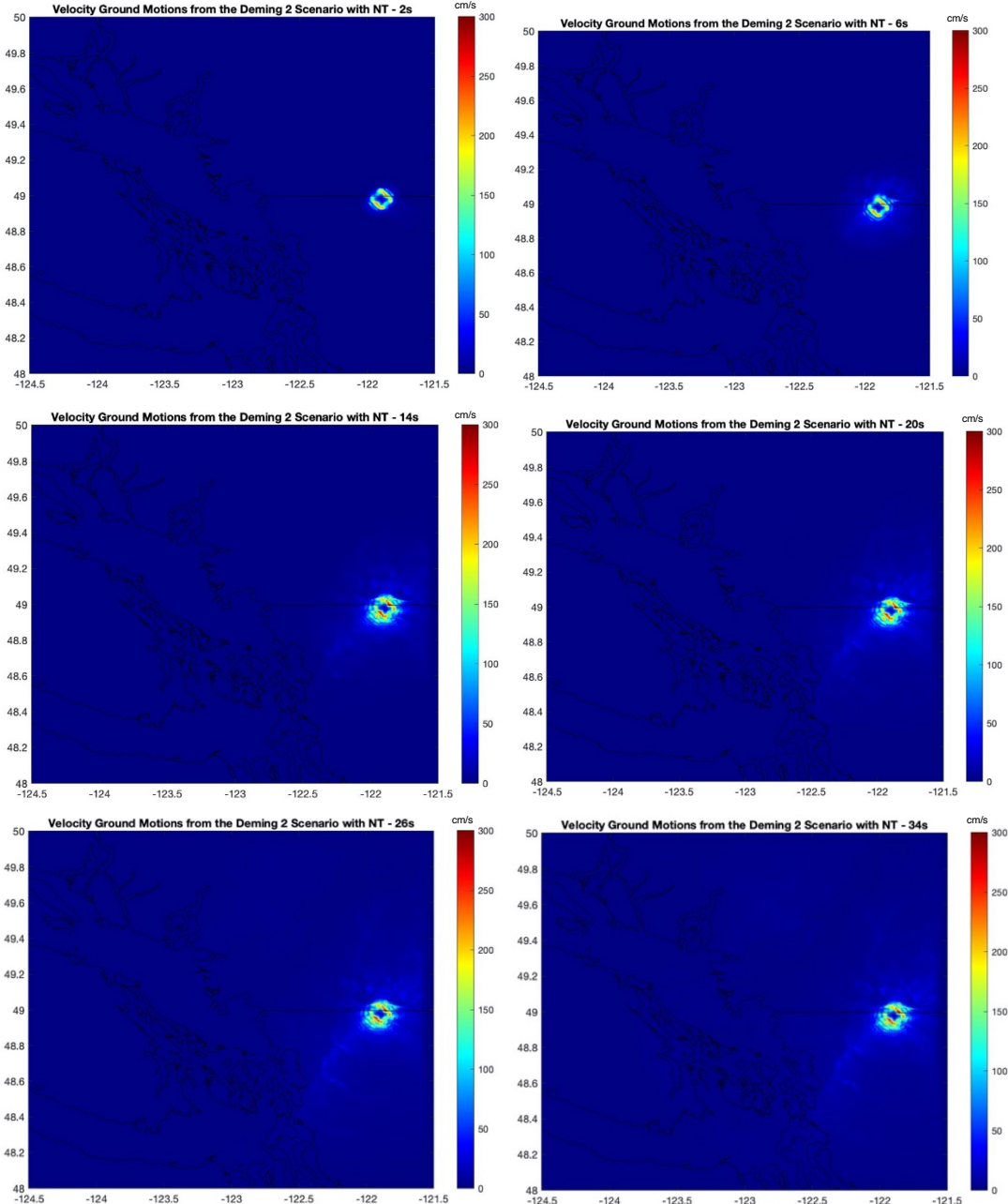


Figure 35: Velocity amplitude maps for Deming 2 scenario with MR from 2-66 seconds of simulation duration.



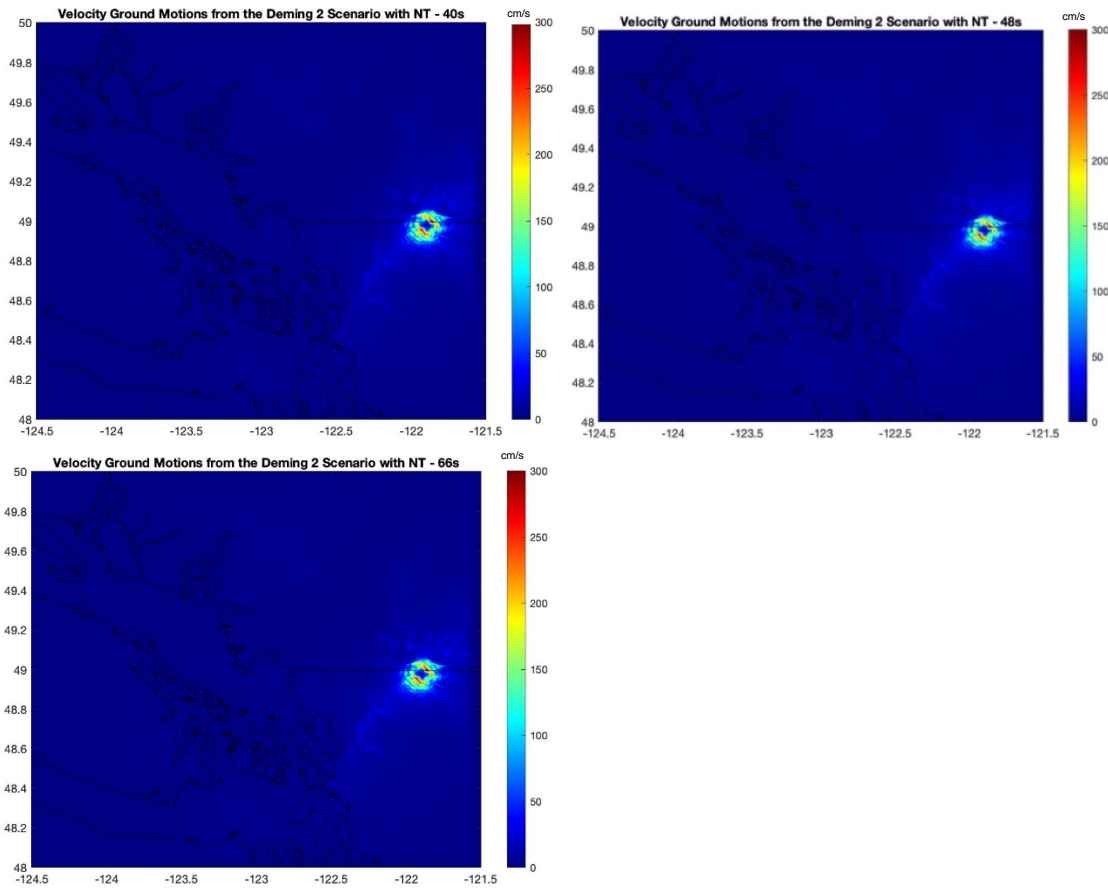
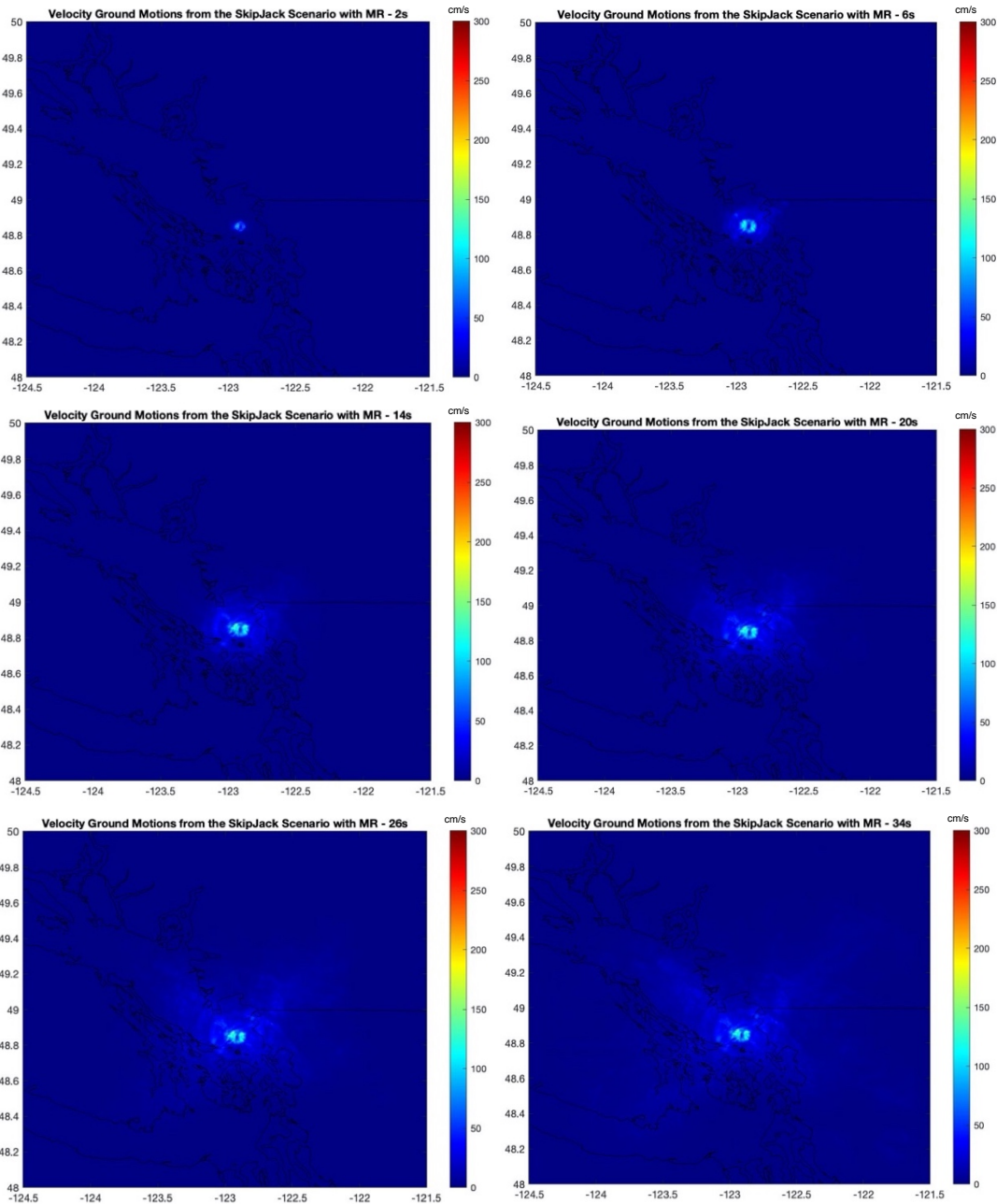


Figure 36: Velocity amplitude maps for the Deming 2 scenario without topography and MR from 2-66 seconds of simulation duration.



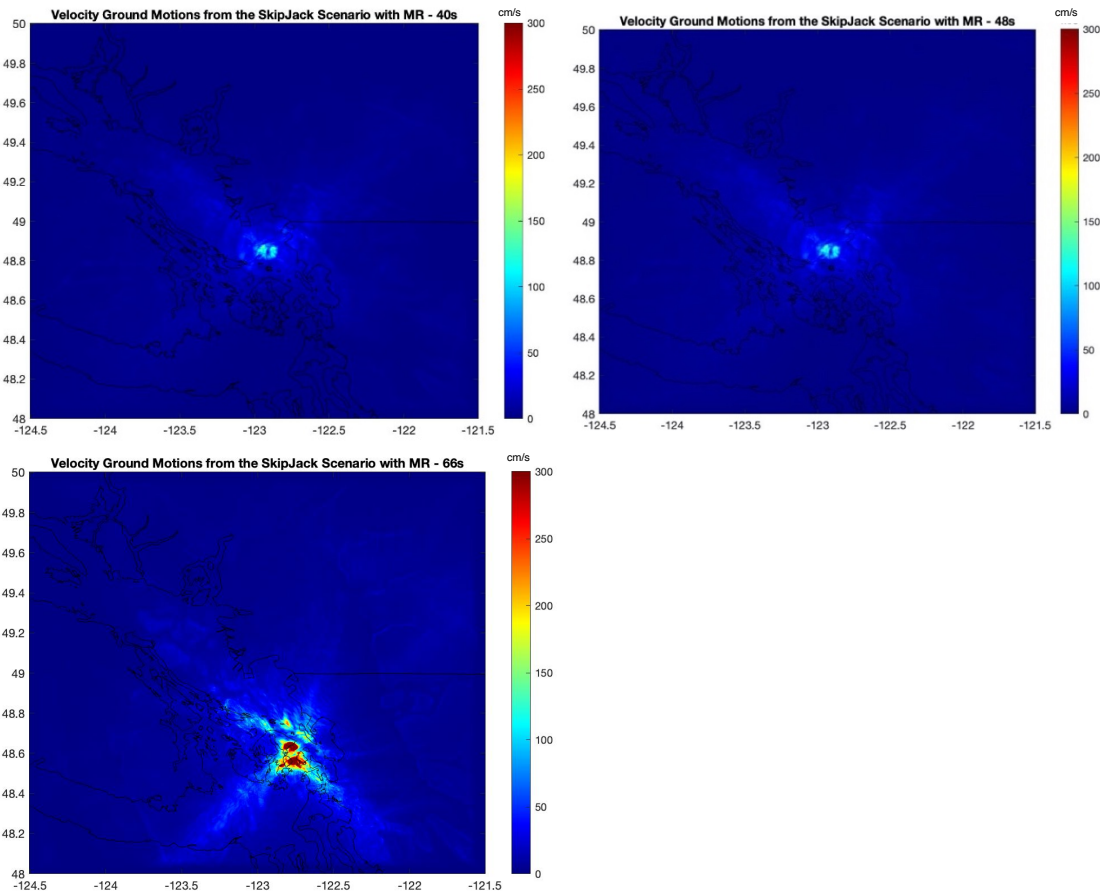
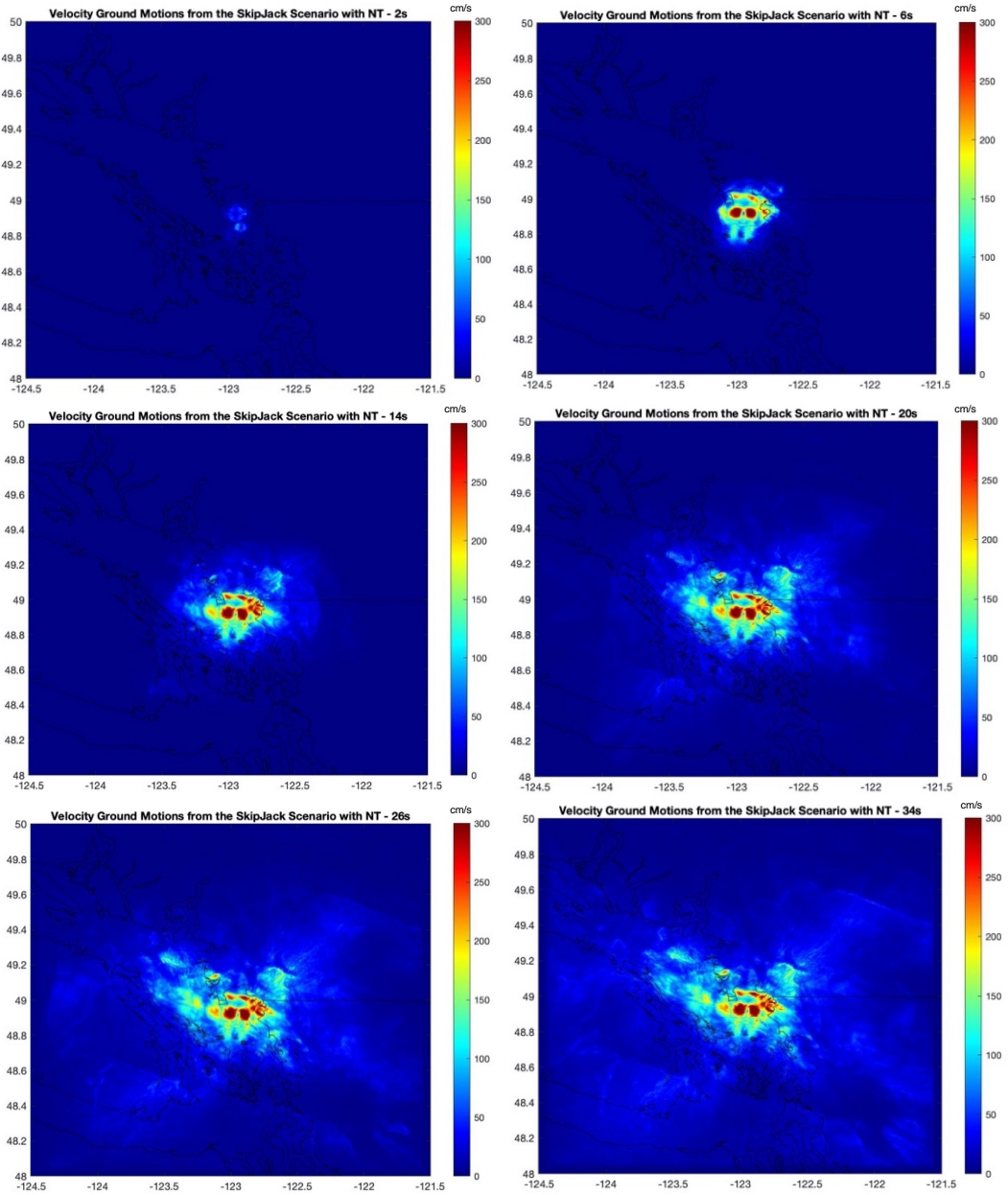


Figure 37: Velocity amplitude maps for the Skip Jack Island scenario with MR from 2-66 seconds of simulation duration.



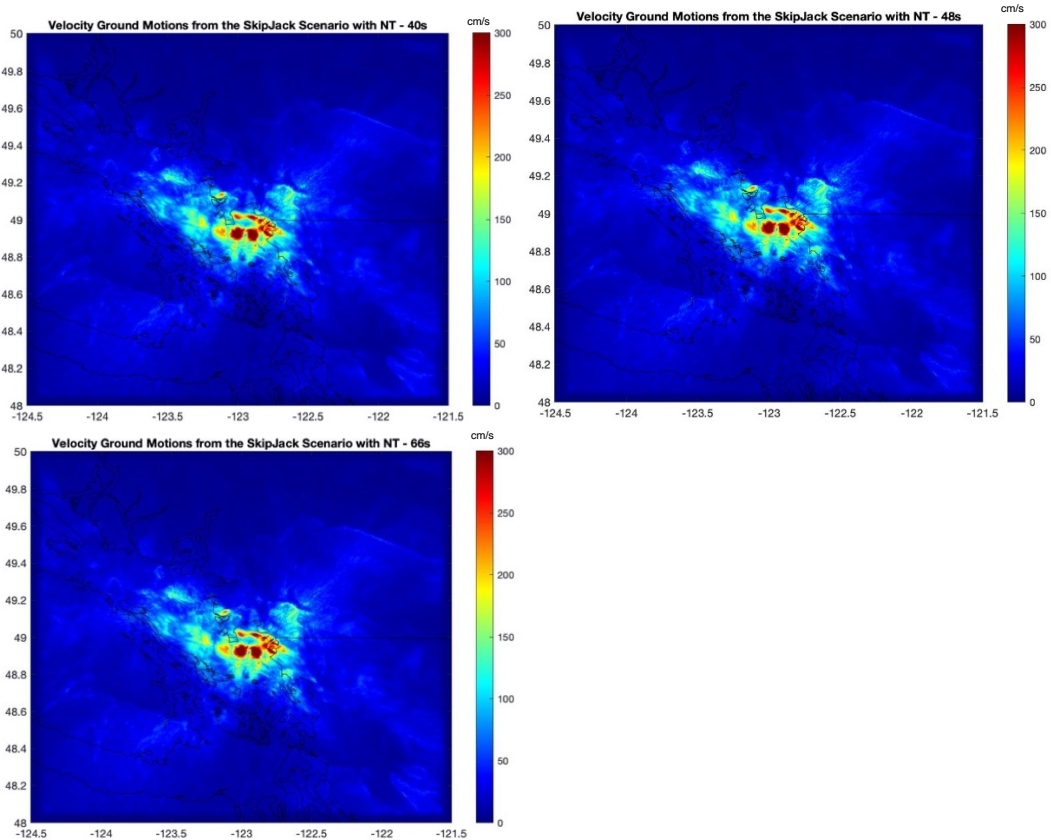
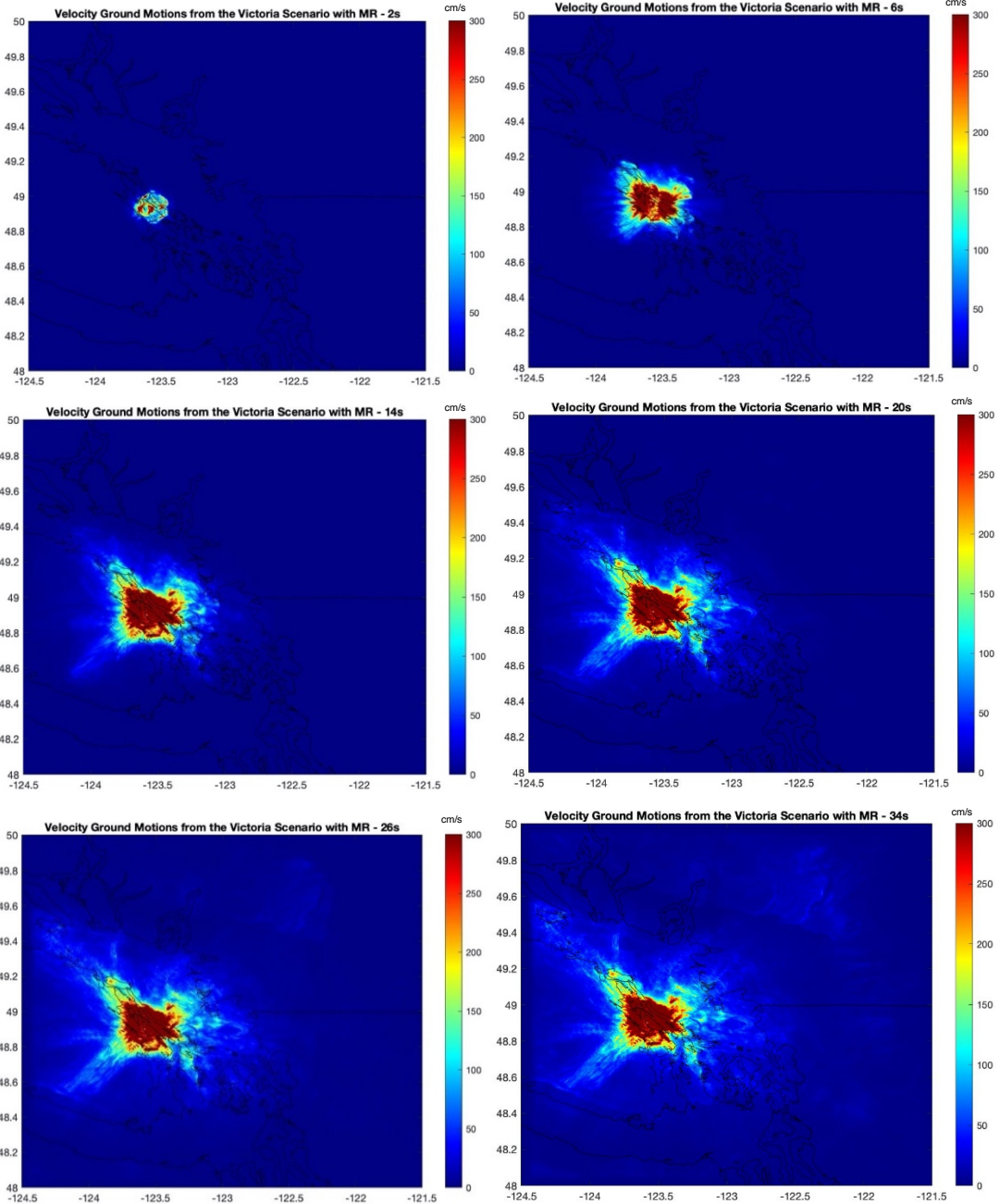


Figure 38: Velocity amplitude maps for the Skip Jack Island scenario without topography and MR from 2-66 seconds of simulation duration.



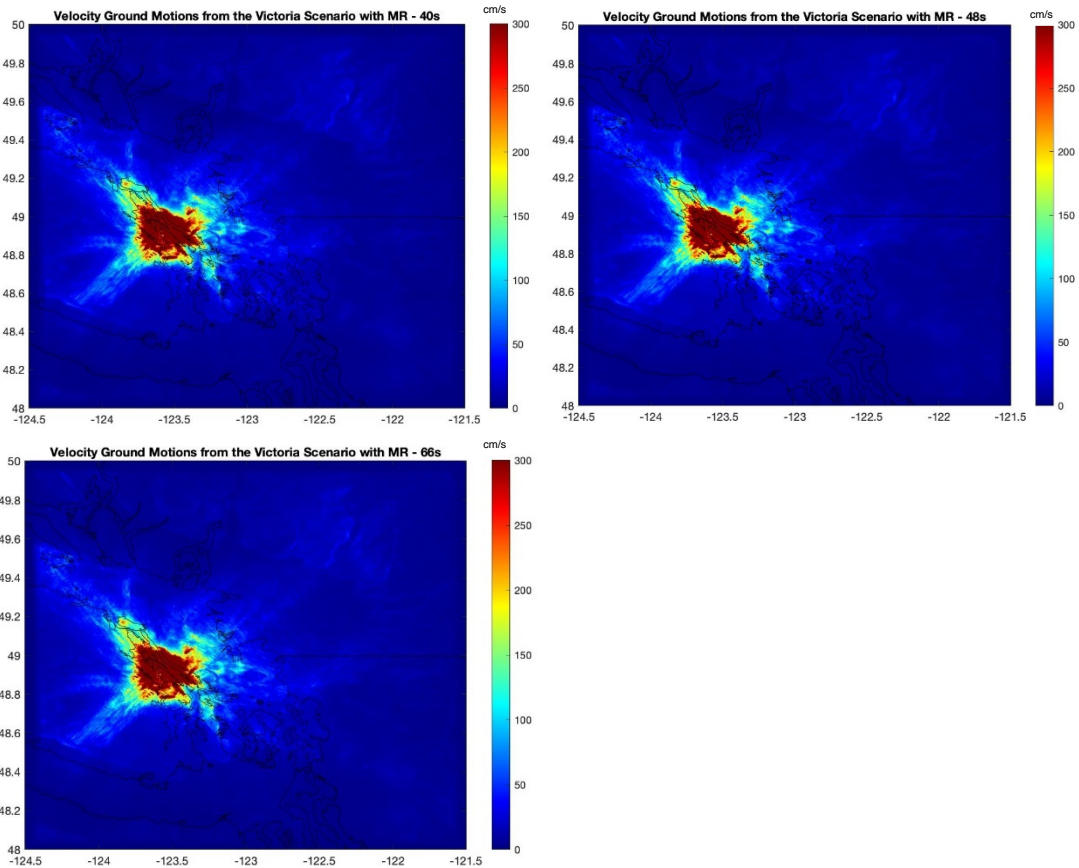
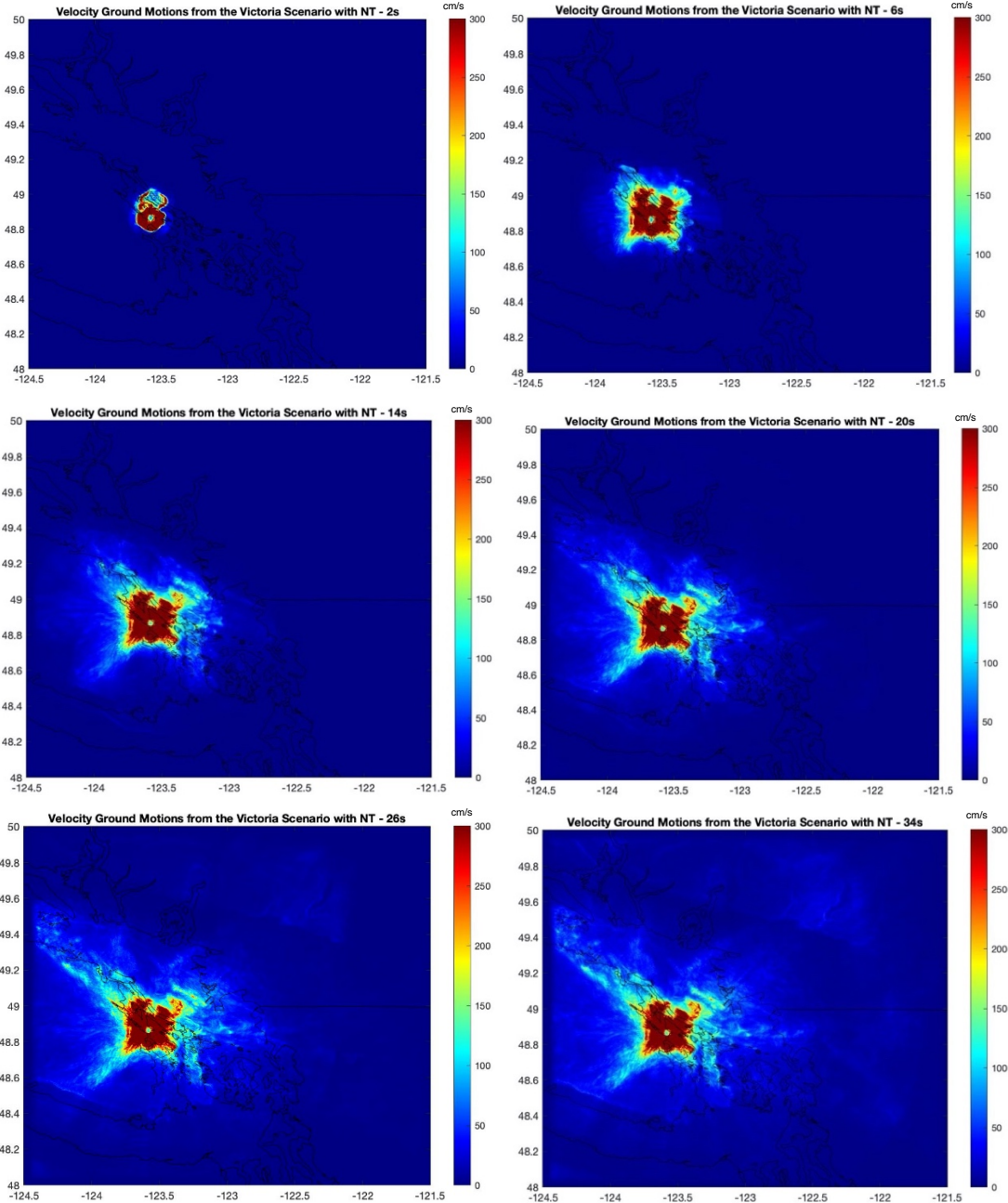


Figure 39: Velocity amplitude maps for the Victoria scenario with MR from 2-66 seconds of simulation duration.



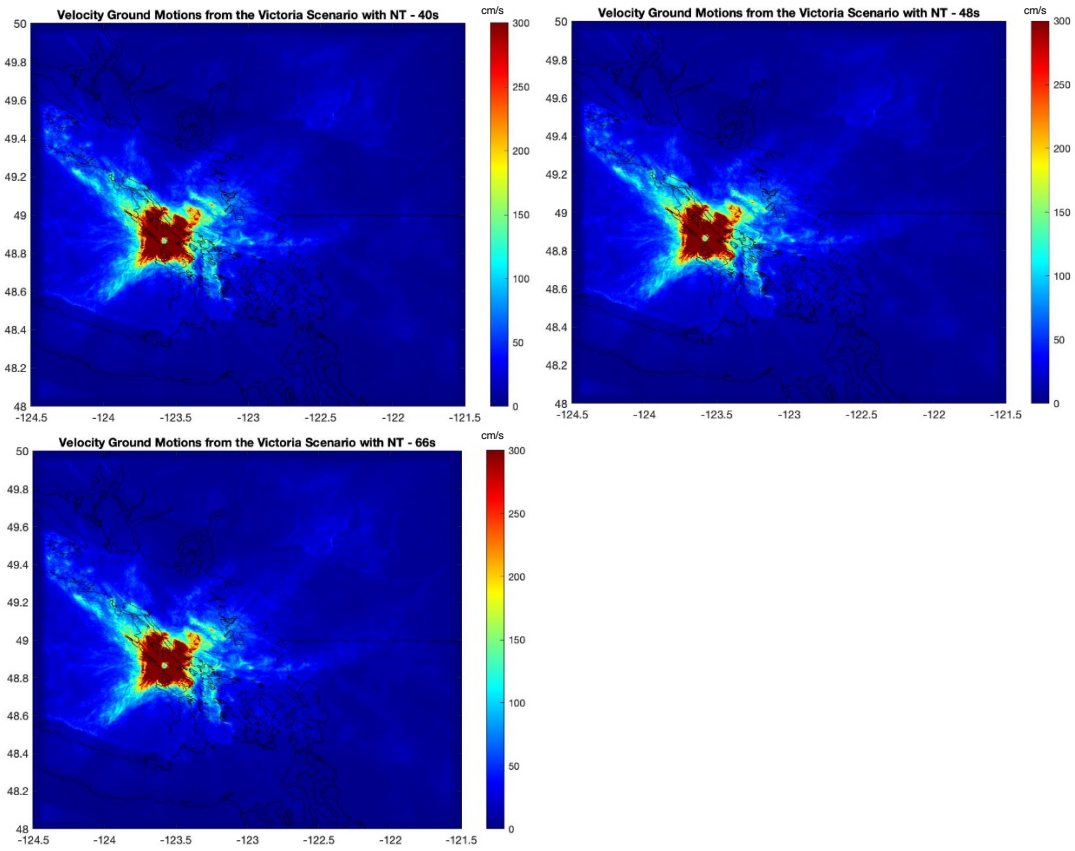


Figure 40: PGV maps for the Victoria scenario without topography and MR from 2-66 seconds of simulation duration.

Curriculum Vitae

Name:	Alex Vanderhoeff
Post – Secondary Education:	The University of Western Ontario (UWO) London, Ontario, Canada 2015-2020 B.Sc. Honours Specialization, Geophysics
	The University of Western Ontario (UWO) London, Ontario, Canada 2020-2023 M.Sc. Geophysics
Honours and Awards:	The University of Western Ontario Department of Earth Sciences The Geophysics award for excellence, 2017/2018
	The University of Western Ontario Department of Earth Sciences The Gold medal for Geophysics, 2020/2021
	The University of Western Ontario Dean's List, 2017-2020
Related Work Experience:	Teaching Assistant The University of Western Ontario 2020 – 2022
	Graduate Research Fellow The University of Western Ontario 2020 – 2023
	Management Consultant/Data Scientist BCG 2023
	Machine Learning Engineer Autodesk 2022
	Data Scientist BCG 2021

- Research Works:
Undergraduate Thesis: Thermal conductivity of an Fe-Ni alloy and implications for heat flow in the cores of terrestrial bodies.
- Presentations:
Thermal conductivity of an Fe-Ni alloy and implications for heat flow in the cores of terrestrial bodies. April 2020.
London, Ontario, Canada